Design of an Infrared Camera for Application on a Small Satellite Mission to Venus

Design einer Infrarotkamera zum Einsatz auf einer Venus Kleinsatellitenmission

Master's Thesis
Benjamin Buchmann
IRS-24-S-008

Supervisor:
Apl. Prof. Dr.-Ing. Ralf Srama (IRS)
Dr. Christian Fischer (IRS)
Dr. Matthias Grott (DLR)

Institute of Space Systems (IRS), University of Stuttgart
Institute for Planetary Research, German Aerospace Center (DLR)
March 2024

UNIVERSITÄT STUTTGART
INSTITUT FÜR RAUMFAHRTSYSTEME
im Raumfahrtzentrum Baden-Württemberg (RZBW)

Pfaffenwaldring 29 · 70569 Stuttgart · Tel.: 0711 685-62375 · www.irs.uni-stuttgart.de

Aufgabenstellung Masterarbeit

für Herrn Benjamin Buchmann

Design einer Infrarotkamera zum Einsatz auf einer Venus Kleinsatellitenmission

Design of an Infrared Camera for Application on a Small Satellite Mission to Venus

Motivation:

Das Institut für Planetenforschung befasst sich mit der Erforschung unseres Sonnensystems, insbesondere im Hinblick auf Ursprung, Entstehung und Entwicklung von Planeten, deren Monden und planetaren Kleinkörpern wie Asteroiden und Kometen. Hierfür entwickelt und baut die Abteilung Planetare Sensorsysteme wissenschaftliche Messinstrumente für die Anwendung auf planetaren Erkundungsmissionen der NASA, ESA und JAXA. Die Erforschung der Venus ist durch die Auswahl der NASA VERITAS sowie der ESA ENVISION Missionen erneut in den Fokus gerückt. Dabei ist gerade die Kenntnis der inneren Struktur der Venus weiterhin stark eingeschränkt, da z.B. seismische Messungen an der Venusoberfläche durch die sehr hohen Oberflächentemperaturen erschwert werden. Wie allerdings in Vorstudien bereits gezeigt werden konnte, besteht die Möglichkeit, seismische Messungen indirekt durch eine Beobachtung der Venusatmosphäre durchzuführen. Im Rahmen der anzufertigenden Arbeit sollen die wesentlichen Kenngrößen einer möglichen Instrumentierung für eine Kleinsatellitenmission auf Basis eines Nahinfrarotsensors spezifiziert und ein erstes Instrumentenkonzept abgeleitet werden.

Aufgabenstellung:

- Einarbeitung in die Themen Radiometrie, Optik und Instrumentendesign
- Identifizierung der Messanforderungen und Berechnung von Signal zu Rauschverhältnissen
- Durchführung von Trade-off Studien für die Auswahl der Sensorik und der Optik
- Ableiten eines Instrumentenkonzeptes
- Dokumentation

Die Arbeit wird bei Deutsches Institut für Luft- und Raumfahrt e.V. (DLR) – Institut für Planetenforschung durchgeführt.

Betreuer,-in intern: Fischer, Christian

Betreue,-in extern: Dr. Matthias Grott

Bearbeitungsbeginn: 01.10.2023

Einzureichen spätestens: 31.03.2024

Empfangsbestätigung:
Ich bestätige hiermit, dass ich die Aufgabenstellung sowie die rechtlichen Bestimmungen und die Studien- und Prüfungsordnung gelesen und verstanden habe.

[redacted]
Datum
Apl. Prof. Dr.-Ing. Ralf Srama
(Verantwortlicher Hochschullehrer)

Matthias Grott
Digital signiert von Matthias Grott
DN: C=DE, O=Deutsches Zentrum fuer Luft- und Raumfahrt e.V. (DLR), SN=Grott, G=Matthias, CN=Matthias Grott
Grund: Ich habe dieses Dokument geprüft
Ort: Berlin
Datum: 2023.06.15 13:55:49+02'00'
Foxit PDF Reader Version: 12.1.2
Datum
Externe/r Betreuer/-in

Datum
Unterschrift des/der Studierenden

Rechtliche Bestimmungen: Der/die Bearbeiter/in ist grundsätzlich nicht berechtigt, irgendwelche Arbeits- und Forschungsergebnisse, von denen er/sie bei der Bearbeitung Kenntnis erhält, ohne Genehmigung des/der Betreuers/in dritten Personen zugänglich zu machen. Bezüglich erreichter Forschungsleistungen gilt das Gesetz über Urheberrecht und verwendete Schutzrechte (Bundesgesetzblatt I/ S. 1273, Urheberschutzgesetz vom 09.09.1965). Der/die Bearbeiter/in hat das Recht, seine/ihre Erkenntnisse zu veröffentlichen, soweit keine Erkenntnisse und Leistungen der betreuenden Institute und Unternehmen eingeflossen sind. Die von der Studienrichtung erlassenen Richtlinien zur Anfertigung der Masterarbeit sowie die Prüfungsordnung sind zu beachten.

Statement of Authorship

I, **Buchmann, Benjamin**, hereby confirm that I have written this ***Master's thesis*** independently with the support of the supervisor(s) and have not used any sources and aids other than those specified. The thesis or essential parts of it have not been submitted to this or any other educational institution for the completion of a degree. I further declare that I have complied with the relevant provisions on copyright protection of third-party contributions in accordance with the rules of proper scientific practice when preparing the thesis. As far as my thesis contains third-party contributions (e.g. images, drawings, text passages, etc.), I have marked these contributions as such (citation, reference) and obtained any necessary permission from the authors to use these contributions in my work. I am aware that in the event of a culpable breach of these obligations, I must bear the resulting consequences.

Berlin, 24.03.2024, B. B.....

Location, date, signature

I hereby agree that my ***Master's thesis*** on the topic:

Design of an Infrared Camera for Application on a Small Satellite Mission to Venus

will be kept publicly accessible in the library of the Institute of Space Systems without an embargo period and the thesis will be listed on the Institute's website and in the online catalog of the University Library. The latter means permanent, worldwide visibility of the bibliographic data of the thesis (title, author, year of publication, etc.). Upon completion of the thesis, I will provide my supervisor with a printed and a digital version in addition to the review copy. I transfer ownership of these additional versions to the University of Stuttgart and grant the Institute of Space Systems free, temporally and locally unrestricted, non-exclusive right of use for research and teaching purposes to this thesis and to the results generated by me within the scope of this thesis. If, in connection with the thesis, agreements on rights of use exist between the Institute and third parties, these agreements also apply to the results produced within the scope of this thesis.

Berlin, 24.03.2024, B. B.....

Location, date, signature

Acknowledgements

I would like to express my deepest gratitude to my supervisor Dr. Matthias Grott for his intangible support and invaluable support from the beginning throughout the entire process of this exciting project. He has not only helped but also challenged me as I've come to complete this final stage of my academic journey. I am also very grateful for his encouragement and advice on the first steps towards my professional career.

I would like to express my sincere gratitude to Dr. Ralf Srama and Dr. Christian Fischer for their valuable feedback and guidance. I could not have undertaken this work without their very kind and patient, supportive communication, especially in the final phase of my work.

I had the pleasure of meeting many colleagues at DLR and would like to thank them all for their kind help and support. I have also enjoyed many enlightening conversations and feedback sessions with my fellow office mates. Lastly, I'd like to thank my family and friends, especially my mother, for their moral and emotional support. Your belief in me has kept my spirits and motivation high throughout my academic journey and I am beyond grateful to have you all by my side.

Abstract

With the upcoming NASA VERITAS and ESA EnVision missions renewing focus on the exploration of Venus, where the understanding of the interior structure of the planet remains limited due to the challenging surface conditions. This thesis investigates the feasibility of detecting seismic activity on Venus using infrared measurements from orbit. This provides a more robust and cost-effective approach based on the possibility of observing CO_2 non-local thermodynamic equilibrium (NLTE) emissions at a wavelength of 4.3 µm on the dayside and O_2 airglow emissions at 1.27 µm on the nightside to detect atmospheric-coupled Rayleigh waves in the Venusian atmosphere. The aim is to derive an initial instrument concept for a small satellite mission with the capability to be included as a rideshare on an upcoming Venus mission, providing insights into the interior structure of Venus. Combining radiometry, optics, infrared detectors, remote sensing, image processing and planetary science of Venus, this thesis defines an initial mission and instrument design and performs trade-off analyses to propose a preliminary imaging system design with sufficient signal-to-noise ratio (SNR) and spatial resolution performance in terms of the modulation transfer function (MTF). The results identified limitations in the detectability of atmospheric-coupled Rayleigh waves due to insufficient SNR performance. Despite these challenges, the study found that higher seismic magnitudes can be detected with suitable imaging system configurations and image processing methods. Trade-off analyses led to the identification of preliminary designs for observing both the day- and nightside of Venus. The imaging system based on the Raytheon Phoenix detector is recommended as the most suitable concept for achieving the mission objective, with the ability to observe both wavelengths providing a higher probability of detecting seismic activity from orbit.

Zusammenfassung

Die bevorstehenden Missionen NASA VERITAS und ESA EnVision haben das Interesse an der Erforschung der Venus neu entfacht, wobei die Herausforderungen der Oberflächenbedingungen weiterhin das Verständnis der inneren Struktur des Planeten stark einschränken.

Diese Arbeit untersucht die Möglichkeit, seismische Aktivitäten auf der Venus mithilfe der Beobachtung der Venusatmosphäre im Infrarotbereich aus dem Orbit um die Venus zu detektieren. Durch die Beobachtung von Emissionen bei einer Wellenlänge von 4.3 µm durch angeregte CO_2 Moleküle im nicht-lokalen thermodynamischen Gleichgewicht auf der Tagseite und O_2 Airglow Emissionen bei 1.27 µm auf der Nachtseite ist es möglich, seismische Rayleigh-Wellen in der Venusatmosphäre zu detektieren, welche von der Venusoberfläche in die Atmosphäre übertragen werden. Das Hauptziel besteht darin, ein erstes Konzept für eine Instrumentierung einer Kleinsatellitenmission zu ermitteln.

Dabei werden Fachgebiete wie Radiometrie, Optik, Infrarotdetektoren, Fernerkundung, Bildverarbeitung und Planetenforschung der Venus kombiniert, um ein passendes Missions- und Instrumentendesign zu definieren. Die Analyse von Trade-off Studien führt zur Ableitung eines vorläufigen Instrumentenkonzepts mit hinreichendem Signal-Rausch-Verhältnis und räumlicher Auflösungsleistung.

Die Ergebnisse zeigen Limitierungen der Detektion der atmosphärisch gekoppelten Rayleigh-Wellen aufgrund unzureichender Signal-Rausch-Verhältnis-Leistung. Trotz dieser Herausforderungen können stärkere seismische Beben mit geeigneten Instrumentendesigns detektiert werden. Die Trade-off Studien führten zur Identifizierung von Preliminary Designs für die Beobachtung der Tag- und Nachtseite der Venus. Das Infrarotkameradesign unter Verwendung des Raytheon Phoenix Detektor wird als das geeignetste Konzept zur Erfüllung des Missionsziels empfohlen. Aufgrund der Möglichkeit beide Seiten der Venus bzw. beide Wellenlängen zu beobachten, bietet dieses Konzept eine höhere Wahrscheinlichkeit seismische Aktivitäten zu detektieren.

Table of Contents

List of Figures

List of Tables

List of Symbols

Symbol	Unit	Name
Ω	sr	Solid Angle
$f/\#$	-	f-Number
f	m	Focal Length
D	m	Aperture Diameter
L_λ	W m^{-2} sr^{-1} m^{-1}	Spectral Radiance
λ	m	Wavelength
h	J s	Planck's Constant
c	m s	Speed of Light
k	Js−1	Boltzmann Constant
T	K	Temperature
E_λ	J	Photon Energy
Φ_λ	ph s^{-1} m^{-2} sr^{-1} m^{-1}	Spectral Photon Flux
Φ	ph s^{-1} m^{-2} sr^{-1}	Photon Flux
t_{int}	s	Integration Time
A	m^2	Detector Area
$\Delta\lambda$	m	Bandwidth
x, y	m	Spatial Domain Coordinates
ξ, η	m^{-1}	Spatial Frequency Domain Coordinates
X	m	Spatial Period/Distance
M	-	Modulation Depth/Contrast
ξ_C	m^{-1}	Cutoff Frequency
$\lambda_{optical}$	m	Electromagnetic Wavelength
MTF	-	Modulation Transfer Function
p_{pitch}	m	Pixel Pitch (Size)
PD	m	Pixel Displacement
$PMAG$	-	Primary Magnification
T	-	Optical Transmission
R_V	VW^{-1}	Responsivity
D	W^{-1}	Detectivity
SNR	-	Signal-to-Noise Ratio
eta	-	Quantum Efficiency
N	ph	Integrated Photon Flux
n_{shot}	ph	Shot Noise

Symbol	Unit	Name
n_{dark}	ph	Dark Noise
$n_{readout}$	ph	Readout Noise
I_{dark}	A	Dark Current
e	As^{-1}	Elementary Charge
FW	e^-	Full Well Capacity
FOV	deg	Field-of-View
n_{pixel}	-	Number of pixels
$iFOV$	mrad	Instanteneous Field-of-View
h	m	Orbit Altitude
GSD	m	Ground Sampling Distance
PS	-	Pixel Smear
v_{ground}	ms^{-1}	Ground velocity
μ_V	$m^3kg^2s^{-2}$	Gravitational Constant
R_V	m	Radius of Venus
$v_{V,rot}$	ms^{-1}	Rotational velocity of Venus
b	-	Binning Factor
s	-	Stacking Factor
d	m	Distance
a	-	Albedo radiation Factor
S	Wm^{-2}	Solar Constant
α_λ, β_λ	-	Limb Darkening Parameters
θ	deg	Incidence Angle
ν	Hz	Electromagnetic Frequency
I	R	Rayleigh Emission
σ	-	Standard Deviation
M_S	-	Surface Magnitude

List of Acronyms

Acronym	Definition
VEM	Venus Express Mission
VIRTIS	Visible and InfraRed Thermal Imaging Spectrometer
CaSSIS	Colour and Stereo Surface Imaging System
NIRS	Near Infrared Spectrometer
MTF	Modulation Transfer Function
PSF	Point Spread Function
PD	Pixel Displacement
PMAG	Primary Magnification
CWL	Center Wavelength
FWHM	Full Width Half Maximum
SWIR	Short Wavelength Infrared
MWIR	Middle Wavelength Infrared
NEP	Noise Equivalent Power
SNR	Signal-to-Noise Ratio
A/D	Analog-to-Digital
FW	Full Well
FOV	Field-of-View
iFOV	Instananeous Field-of-View
GSD	Ground Sampling Distance
AU	Astronomical Unit
NLTE	Non-Local-Thermodynamic-Equilibrium
VER	Volume Emission Rate
IER	Integrated Emission Rate
SZA	Solar Zenith Angle
EA	Emission Angle
VAMOS	Venusian Atmosphere Measurements and Orbiter for Seismicity
MR	Mission Requirement
MC	Mission Constraint
FoM	Figure-of-Merit
JWST	James Webb Space Telescope
VEM	Venus Emissivity Mapper
SCD	SemiConductor Devices
LG/MG/HG	Low/Medium/High Gain

1 Introduction

In the history of Venus exploration, previous missions such as the European Space Agency's (ESA) Venus Express mission (VEM) and the Japan Aerospace Exploration Agency's (JAXA) Akatsuki mission have significantly advanced our understanding of the fascinating planet. The Venus Express mission, which operated from 2006 to 2014, provided invaluable insights into Venus' atmosphere, surface and interactions with the solar wind through a suite of instruments including spectrometers and imaging systems [34, 35]. Similarly, the Akatsuki spacecraft, launched in 2010, has been essential in studying Venus' atmospheric dynamics and cloud formation processes using infrared cameras and other instruments [20, 21, 32].

In recent years, the exploration of Venus has received new emphasis with the selection of the upcoming NASA VERITAS and ESA EnVision missions, marking a renewed focus on discovering more about Venus. Despite this new dynamic in the exploration of Venus, the understanding of Venus' internal structure is still very limited, mainly due to the enormous challenges posed by the planet's harsh surface conditions, including extreme temperatures that do not favour direct seismic measurements. However, preliminary studies have revealed the promising option of measuring seismic activity via remote sensing of the Venusian atmosphere from orbit.

Missions to the Venusian surface equipped with seismometers would face immense challenges, including very limited lifetime and enormous complexity. The search for new insights into the interior dynamics, crustal dynamics and seismic activity of Venus has therefore led to a rising interest in using orbital measurements in the infrared spectrum to investigate seismic activity over it's atmosphere as suggested by [29] and further investigated by [43]. By exploiting the phenomenon atmospheric-coupled Rayleigh waves, which reveals pressure waves in the atmosphere, orbital infrared measurements offer a more robust and cost-effective way of detecting seismic activity on Venus.

Two specific wavelengths have been suggested for the observation of propagating seismic waves in the Venusian atmosphere at 4.3 µm on the dayside and at 1.27 µm on the nightside of Venus, which have already been observed by the Visible and InfraRed Thermal Imaging Spectrometer (VIRTIS) on board the VEM mission [35, 34], but without being utilised for the detection of seismic activity in the Venusian atmosphere.

Within this context, this thesis aims to specify the main parameters of a potential instrumentation for a small satellite mission, based on an infrared detector. The main focus will

be to derive an initial instrument design capable of detecting seismic activity in the Venusian atmosphere by space-based remote sensing. This effort will involve several disciplines, including radiometry, optics, infrared detectors, remote sensing, image processing, and planetary science for Venus. Key objectives include identifying measurement and detection requirements, examining signal-to-noise ratio performance, performing trade-off studies for sensor and optics selection, and ultimately deriving an instrument concept that will be optimised to meet the mission objective.

This work aims to address the central challenge in the understanding of the study of Venus internal dynamics and proposes an unique approach of measuring seismic activity from orbit. By overcoming the limitations of surface measurements and using a cutting-edge remote sensing technique, this work has the potential to improve the understanding of seismic activity of Venus and contribute to further scientific pursuits in planetary exploration of seismic activity.
The primary objective of this thesis is to assess the feasibility of detecting seismic activity in the Venusian atmosphere using space-based remote sensing, and to derive an initial design for an infrared camera for a small satellite mission.

First of all, the theoretical background chapters provide a comprehensive overview of radiometry, optics, infrared detectors, remote sensing, image processing and planetary science for Venus, in particular the study of the background signals at 1.27 µm and 4.3 µm as well as the target signal of the atmospheric-coupled seismic Rayleigh waves together with general properties of Venus are fundamental for the following chapters of this thesis. Combining all these disciplines will provide the framework of defining the imaging system based on the approach of [11].

The mission definition chapter will then outline the precise objectives, requirements, constraints, figures of merit and system drivers for the proposed instrumentation on board of a small satellite mission along with the definition of a baseline design of the imaging system and derived cases for the expected seismic and background signals.

The subsequent chapters focus on trade-off analysis and evaluation, especially focusing on the detectivity and spatial resolution performance in order to determine if the imaging system is able to detect and observe seismic waves in the Venusian atmosphere, which results in the derivation of a preliminary design of the imaging system for observing the day- and nightside. Finally, the thesis concludes with a summary of the key results and an outlook on the future directions of the payload design process.

2 Theoretical Background

The theoretical framework for the design of an infrared camera for a small satellite mission to Venus involves a multidisciplinary synthesis of advanced concepts in radiometry, optics, infrared detectors, planetary science, remote sensing, and image processing. The framework applied in this thesis is based on the imaging chain model by [11], shown in Fig. 2.1. This allows the complex design of the infrared camera system to be structured and the links between the elements of the imaging chain to be clearly shown. The theoretical background will also provide the foundation for the mathematical models used in order to model the radiometry, optics and the sensor in combination with the space-based remote sensing in order to evaluate the feasibility of detecting Rayleigh surface waves in the Venusian atmosphere. In Fig. 2.1, radiometry sets the framework for understanding the fundamental properties of

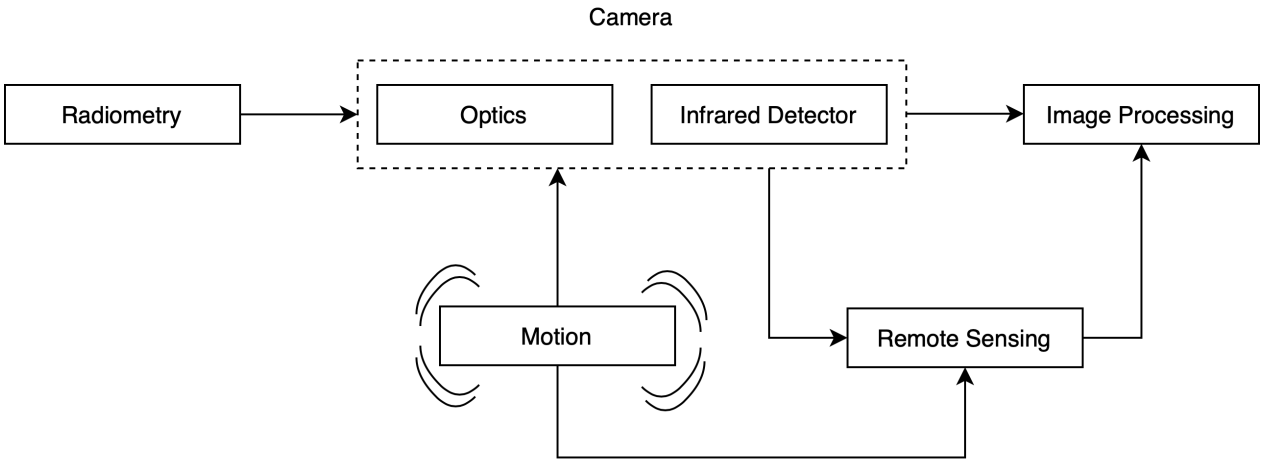

Figure 2.1: Imaging chain model as a framework to design an infrared camera system for remote sensing from orbit

electromagnetic radiation that will create the desired image. This is followed by an explanation of the basic geometrical-optics concepts and the introduction of the modulation transfer function as a measure of image quality in terms of contrast. A definition of the principle of an infrared detector and its defining parameters is essential as it is responsible for converting captured electromagnetic radiation into a digital image. Possible ways of enhancing image quality are later discussed in the section on image processing. In order to be able to derive the system requirements in connection with the imaging chain later on, important characteristics of Venus must be outlined. The definition of airglow and Rayleigh surface waves and

their interaction will provide the basis for the mission objective of measuring seismic activity in the Venusian atmosphere from orbit.

2.1 Radiometry

The spectral radiance distribution is crucial for estimating the expected background radiation from Venus when observing in the infrared spectrum. It is defined as the amount of power a surface emits or reflects in a particular direction per unit wavelength, per unit area perpendicular to that direction, per unit solid angle. The solid angle Ω, measured in [sr], is commonly known as the angle that subtends a given area on the surface of a unit sphere and can be defined with the inverse camera equation as in [51].

$$\Omega = \frac{\pi}{1 + 4(f/\#)^2} \tag{2.1}$$

The f-number $f/\#$ is given by the ratio of focal length f and aperture diameter D, which will be explained in detail in the next chapter, since it these are optical characteristics. In the infrared spectrum the spectral radiance is commonly measured in [W $\mathrm{sr}^{-1}\mathrm{m}^{-2}\mu\mathrm{m}^{-1}$] [11].

In general, the spectral radiance profile L_λ of a planet can be divided into two components. First, the reflected solar spectrum, which constitutes the sunlight reflected by the planet's surface and atmosphere. The amount of reflected sunlight depends on the albedo of the planet, which is the fraction of solar energy that is reflected back into space. The reflected solar spectrum is generally more dominant at shorter wavelengths, particularly in the visible range.
Secondly, planets also emit radiation on their own due to their thermal energy commonly known as blackbody radiation, which is determined by their effective blackbody temperature T_{bb}. A blackbody is an idealised object that absorbs all radiation it is exposed to and emits 100% of the absorbed radiation [51]. Consequently, the total spectral radiance can be described as the sum of the reflected solar radiance $L_{\lambda,solar}$ and the emitted thermal radiance $L_{\lambda,thermal}$:

$$L_{\lambda,total} = L_{\lambda,solar} + L_{\lambda,thermal}. \tag{2.2}$$

Both components can be modeled using Planck's law, which is defined as in [11]:

$$L_\lambda = \frac{2hc^2}{\lambda^5}\left(\frac{1}{e^{\frac{hc}{kT\lambda}} - 1}\right) \tag{2.3}$$

where $h = 6.6261 \cdot 10^{-34}$ Js constitutes Planck's constant, $c = 2.9979 \cdot 10^8$ m/s is the speed of electromagnetic waves in a vacuum, $k = 1.3807 \cdot 10^{-23}$ J/K is the Boltzmann constant, T is the effective blackbody temperature in [K] and λ is the wavelength in units of [µm].

In order to accurately analyse the spectral radiance profile of Venus, it is necessary to consider both components and how they vary with wavelength due to the characteristics of Venus (see section 2.6). Understanding these profiles is crucial for the investigation of both, the day- and nightside background signals. However, the spectral radiance distribution will not be

derived from Planck's law in this thesis. Instead, it will be derived from actual measurements in the range of the target wavelengths in the infrared spectrum, which will also be discussed in section 2.6. Nonetheless, understanding the origin of the measured background signals requires knowledge of the spectral radiance distribution derived with Planck's law.

An essential parameter related to the spectral radiance is the photon flux Φ, which is the number of photons reaching the detector per second. It therefore affects the performance of the detector with respect to the saturation of a pixel (see section 2.3). The spectral photon flux can be derived directly from the spectral radiance and is given by

$$\Phi_\lambda = \frac{L_\lambda}{E_\lambda} \tag{2.4}$$

where E_λ is the energy of a photon in [J] corresponding to the electromagnetic wavelength λ [11] and is given by:

$$E_\lambda = \frac{h \cdot c}{\lambda} \tag{2.5}$$

The result of equation 2.4 provides the number of photons per unit area, time, wavelength and steradian [photons $s^{-1}m^{-2}\mu m^{-1}sr^{-1}$]. The total number of photons over a wavelength range (determined by optical filter bandpass) for a certain integration time, detector (pixel) area and solid angle can be obtained by integrating the spectral photon flux over all parameters [51]:

$$\Phi = \int_0^{t_{int}} \int_0^{A} \int_{\lambda_1}^{\lambda_2} \int_0^{\Omega} \Phi_\lambda \, dt \, dA \, d\lambda \, d\Omega \tag{2.6}$$

$$\Longleftrightarrow \Phi = t_{int} \cdot A \cdot \Omega \int_{\lambda_1}^{\lambda_2} \Phi_\lambda \, d\lambda. \tag{2.7}$$

Therefore, the photon flux is a crucial parameter for designing the infrared camera as it involves several design choices simultaneously, including the sizing of the imaging system with the f-number (see eq. 2.1), detector selection and therefore pixel size (see section 2.3), selection of the bandpass corresponding to the observed wavelength and the integration time itself.

2.2 Optics

The basic concept of a camera refers to the geometric relationship between the object, the image and the optical elements, e.g. a convex lens in between. In this context the focal length f is one of the most essential parameters and refers to the distance between the lens and the produced image [11]. This relies on the assumption that the distance between the object and the lens is sufficiently large, a condition typically met in the context of remote sensing from space. In addition to that, one can define another essential optical design parameter called the f-number $f/\#$ and is defined as the ratio of the focal length f to the optics aperture diameter D [11]:

$$f/\# = \frac{f}{D} \tag{2.8}$$

The choice of values for these parameters depends on the application and the focal length can have a wide range up to 880 mm in the case of CaSSIS onboard the ExoMars Trace Gas Orbiter [46], while the f-number lies typically between 1.0 (e.g. NIRS3 spectrometer for Hayabusa [21]) and 8.0 (e.g. Infrared Camera 1 for Akatsuki [20, 32]).

2.2.1 Modulation Transfer Function

One of the parameters used to examine the optical performance of an imaging system is the Modulation Transfer Function (MTF). The analysis of the optical performance using the MTF is performed from a frequency domain perspective. Just as electrical signals in the time domain consist of various frequencies, the (ir-)radiance distribution within the taken images, due to the collected light during the integration time, consists of spatial frequencies. This analogy leads to the application of the Fourier transformation to images [11] in order to apply the MTF. The key relation between the image in the spatial and frequency domain is given by the convolution theorem [11]

$$g(x,y) = h(x,y) * f(x,y) = \mathcal{F}^{-1}\big\{\mathcal{F}\{h(x,y)\} \cdot \mathcal{F}\{f(x,y)\}\big\} = \mathcal{F}^{-1}\{H(\xi,\eta) \cdot F(\xi,\eta)\} \quad (2.9)$$

where $f(x,y)$ describes the radiance distribution of the taken image in the spatial domain, while $h(x,y)$ constitutes the corresponding point spread function (PSF). $F(\xi,\eta)$ is the Fourier transformation of the taken image, while $H(\xi,\eta)$ is the corresponding MTF. What makes this method so advantageous is that the convolution operation required in the spatial domain is done by a simple multiplication of the fourier transformed image and the MTF in the frequency domain and the subsequently inverse Fourier transformation to model blurring in the image (Fig. 2.2). The Fourier transformation, multiplication and subsequent inverse transformation are mathematically easier to perform than the convolution. Nevertheless, a better understanding of the MTF is required and shall be explained in detail below.

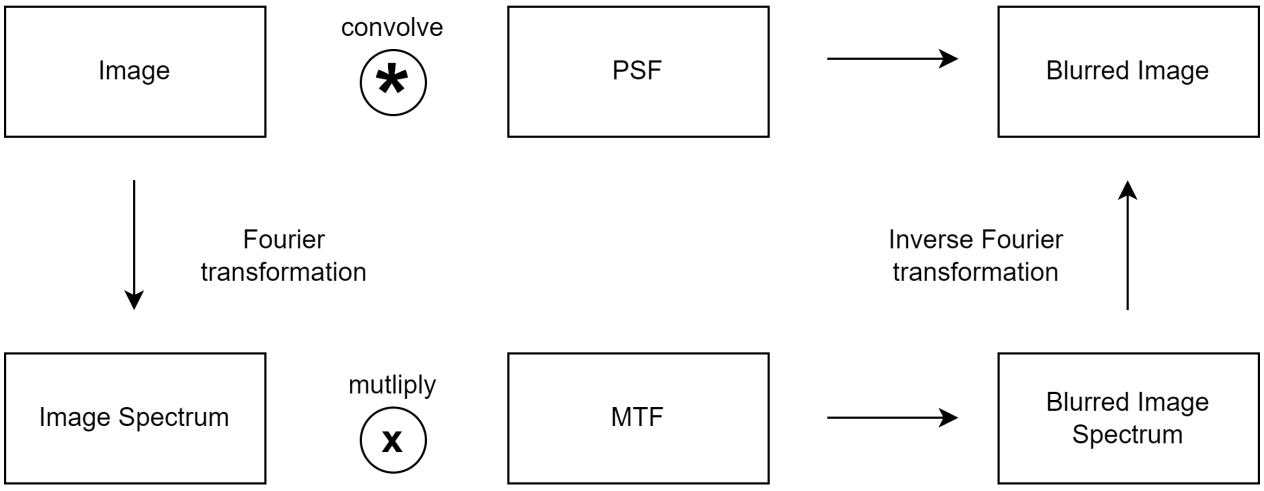

Figure 2.2: Relation between the spatial and frequency domain through the convolution theorem in order to examine the optical performance of the imaging system design when applying the MTF in the frequency domain

First of all, the MTF is defined in the spatial domain and therefore the spatial frequency has to be defined as $\xi = 1/X$, where X constitutes the spatial period or distance. For optical systems the spatial frequency is often expressed in cycles/mm [cy/mm] or line pairs/mm [lp/mm], where one cycle equals one black/white line pair or one period of a wave [5]. The definition of the MTF is based on the modulation depth M, which can also be seen as a measure of the contrast of an image and is defined by the amplitude of the irradiance E of the taken image

$$M = \frac{E_{max} - E_{min}}{E_{max} + E_{min}} \tag{2.10}$$

where E_{min} and E_{max} are the minimum and maximum irradiance values in the image. This leads to the general definition of the MTF [5]:

$$MTF(\xi) = \frac{M_{image}(\xi)}{M_{object}} \tag{2.11}$$

where M_{obj} is the object modulation depth and does not vary with respect to ξ, while the image modulation depth M_{img} decreases with increasing spatial frequencies until no spatial variation of irradiance exists in the image (MTF = 0) [5]. For MTF = 1 there will be no change in the resolution at higher spatial frequencies and therefore no degradation of the image quality regarding blur. Hence, the dependency on the spatial frequencies of the seismic Rayleigh waves will be crucial when analysing the optical performance with the MTF of the imaging system.

The calculation and investigation of the MTF will be crucial for analysing optical performance in terms of spatial resolution. Besides the spatial resolution being specified with the ground sampling distance (see section 2.4), the resolution can be defined in the spatial frequency domain as the frequency at which the MTF falls below a particular threshold [5] and shall be defined later in this thesis as the limit of required resolution with $MTF_{threshold}$.

The infrared camera as an imaging system also constitutes an electro-optical system, which constists of optics, detectors, electronics, signal processors and displays. Consequently, the components of an electro-optical system influence the optical performance in terms of the MTF as well, which is why the definition of the MTF regarding the detector footprint, sampling and motion blur needs to be taken into account.
First of all, the MTF will be evaluated for a circular, aberration-free lens as it is the only optical element. Since the PSF is assumed for diffraction-limited optical systems [5], it leads to the definition of the related cutoff-frequency with

$$\xi_C = \frac{1}{\lambda_{optical} \cdot f\#} \tag{2.12}$$

where $\lambda_{optical}$ corresponds to the electromagnetic wavelength of the considered background radiation (see section 2.6). The corresponding MTF for the diffraction-limited lens is now given by

$$MTF_{lens}(\phi) = \frac{2}{\pi} \cdot (\phi - \cos\phi \cdot \sin\phi) \text{ with } \phi = \cos^{-1}\left(\frac{\xi}{\xi_C}\right) \tag{2.13}$$

For $\xi > \xi_C$, $\mathrm{MTF}_{\mathrm{lens}}(\phi)$ is set to zero and it should be noted that an optical system cannot perform better than its diffraction-limited MTF as any aberrations will only decrease the MTF [5]. Note also that with the definition of ξ_C in equation 2.12 the diffraction blur will increase as f and/or $\lambda_{optical}$ increases or as the aperture size decreases (see eq. 2.8).

Infrared camera systems as an electro-optical system do not only consist of optical elements, but also detector arrays. Therefore, it is necessary to consider several MTF components affecting the optical performance of the imaging system. Each single squared pixel of the detector array with size $p_{pitch} \times p_{pitch}$ performs spatial averaging of the irradiance falling onto the detector, which is a crucial aspect for analyzing the optical performance for any imaging system with detectors [5]. The corresponding MTF component can be calculated with the absolute of the normalized sinc function:

$$MTF_{footprint}(\xi) = |\mathrm{sinc}(\xi \cdot p_{pitch})| = \left| \frac{\sin(\pi \xi p_{pitch})}{\pi \xi p_{pitch}} \right| \tag{2.14}$$

Another MTF component considers the fact that irradiance from the image might not fall into one single pixel/column of the detector array but into two adjacent pixels/columns. As shown by [5] one can use the sampling MTF component defined with:

$$MTF_{sampling}(\xi) = |\mathrm{sinc}(\xi \cdot p_{pitch})| \tag{2.15}$$

Finally, the motion of the spacecraft relative to the object can be considered as another MTF component given by

$$MTF_{motion}(\xi) = |\mathrm{sinc}(\xi \cdot PD)| \tag{2.16}$$

which can further reduce the image quality due to the pixel displacement PD, which is the product of the pixel smear (defined in section 2.3) and the pixel size p_{pitch} [42].
In order to determine all degrading features of the produced image in terms of contrast, one has to multiply all previous mentioned MTF components:

$$MTF_{total} = \prod_i MTF_i. \tag{2.17}$$

Considering the application of the MTF in 2D for applying the MTF to the Fourier transformation of the image, one has to calculate the matrix product (element-wise) of the MTF with the corresponding spatial frequencies included in the image spectrum for each MTF component as

$$MTF_{component}(\xi, \eta) = MTF_{component}(\xi) \cdot MTF_{component}(\eta) \tag{2.18}$$

where ξ and η are the spatial frequencies corresponding to x and y in the spatial domain, respectively. Other MTF components such as image vibration, atmospheric turbulence, etc. [5], although relevant in a broader context of the image quality examination, fall outside the scope of this thesis. This delineation allows for a more focused and in-depth investigation of the selected MTF components, ensuring a targeted and detailed study within the defined parameters of this thesis.

As the targeted seismic Rayleigh waves have varying wavelengths depending on their frequency and propagation speed, their spatial frequencies and consequently the optical performance regarding the spatial resolution of the optical system also varies. To convert the spatial frequency of Rayleigh waves in the object space ξ_{obj} to spatial frequencies on the detector ξ_{img}, the primary magnification PMAG (see section 2.4) of the system needs to be taken into account

$$\xi_{obj} = PMAG \cdot \xi_{img}, \tag{2.19}$$

The relationship between the spatial frequencies in image and object space is therefore essential because the spatial frequencies of the Rayleigh waves are defined by their wavelength in the object space. However, the optical performance of the imaging system is defined in the image space and the conversion from image to object space or vice versa is therefore indispensable in order to be able to analyse the optical performance with regard to the observation of Rayleigh waves. The spatial resolution of the seismic waves can therefore lead to a reduction of the contrast making it harder to distinguish between dips and peaks of the seismic waves in the image in order to detect them.

2.2.2 Optical Filters

As mentioned in the previous chapter, the incoming electromagnetic signal must be limited for a certain range of wavelengths (see eq. 2.7) in order to derive the expected number of photons reaching the detector. This limitation can be achieved by using an optical filter, which allows a certain part of the electromagnetic spectrum to pass through while blocking other parts. Optical filters can be divided into categories such as longpass, shortpass and bandpass filters, hence their specifications should be understood in order to effectively understand and determine which filter is best for the application [7].

Longpass filters transmit wavelengths longer than the specific cut-off wavelength of the filter, while shortpass filters transmit wavelengths shorter than a specific cut-off wavelength. A bandpass filter can be interpreted as a combination of a longpass and a shortpass filter resulting in transmission over a certain wavelength range (bandwidth). Two characteristic parameters are required to define the bandwidth: the centre wavelength (CWL) and the full width half maximum (FWHM). The CWL refers to the centre of the spectral bandwidth, while the FWHM describes the spectral bandwidth over which the bandpass filter transmits. It is defined by the wavelengths, analogous to the cut-on and cut-off wavelengths of the long- and shortpass filter, at which the filter reaches 50% of its maximum transmission. The peak transmission within the FWHM is highly dependent on the specific optical filter, but usually has values between 70 and 90%. The transmission T has to be considered in the estimation of the incoming photon flux to the detector given by

$$\Phi = T \cdot \Phi_{perfect}, \tag{2.20}$$

where Φ_{total} is the photon flux with perfect transmission as defined in chapter 2.1 (see eq. 2.4). Therefore, a suitable optical filter must be determined depending on the application, which will be specified later in this thesis.

2.3 Infrared Detectors

In this chapter the basic principle of the "heart of an infrared system" [51], the detector, will be explained along with its characterisation, focusing on infrared detectors operating in the wavelength range relevant to the detection of seismic activity in the Venusian atmosphere. Furthermore, the theoretical aspects of infrared detectors will be addressed, including a detailed examination of the essential figures of merit, especially the signal-to-noise ratio as the primary performance metric in this thesis. The chapter also examines fundamental performance limitations to provide a comprehensive understanding of the capabilities and constraints of these detectors.

2.3.1 Classification

The majority of optical detectors can be divided into two categories: thermal detectors and photon detectors [39]. Photon detectors exhibit both good signal-to-noise performance and a very fast response, but to achieve this, the photon infrared detectors may require cryogenic cooling ([39]) as dark noise increases at higher operational temperatures. In comparison to that, thermal detectors have relatively lower sensitivity and slower response compared to photon detectors. This characteristic makes them less suitable for applications requiring high sensitivity and speed, consequently this thesis will focus on photon detectors. The latter can be further divided into intrinsic, extrinsic and photoemissive detectors (Schottky barriers). Extrinsic detectors require much more cooling to achieve high sensitivity for a given spectral response cutoff in comparison with intrinsic detectors and the trend that higher wavelengths require lower operating temperatures of the infrared detectors can be seen in [39]. Intrinsic detectors, on the other hand, are most common at short wavelengths below 20 µm according to [39] and are typically composed of semiconductor alloys, but even for this specific type of infrared detectors the operating temperature can vary between 30 K to 300 K [39]. The most dominant semiconductor has been mercury cadmium telluride (HgCdTe). The short wavelength infrared (SWIR) range from 1 µm to 3 µm has been dominated by III–V semiconductor compounds based on indium, such as InGaAs, InAs, InSb, InAsSb [38]. HgCdTe exhibits extreme flexibility, it can be tailored for optimised detection in any region of the IR spectrum, specifically wavelength tunability and high quantum efficiency have made HgCdTe the preferred material [37]. Nevertheless, [37] also states that there are some InGaAs photodiodes that can compete with the performance of HgCdTe photodiodes.

2.3.2 Figures of Merit

Figures of merit are critical parameters used to evaluate and compare the performance of different detectors. In the following the most important figures of merit will be explained in order to finally introduce the signal-to-noise ratio as the only figure of merit, which will be the focus in the scope of this thesis.

The responsivity R_V refers to the detector's ability to convert incoming (infrared) radiation into an electrical signal, which dependends on the observed electromagnetic wavelength. A higher responsivity indicates a more sensitive detector capable of detecting lower signals.

Based on this, one can define the noise equivalent power (NEP) in [W], which represents the signal level that produces a signal-to-noise ratio of 1 [39]. The reciprocal of the NEP can then be used to define the detectivity D [39]:

$$D = \frac{1}{NEP} \tag{2.21}$$

Normalising the detectivity leads to one of the most important figures of merit, D-star D^*, which allows the comparison of detectors of the same type ([37]) across the electromagnetic spectrum.
However, the figure of merit that will be used for analysing the performance of the infrared system in this thesis is the signal-to-noise ratio (SNR). It measures the strength of the signal relative to the variation of the background signal and given by [10, 19]:

$$SNR = \frac{\eta \cdot N_{Signal}}{\sqrt{n_{shot}^2 + n_{dark}^2 + n_{readout}^2}} \tag{2.22}$$

The quantum efficiency η is another figure of merit regarding the performance of infrared detectors and refers to the proportion of incoming photons that are successfully converted into electrons, thereby contributing to the electrical signal [39]. A quantum efficiency of one would indicate an optimal conversion rate, so that every photon would be converted into an electron, while a quantum efficiency of zero, would mean that no electrical signal is being generated by the electromagnetic radiation. N_{Signal} is the number of photons generated by the atmospheric coupled Rayleigh waves, given by equation 2.7. The denominator of the fraction represents the noise, which is composed of three components: shot noise n_{shot}, dark noise n_{dark} and readout noise $n_{readout}$. The shot noise can be well approximated by a normal distribution with the total number of photons

$$n_{shot} = \sqrt{\eta \cdot (N_{Signal} + N_{background})} \tag{2.23}$$

reflecting the statistical variation in photon detection. Thermal activity within the detector generates the dark noise

$$n_{dark} = \sqrt{I_{dark} \cdot t_{int}} \tag{2.24}$$

which depends on the integration time t_{int} as well as on the dark current I_{dark}, which is mostly given in [A] by technical data sheets and can be converted using

$$I_{dark}[e^-/s] = \frac{I_{dark}[A]}{e} \tag{2.25}$$

where $e = 1.602 \cdot 10^{-19}$ As^{-1} is the elementary charge. A low operating temperature would therefore the best design option to mitigate the dark noise of the detector. Lastly, readout noise $n_{readout}$ in [e^-] is generated by amplifying the electrical signal through analogue-to-digital (A/D) conversion. Therefore, it is highly dependent on the electronics of the detector, which is beyond the scope of this thesis. The performance of infrared detectors is optimised when the dark and readout noise components are comparably low to the shot noise [39]. The conversion efficiency α is assumed to be one, since it depends on the properties of the electronics, which are not included in this thesis.

Beyond the previously described figures of merit, there are also indicators that relate to the limitations of the performance of an infrared detector. One of these is the full well capacity (FW) in [e^-], which sets the maximum of charge that can be accumulated by a single pixel. Once the full well capacity is reached, no more photons can be collected and the detector is therefore saturated. This leads to the limitation of the integration time with

$$t_{int,\,max} = \frac{FW}{\Phi} \tag{2.26}$$

where Φ is the photon flux in photons per second.

2.4 Remote Sensing

The importance of remote sensing parameters when developing imaging systems is immense, as they have a direct impact on the quality and applicability of the captured image. Among these parameters, the field of view (FOV) of a camera on board a spacecraft is the angular range of the image scene and thus critical for determining the coverage. It can be calculated in each direction (x, y) by using the trigonometric relation

$$FOV_{x/y} = 2\arctan\left(\frac{p_{pitch} \cdot n_{pixel,x/y}}{2f}\right) \tag{2.27}$$

where p_{pitch} is the pixel size and $n_{pixel,x/y}$ are the number of pixels in the x and y direction of the used detector. In addition, f constitutes the focal length and consequently it is evident that the FOV depends on the detector selection and size of imaging system. Furthermore, one can derive this relation for a single pixel of the detector, which gives the instantaneous field of view (iFOV) representing the angular range of a single pixel of the detector by:

$$iFOV = 2\arctan\left(\frac{p_{pitch}}{2f}\right) \tag{2.28}$$

and is usually measured in [mrad]. Based on the definition of the iFOV, it is now possible to define the ground sampling distance (GSD), which is the projected size of one pixel of the detector on the ground and therefore a measure of the spatial resolution capability of the imaging system. The calculation is done by multiplying the iFOV in [rad] with the orbit altitude h:

$$GSD = iFOV \cdot h \tag{2.29}$$

The primary magnification (PMAG), as already mentioned in section 2.2, measures how much an image of an object is magnified when captured by an imaging system given by the ratio of the pixel size and the ground sampling distance [5]:

$$PMAG = \frac{p_{pitch}}{GSD} \tag{2.30}$$

Another essential aspect for remote sensing instruments is that the orbiting camera and Venus are not stationary. Therefore, blurring effect caused by motion have to be considered by defining the pixel smear PS given by:

$$PS = \frac{v_{ground} \cdot t_{int}}{GSD}, \tag{2.31}$$

where v_{ground} refers to the relative velocity of the spacecraft in orbit relative to the ground. Note that the rotational velocity of Venus $v_{V,rot}$ must also be taken into account to be precise. The velocity of the spacecraft can be derived by using the fundamental vis-viva equation as given in many space engineering textbooks, such as [31]. Assuming that the spacecraft is orbiting Venus in the opposite direction to its rotation, v_{ground} can be defined as

$$v_{ground} = \frac{1}{1 + \frac{h}{R_V}} \sqrt{\frac{\mu_V}{h + R_V}} - v_{V,rot}, \tag{2.32}$$

where μ_V is the product of the gravitational constant $\gamma = 6.674301 \cdot 10^{-11}$ $\mathrm{m^3 kg^2 s^{-2}}$ and the mass of Venus. R_V and $v_{V,rot}$ are the radius and already mentioned rotational velotiy of Venus, respectively (see section 2.6).

2.5 Image Processing

In the context of space-based remote sensing, image processing plays a pivotal role in enhancing the quality and utility of data captured by sensors aboard satellites or space probes. Among the many techniques employed, binning and stacking are particularly relevant because of their straight-forward approaches improving the signal-to-noise ratio. These methods are designed to overcome the inherent challenges posed by space environments, such as limited light conditions, high relative motion between the sensor and the target, and the need for efficient data transmission.

Pixel binning is the combination of charge from adjacent pixels in the sensor array, effectively reducing the image's spatial resolution in exchange for an enhanced SNR [10]. The readout noise is the only noise component, which does not change with binning, as it is associated with the electronic noise introduced during the readout process and is independent of the number of binned pixels [10]. This process can be performed either during the image capture phase within the sensor hardware or with post-processing software algorithms. For instance, in 2 x 2 binning ($b = 2$), an array of 16 pixels is combined into 4 larger pixels, resulting in a reduction of the total number of pixels to $1/4$ and hence halving the image resolution in each dimension. The primary advantage of binning is the significant improvement in SNR (see eq.), where the binning factor b affects not only the signal photon flux N_{Signal}, but also the total photon flux thus increasing shot and dark noise as well. The readout noise is not affected when binning is applied [44]. Nevertheless binning improves the SNR by a factor of approximately $\sqrt{b}$, which might be necessary if the SNR is too low for detecting seismic activity in Venus' atmosphere with this approach. However, the main drawback of binning is the loss of spatial resolution given by

$$GSD = iFOV \cdot h \cdot b \tag{2.33}$$

as multiple pixels are combined into a single larger pixel. Therefore, this must be considered as a trade-off when analysing the system performance of the imaging system.
Another image processing technique to improve the final image quality in terms of SNR is called stacking, where multiple images of the same scene are superimposed and aligned

[36]. Stacking enhances the SNR by averaging out random noise across the stacked images s while reinforcing SNR without reducing the spatial resolution as it does with binning, which ultimately gives the improved SNR by:

$$SNR = \frac{\eta \cdot N_{Signal} \cdot b \cdot \sqrt{s}}{\sqrt{n_{shot}^2 \cdot b + n_{dark}^2 \cdot b + n_{readout}^2}} \tag{2.34}$$

However, the use of stacking is only considerable if the integration time with respect to the full well capacity is not exceeded:

$$t_{int,\,max} = \frac{FW}{\Phi \cdot s} \tag{2.35}$$

which leads to a further limitation of the integration time. Furthermore, stacking requires precise alignment of multiple images, which can be challenging due to the motion of the seismic Rayleigh waves, Venus and the spacecraft itself [11]. Figure 2.3 shows an exemplary use of both image processing methods.

Assuming an SNR = 1 per pixel, the SNR would not change with b = s = 1 and therefore the GSD and maximum integration time would not change. When b = 2, the GSD is doubled and thus the spatial resolution of the imaging system is halved, but the SNR is increased by $\sqrt{2}$ (SNR = 1.41). For b = 4, the GSD is quadrupled according to equation 2.33 and thus the spatial resolution is quartered, but the SNR is doubled (SNR = 2.
A similar trade-off occurs when using stacking, e.g. if 5 images are stacked (Fig. 2.3), the SNR can be increased by a factor of $\sqrt{5}$ in each pixel to SNR = 2.24 (without binning), but a maximum integration time of 5s would be reduced to 1s and thus also the photon flux (see eq. 2.4), which in turn affects again the SNR. Therefore, binning and stacking together can significantly increase the SNR at the expense of spatial and temporal resolution.

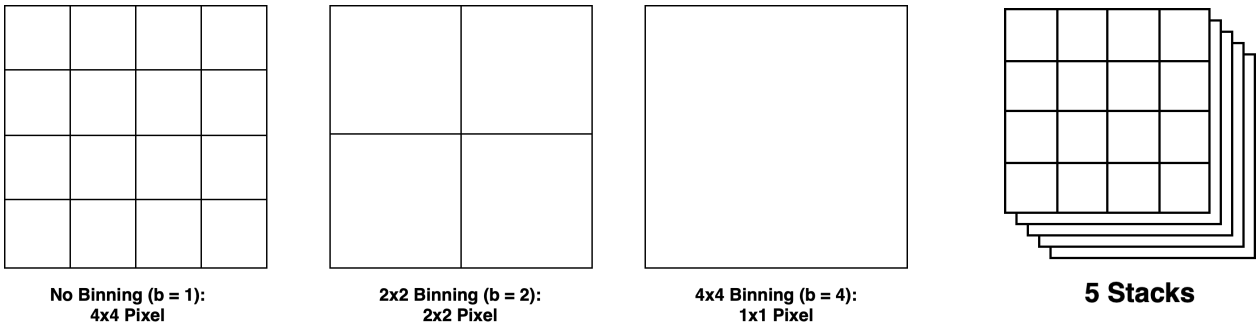

Figure 2.3: Exemplary illustration for the application of image processing methods binning (left) and stacking (right)

2.6 General Characteristics of Venus

Venus is one of the four terrestrial planets in the Solar System and with a radius of 6051 km and a mass of $4.867 \cdot 10^{23}$ kg it is similar yet smaller in size compared to Earth [50]. Venus is also the second closest planet to the Sun, after Mercury and before Earth, and is about 0.72 astronomical units (AU) from the Sun. Therefore, it takes Venus only 243 Earth days to rotate around the Sun. However, the axis of Venus is tilted by 177°, resulting in a retrograde rotation [50]. A solar day on Venus, which is the time it takes for the Sun to return to the same position in the sky, is rather long with a duration of 117 Earth days. Furthermore, Venus rotates very slowly with just $v_{V,\,rot} = 1.81$ ms^{-1} resulting in a longer (sidereal) day[1] than year. Since Venus is closer to the Sun compared to Earth, solar radiation is higher on Venus based on the inverse-square law:

$$L_{\lambda,\,Solar,\,Venus} = \left(\frac{d_{Sun,Earth}}{d_{Sun,Venus}}\right)^2 \cdot L_{\lambda,\,Solar,\,Earth} \tag{2.36}$$

where $d_{Sun,Earth}$ and $d_{Sun,Venus}$ are the distances of Earth and Venus to the Sun, respectively whereas $L_{\lambda,\,Solar,\,Earth}$ and $L_{\lambda,\,Solar,\,Venus}$ are the incoming spectral solar radiation for Earth and Venus, respectively. Not all radiation coming towards Venus will be reflected back into space. With a very thick cloud layer, Venus is emitting approximately 77% of the incoming solar radiation, which results in an albedo of $a_{Venus} = 0.77$ [26], which is much higher compared to Earth ($a_{Earth} = 0.3$) thus the resulting radiance from reflected sunlight on Venus is given by:

$$L_{\lambda,\,Albedo,\,Venus} = a_{Venus} \cdot L_{\lambda,\,Solar,\,Venus} \tag{2.37}$$

Temperatures at the surface ($\bar{T}_{surface} = 737$ K) are much higher on Venus than on Earth due to the strongest greenhouse effect in the solar system caused by a high concentration of CO_2 [50], however, compared to Earth the blackbody radiation emitted in the infrared spectrum is lower. The opaque and thick cloud layer contains most of the heat, resulting in a lower effective blackbody temperature of 226 K above the clouds [50]. As already explained in section 2.1 the reflected spectral radiance distribution can be determined using Planck's law (Eq. 2.3) considering the two components as in equation 2.2. The total spectral radiance of Venus is ultimately composed of the sum of the reflected solar radiation and the blackbody radiation of Venus given by:

$$L_{\lambda,Venus} = L_{\lambda,\,Blackbody,\,Venus} + L_{\lambda,\,Albedo,\,Venus} \tag{2.38}$$

This results in the graphs seen in figure 2.4. The reflected solar radiation component (yellow) dominates in the electromagnetic spectrum of the visible light through the near-infrared range (0.2 µm to 4 µm). The blackbody radiation (green) prevails at longer infrared wavelengths between 4 µm to 50 µm. Planck's law gives a good approximation of the measured data from [1] (blue). A useful comparison can be made with the solar constant in [Wm^{-2}], which is determined by integrating the spectral radiance in [Wm^{-2}µm^{-1}] over the wavelength and is in excellent agreement with the expected literature values of [1, 50]. Furthermore, the resulting distribution agrees well with the results of [26]. However, the only spectral radiance

[1] One full rotation on its axis relative to the fixed stars

component when observing the wavelength of 1.27 µm refers to the reflected solar radiation, which appears only on the sunlit side of a planet is therefore zero on the nightside of Venus, which would mean that there is no background radiation when observing 1.27 µm O_2 airglow on the nightside, although [26] indicates that there is. Consequently, a consideration of only the reflected solar and blackbody radiation according to Planck's law is not sufficient for the accurate description of the background signal and will therefore be discussed in detail in the following chapter.

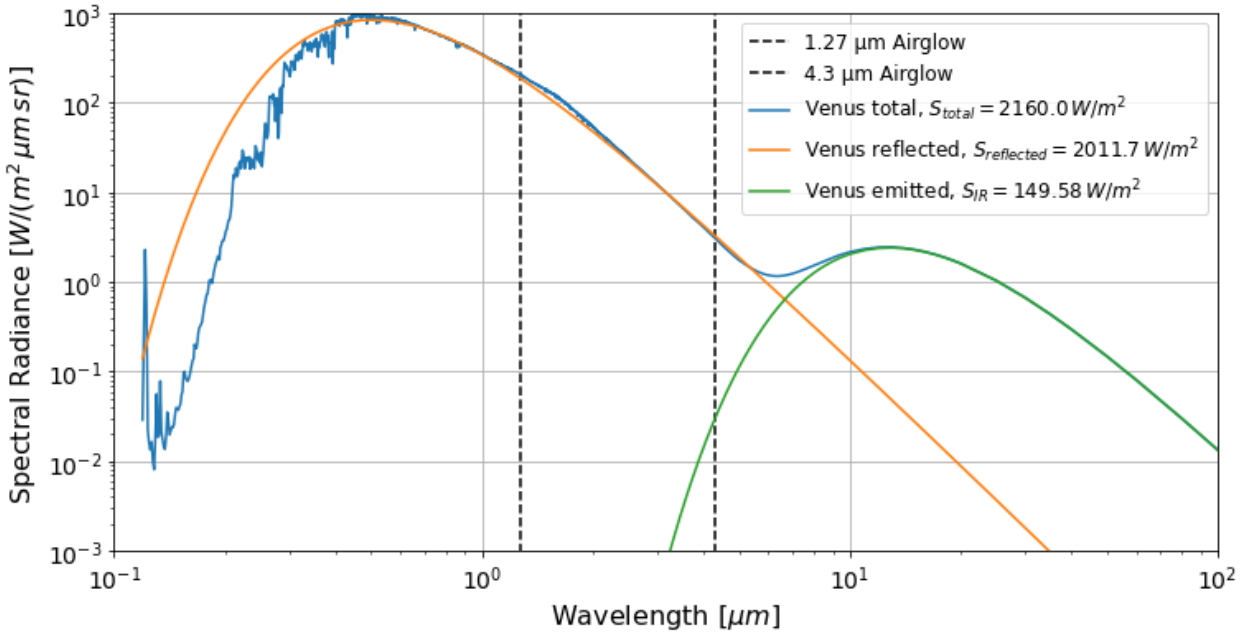

Figure 2.4: Spectral radiance distribution of Venus based on Planck's law with measured data over the electromagntic spectrum from 100 nm to 100 µm

At the Venusian surface, atmospheric pressure is about 90 bar, the density is about 65 kgm^{-3} and the speed of sound is slightly higher (425 ms^{-1}) than on Earth's surface [50, 27]. At an altitude of 50 km in Venusian atmosphere, the pressure is comparable to Earth's surface pressure, but [28] shows that the density is almost two orders of magnitude higher. These two effects mean that, for a given altitude and quake magnitude, atmospheric signals are expected to be about 600 times greater on Venus than on Earth, making orbit-based detection of seismic activity a viable possibility on Venus [29]. Lastly, table 2.1 summarises all the necessary characteristics of Venus mentioned above.

2.7 Limb Darkening

Limb darkening is a critical factor when estimating background radiance signals when observing Venus. The limb darkening effect, described by the limb darkening function, is a reduction in observed radiance with increasing incidence angle [30]. This attenuation results from a greater atmospheric path travelled by the radiation at higher angles of incidence. The limb darkening effect is closely related to several atmospheric properties. Understanding and

Table 2.1: Characteristic properties of Venus

Parameters	Value	Unit
Radius R_V	6051	km
Mass m_V	$4.867 \cdot 10^{23}$	kg
Distance to Sun $d_{Sun,Venus}$	0.723	AU
Rotational velocity $v_{V,rot}$	1.81	m/s
Albedo a_{Venus}	0.77	-
Average surface temperature $\bar{T}_{surface}$	737	K
Effective blackbody temperture $T_{bb,eff}$	226	K

retrieving the limb darkening function not only provides a more accurate estimation of the expected background signal, but also enables the calculation of radiances similar to those obtained in nadir observations and is therefore vital for this thesis.

[30] gives the limb darkening function as a first-order approximation as function of the cosine of emergence angle by:

$$L_\lambda = L_{0,\lambda} \cdot (\alpha_\lambda + \beta_\lambda \cdot \cos(\theta)) \tag{2.39}$$

where $L_{0,\lambda}$ is the radiance that would be observed in a Nadir observation, which will be derived from the assumed values in section 2.8. α_λ and β_λ are the limb darkening parameters corresponding to the observed wavelength, which are independent on the optical depth [30]. Therefore, limb darkening is strongly dependent on the observed wavelength and can vary based on literature, radiative transfer models and measured values with VIRTIS-H at different latitudes [30]. However, for the O_2 airglow signal when observing 1.27 µm on the nightside the limb darkening parameters will be based on the averaged values of $\alpha_{1.27} = 0.4$ and $\beta_{1.27} = 0.6$ from [30] for a wavelength of 1.31 µm as there are no given limb darkening parameters at the exact wavelength of 1.27 µm.
When observing the CO_2 NLTE emission on the dayside at 4.3 µm, the limb darkening parameters are based on the values corresponding to an observed wavelength of 4 µm with $\alpha_{4.3} = 0.2$ and $\beta_{4.3} = 0.8$. As $\beta_{4.3}$ is greater than $\beta_{1.27}$, stronger limb darkening is expected when observing 4.3 µm on the dayside of Venus.

2.8 Atmospheric Airglow on Venus

The study of atmospheric airglow is the key factor in the approach of detecting seismic waves in the atmosphere to obtain information about the planetary interior as proposed by [12, 28, 29]. Therefore, this chapter deals with the investigation of airglow phenomena in the upper atmosphere of Venus, which will later constitute the background signal within the aimed observations of this mission. The two candidates for possible observation of airglow at 1.27 µm and 4.3 µm will be described and characterised based on existing measurements and model calculations.

Airglow can be defined as a faint emission in the ultraviolet, the visible and the near-infrared

spectral range at high atmospheric altitudes. It is a phenomenon that occurs in the upper parts of a planetary atmosphere, such on Earth, Mars and Venus [40]. It is therefore usually not visible from the surface of a planet, but for astronauts, it is easily observed at the edge of Earth's nightside. Auroras are more limited in their distribution around the magnetic poles of a planet. In contrast, the phenomenon of airglow occurs globally and is generally homogeneous [35]. Compared to auroral emissions airglow is the result of chemical interactions between the components of the atmosphere.

In the case of Venus, the production mechanisms of the 1.27 µm nightside and the 4.3 µm dayside emissions are directly related. A strong flux of ultraviolet radiation ($h\nu$) coming from the Sun breaks the CO_2 molecules results in releasing oxygen atoms (O). This mechanism is commonly known as photodissociation and is illustrated in figure 2.5), and can be expressed by:

$$CO_2 + h\nu_{solar} \longrightarrow C + 2O \tag{2.40}$$

If the radiative energy does not overcome the binding energy of the CO_2 molecules, they result to be in an excited state CO_2^*, where the molecules are in a nonlocal thermodynamic equilibrium [12, 13, 43]. Due to the low density at high altitudes between 100 km to 170 km the CO_2^* molecules are not capable to return to their initial state by colliding with each other. Therefore, the emission at 4.3 µm is a result of photoemission of the CO_2^* molecules returning to their initial state CO_2, which also generates adiabatic temperature changes in the Venusian atmosphere and therefore measurable at the particular wavelength of 4.3 µm [13]:

$$CO_2^* \longrightarrow CO_2 + h\nu_{4.3} \tag{2.41}$$

Simultaneously, the free oxygen atoms are being carried by the highly dynamic atmosphere towards the night side of the planet. Here, the atoms from the higher atmosphere migrate to lower altitudes where they recombine to form molecular oxygen

$$O + O + M \longrightarrow O_2 + M + h\nu_{1.27}, \tag{2.42}$$

where M can be a carbon dioxide or oxygen molecule. As a result, they emit light ($h\nu_{1.27}$) at specific wavelengths, with the strongest emission in the infrared spectrum at 1.27 µm (Fig. 2.5) often expressed as $O_2(a^1\Delta_g)$ airglow [6, 35, 24, 14].

A fundamental physical quantity in airglow research is the so-called volume emission rate (VER), which corresponds to the number of photons [ph] emitted per unit volume and unit time:

$$\big[\mathrm{VER}\big] = \frac{\mathrm{ph}}{\mathrm{cm}^3\,\mathrm{s}} \tag{2.43}$$

However, satellite instruments are not able not measure the volume emission rate, but the so-called integrated emission rate (IER), which is the VER integrated over a certain altitude interval [40]). Furthermore, one can use the relation used by [18] to express the IER in the commonly used unit Rayleigh with

$$1\mathrm{R} = 10^{-6}\frac{\mathrm{ph}}{\mathrm{cm}^2\,\mathrm{s}} \tag{2.44}$$

The conversion between the IER in Rayleigh to the photon flux Φ in ph $s^{-1}m^{-2}sr^{-1}$ is given with the following equation from [3]:

$$I = 4\pi 10^{-10}\Phi \tag{2.45}$$

and will later be used to derive the photon flux in order to quantify the performance of the infrared camera. In summary, 1 Mega-Rayleigh (MR) equals 10^{16} photons $s^{-1}m^{-2}$ into 4π sr^{-1}.

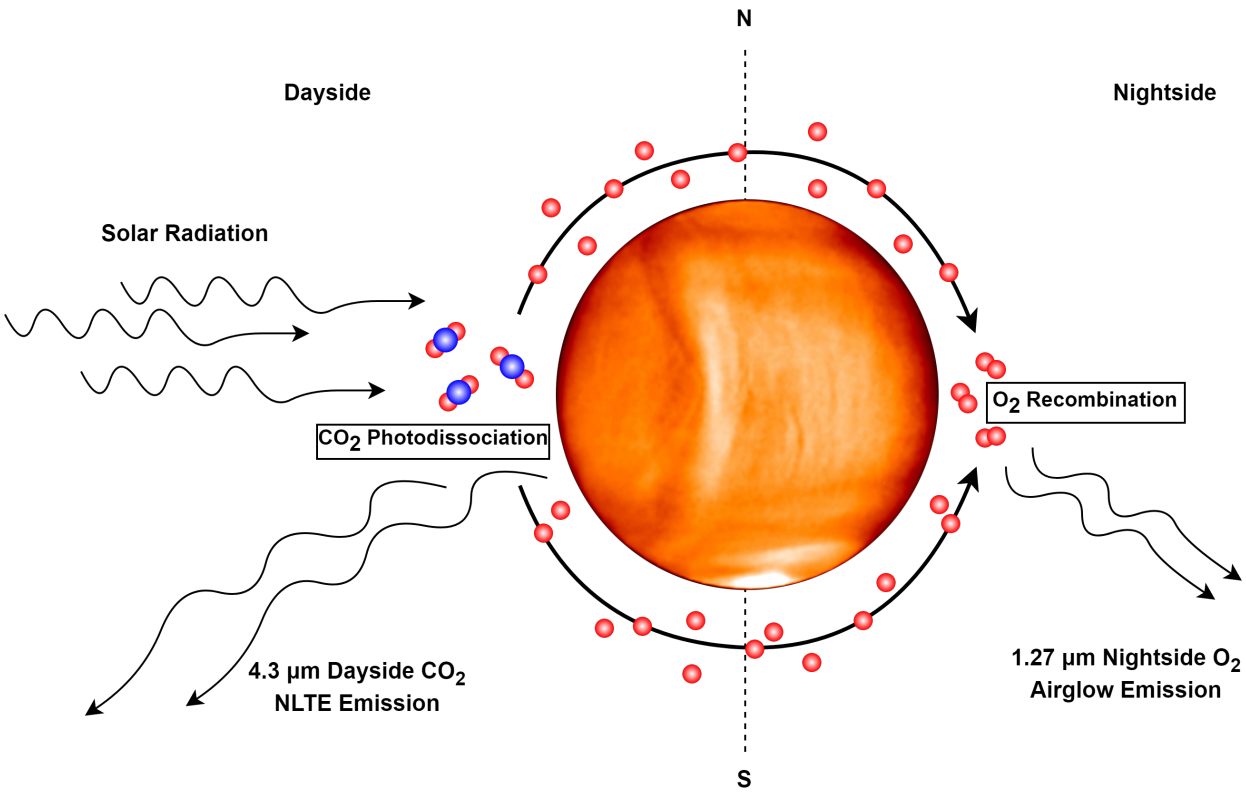

Figure 2.5: Illustration of the production mechanism of the 4.3 µm dayside CO_2 NLTE emission and the 1.27 µm nightside O_2 airglow on Venus

2.8.1 Oxygen Nightside Airglow

Detailed modelling of the O_2 nightside airglow at 1.27 µm has already been conducted by [24, 25, 14]. The O_2 airglow VER peaks at an altitude of 96 km due to the increased density of molecular oxygen at this particular altitude range [25]. Integrating the VER curve over the altitude leads to a total IER as seen from nadir of approximately 0.5 MR [24, 25], which is in strong agreement with a total emission rate of 0.52 MR as observed by Venus Express [35]. However, the airglow emission rate is strongly latitude dependent, peaking at the antisolar point (0° latitude) with a maximum emission of 1.2 MR [35]. Intensities of up to 4.8 MR have also been observed at the antisolar point [24]. Moreover, O_2 nightglow has a radiative lifetime of 4460 s ($\approx$ 74 min) in the Venusian atmosphere [25, 29].

Observations of O_2 nightside airglow on Venus have been conducted over 30 years ago by ground-based telescopes. The corresponding observations made by [6] show a strong peak at exactly 1.269 µm, followed by a lower thermal emission window peaking at 1.277 µm, providing a valuable first impression of the spectral radiance magnitude on the nightside. One can see several spectra of the 1.27 µm airglow measured by the Venus Express Mission [35] with a comparable magnitude at the peak at approximately 1.27 µm with values between 0.02 and 0.12 W $m^{-2}µm^{-1}sr^{-1}$. According to [35], the minor peak observed in the spectra around 1.31 µm represents a thermal emission within an alternate atmospheric window, which is irrelevant in the context of this thesis. As mentioned earlier, the strength of the emission depends strongly on the latitude, which is consistent with the spectra having different emission values at the peak as they were measured at different latitudes. It should also be mentioned that the spectral resolution is much higher in the observations conducted by [6] than in the ones from [35], resulting in a different impression of the radiance distributions, but the emission magnitude is the same.

2.8.2 Carbon Dioxide Dayside Emission

Another possible way to investigate the interior of Venus through its atmosphere lies in the non-local thermodynamic equilibirum (NLTE) emissions on the dayside of Venus [13]. The emissions at 4.3 µm have been intensively measured by the VIRTIS-M and VIRTIS-H instruments onboard the Venus Express mission [34]. Limb observations conducted by VIRTIS-H provided nadir dayside IR spectra around 4.3 µm, which exhibit a characteristic double-peak structure with maxima around 4.28 µm and 4.32 µm [34]. Compared to the O_2 nightside airglow emissions the 4.3 µm NLTE emissions peak at higher altitudes between 100 km to 150 km in Venus' atmosphere, as shown by [13]. The CO_2 dayside NLTE emissions have a stronger emission than O_2 nightside airglow, but it is highly dependent on the emission and solar zenith angle [34].
The emission angle (EA) is defined as the angle between the direction of emission and the perpendicular normal to the surface as in Lambert's cosine law:

$$EA = 90° - \theta, \tag{2.46}$$

where θ stands for the angle between the zenith and observer (Fig. 2.6). As EA increases, there is a corresponding increase in the measured spectral radiance leading to values between 0.02 and 0.20 W $m^{-2}µm^{-1}sr^{-1}$ around the double-peak at 4.3 µm [34].
Simultaneous, the solar zenith angle (SZA), representing the angle between the zenith and the sun (Fig. 2.6), significantly impacts the daytime CO_2 emissions on Venus as it influences the amount of sunlight that the atmosphere receives. Since the SZA varies with the position of the Sun relative to Venus, the measured signal strength on the dayside can change drastically in a range between 0.10 and 0.30 W $m^{-2}µm^{-1}sr^{-1}$ depending on the position of the sun relative to Venus [34] as well as the position and orientation of the spacecraft and instrument onboard.
For the performance analysis of the imaging system, both background signals are assumed to have Gaussian normal distributions, as this allows the characteristic peaks of both background

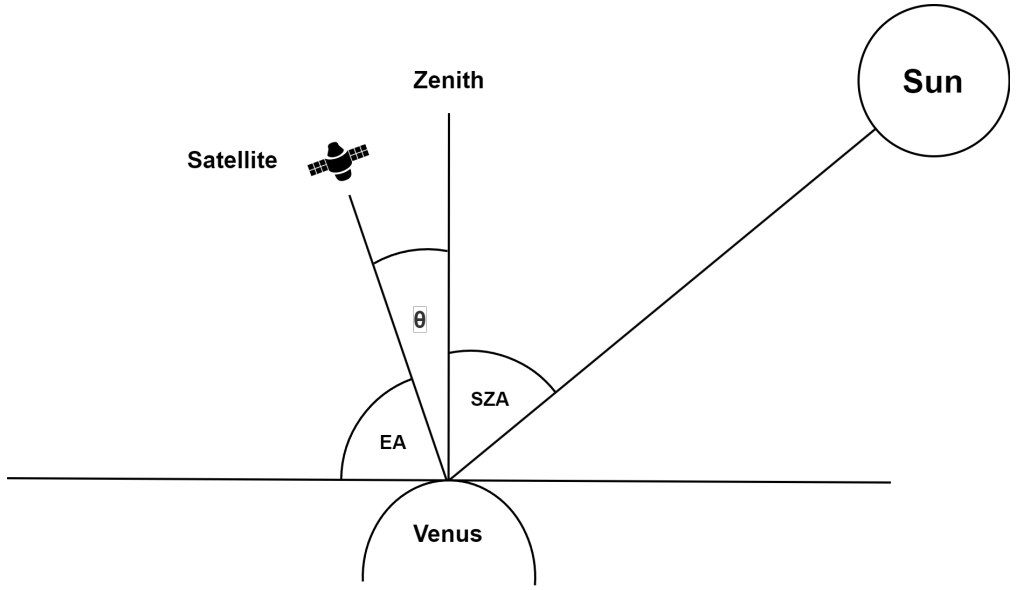

Figure 2.6: Visualization of the emission angle (EA) and solar zenith angle (SZA) in relation to the zenith angle of the satellite θ

signals to be derived as accurate as possible within the scope of this thesis. The spectral radiance distribution will therefore be given by

$$L_\lambda = L_{\lambda_{peak}} \cdot e^{-\left(\frac{\lambda-\lambda_{peak}}{2\sigma}\right)^2} \tag{2.47}$$

where $L_{\lambda_{peak}}$ is the peak radiance value and λ is the wavelength range. Moreover, λ_{peak} is set to 1.27 µm with respect to the O_2 nightside airglow signal and σ is the standard deviation, which is assumed to be 0.005 based on the observed spectra by [35].
The spectral radiance of the day-side signal is assumed to be represented by two Gaussian distributions with peaks at 4.28 µm and 4.32 µm, which overlap each other based on the characteristic double peak mentioned above. Referring to the profiles shown in [34] the standard deviation is set to 0.01, since their distribution is wider. With different values of $L_{\lambda_{peak}}$ the consideration of different spectral radiance profiles as described above can be included for performance and sensitivity analysis of the imaging system.

2.9 Atmospheric-Coupled Rayleigh Surface Waves

This chapter focuses on the physical properties of atmospheric-coupled Rayleigh surface waves in the context of investigating the planetary interior of Venus. Rayleigh surface waves, which are a type of seismic waves generated by seismic body waves during quakes, are fundamental to this approach. The motion of a Rayleigh surface wave is similar to that of a water wave. However, for Rayleigh waves, the vortices rotate retrograde along the surface, as demonstrated by [2].

The key to enable the observation of Venus seismic activity with a remote sensing orbiter in

the Venusian atmosphere is the so-called atmospheric coupling, which occurs when a fraction of the seismic wave energy is transmitted into the atmosphere as it reaches the planet's surface [28]. As shown by [27], a small fraction of the Rayleigh wave energy escapes into the atmosphere beginning at resonant frequencies of 3.10 mHz and 4.15 mHz on Venus [29]. The graph also indicates that Venus is the only planet where possibly weaker seismic activity is counterbalanced by a stronger atmospheric coupling compared to Earth and Mars. This has also been proven by [28, 27], who found that atmospheric oscillations at an altitude of 150 km for the same seismic source have 100 times larger amplitudes on Venus. Computations performed by [12] demonstrated that Venus quakes have amplitudes large enough to be measured by remote sensing instruments.

Rayleigh surface waves propagate with a speed approximately 10 times faster than the speed of sound with $3\,\mathrm{kms}^{-1}$ to $5\,\mathrm{kms}^{-1}$ [28, 29, 33, 22]. In addition, waves from seismic events with detectable emissions are expected to have frequencies of 5 mHz to 200 mHz ([28, 43]), or a period of 200 s to 5 s respectively. The corresponding wavelengths $\lambda_{Rayleigh}$ is given by the fundamental relation

$$\lambda_{Rayleigh} = \frac{c_{Rayleigh}}{f_{Rayleigh}} \tag{2.48}$$

where $f_{Rayleigh}$ and $c_{Rayleigh}$ are the frequency and propagation speed of the seismic waves, respectively. The seismic wavelengths are expected to fall within the range of 15 km to 1000 km, which is an essential parameter in order to investigate the spatial Nyquist frequency [11] given by:

$$X_{Nyquist} = \frac{1}{2\xi_{Rayleigh}} = \frac{\lambda_{Rayleigh}}{2}, \tag{2.49}$$

which constitutes the required ground sampling distance regarding the capability of resolving the corresponding seismic Rayleigh wavelength $\lambda_{Rayleigh}$

$$GSD \overset{!}{\leq} X_{Nyquist} \tag{2.50}$$

and is therefore also essential when considering binning if improving the SNR is required.
Table 2.2 lists all the main characteristics of Rayleigh surface waves relevant for detecting seismic waves in the Venusian atmosphere. Compared to the radiative lifetime of airglow emissions, the period of Rayleigh surface waves is much smaller [43], which is beneficial as the airglow stays relatively constant and therefore does not disappear before the Rayleigh waves can propagate through it. For the 1.27 µm nightside airglow surface wave magnitudes

Table 2.2: Rayleigh Surface Wave Characteristics

Parameter	Range	Unit
$f_{Rayleigh}$	5-200	mHz
$c_{Rayleigh}$	3-5	km/s
$\lambda_{Rayleigh}$	15-1000	km

of at least $M_S = 6$ or higher are required for a successful detection of quakes by remote sensing. On the other hand, the detectable level of seismicity for the 4.3 µm dayside airglow starts

at $M_S = 5$, due to a higher amplification [43]. The rate of occurance has been estimated by[29], who proposed an activity of 25 quakes per year with magnitude larger than 6 and 125 quakes per year with magnitudes larger than 5 while [43] derived a more conservative estimate with 2 and 25 events per year, respectively.

[29] conducted simulations based on the combination of an atmospheric model together with an interior structure model of Venus to generate the variations of the 1.27 µm nightside airglow as a function of epicentre distance. As an example, the Rayleigh surface wave signal corresponding to a Venus quake with $M_S = 6.5$ and a corresponding frequency of 40 mHz. With increasing epicentral distance, the amplitudes of the emission variations decrease from 4000-6000 R at 15° epicentral distance to approximately 800 R, which would be the limit to detect a few quakes per year with a ±800 R detection threshold, acccording to [29]. Based on the increase in emission with decreasing epicentral distance, VER variations of up to ≈10000 R can be assumed for an epicentral distance of 0° in the case that the the source of the quake is detected within the cameras's field of view.
Further estimations of the expected O_2 nightside airglow signal variations have been conducted within the scope of the the mission proposal of VAMOS. The results of the modelled 1.27 µm airglow disturbances by [22] confirm the previously discussed results for a $M_S = 6.5$ quake. For quake magnitudes in the range of 5 to 6 seismic activity is more frequent thus increasing the chance of detection. $M_S = 5.8$ quakes with frequencies in the range of 20 mHz to 25 mHz generate variations of 250 R and 200 R for an epicentral distance of 40° and 60°, respectively [23].
Moreover, [43] presented signal variation amplitudes of 400 R for a $M_S = 6.5$ quake at an epicentral distance of 10° ($f_{Rayleigh} = 20$ mHz), which is much weaker compared to the signal amplitudes of [29]. For a frequency of 100 mHz this decreases to 20 R due to the airglow attenuation of 20 dB per decade [43]. Consequently, the signal amplitudes will decrease to only 10 R for 200 mHz, as waves from seismic events are expected at frequencies of up to 200 mHz.

Based on the results discussed previously, airglow variation amplitudes from 10 to 10000 R will be considered over a bandwidth of 5 mHz to 200 mHz for the 1.27 µm O_2 nightside airglow in the following. For the 4.3 µm CO_2-NLTE dayside emissions stronger airglow variation amplitudes can be assumed as the seismic waves get amplified for altitudes up to 135 km by a factor of 128 [43]. In the scope of this thesis, the aim is to find out which of the two signals is more suitable to detect atmospheric-coupled Rayleigh surface waves and to optimise the instrument accordingly.

3 Mission Definition

Based on the theoretical foundations and the aspects discussed above, the design of the imaging system is a complex task. Therefore, the design process will follow a structured approach outlined by [49], utilising their comprehensive approach. As a framework for the design process, a mission design flowchart (see fig. 3.1) is used, which is explained in more detail in the subsequent chapters of the thesis, and can be divided into three distinct sections: mission definition, characterisation and analysis, and evaluation and selection.

The first step in the mission design process is the mission definition, which involves the explicit definition of the mission objectives as the cornerstone of the mission. Additionally, a set of related mission requirements and constraints provide a quantifiable reflection of the mission objectives, ensuring that they are not only understandable but also precisely measurable. Within the context of the defined mission objectives, requirements and constraints, the figures of merit will be formulated. They are a crucial element in evaluating the system's performance and identifying whether the mission concept is capable of achieving the mission objectives. Furthermore, they establish a link between the three primary sections of the mission design flow chart, allowing for a quantitative criterion to evaluate the different possible mission concepts.

Subsequently, this framework allows the identification of three distinct mission concepts, each with its own set of trade-offs and considerations. As previously mentioned in chapter 2.8, viable options for detecting atmospheric-coupled Rayleigh waves in the Venusian atmosphere are either on the Venusian nightside or on the dayside. However, it is essential to define each concept as it directly impacts the design choices for the imaging system. In the second stage of mission design, trade-off studies analyze these concepts, with a particular focus on the system drivers that affect the mission's success. This analytical process enables a critical evaluation of the strengths and weaknesses of each concept.

Finally, the results of these analyses are compared and evaluated in relation to the figures of merit. Consequently, this leads to the selection for the preliminary design of the imaging system, ensuring that it is optimally aligned with the mission objectives while meeting the defined requirements and constraints.

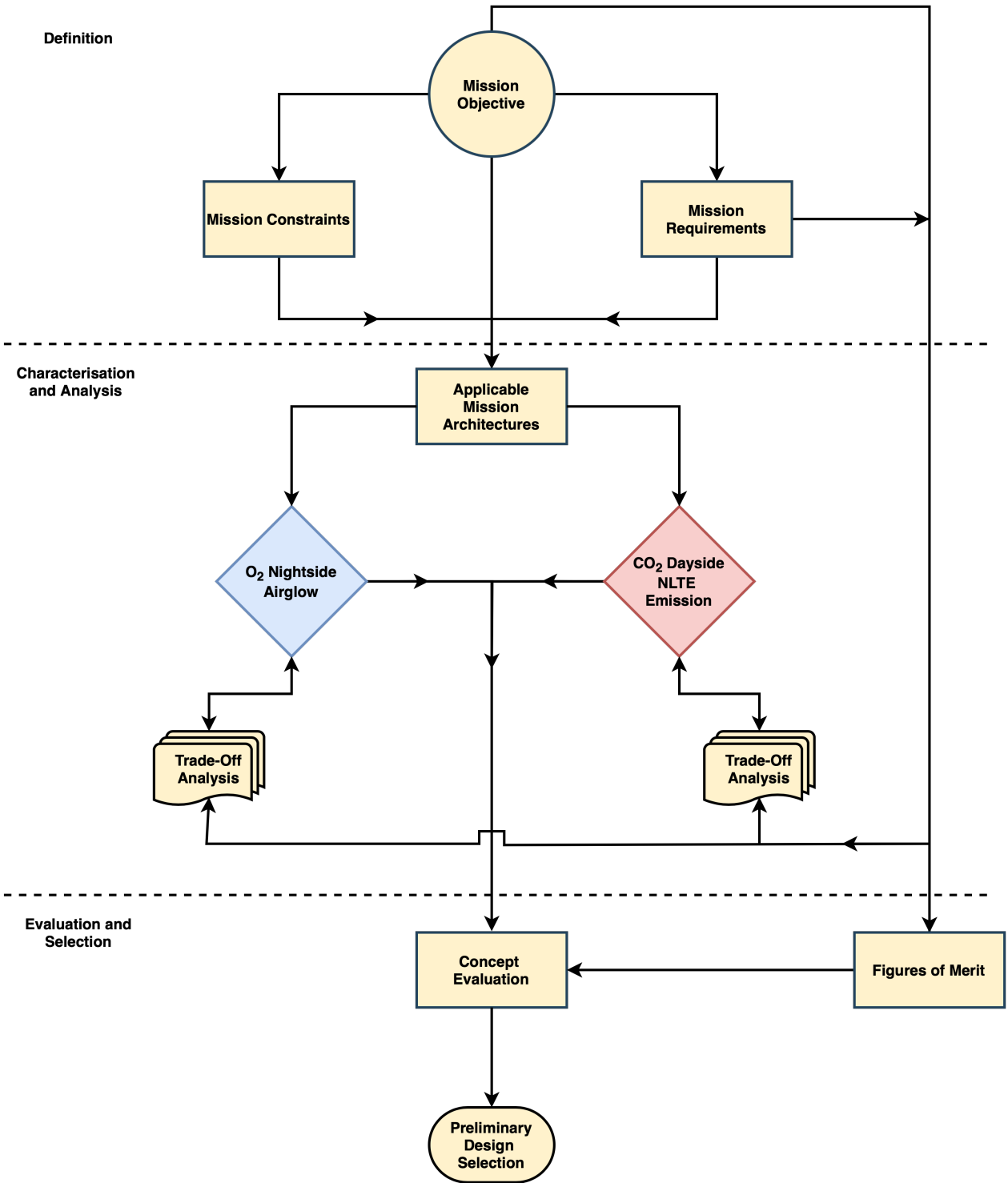

Figure 3.1: Flow chart of the mission design process in order to select a preliminary design of the imaging system

3.1 Mission Objectives

The first step in the mission characterisation process is to define the mission objectives. These objectives guide the entire mission planning and payload design process and serve as the basis for determining the mission requirements, constraints and figures of merit. As mentioned above, the primary objective of the mission is to detect seismic activity on Venus by remote sensing from space. From the primary objective, a number of secondary objectives can be derived, which are useful in determining the requirements, constraints and figures of merit for the imaging system. Based on the work of [43, 29], it is already clear that the primary objective can be achieved by measuring atmospheric-coupled Rayleigh waves, observing specific wavelengths corresponding to a characteristic background radiation from the Venusian atmosphere. Therefore, the secondary mission objectives are directly derived from the primary objective and summarised in the table 3.1.

Table 3.1: Mission objectives

Primary objective: To detect seismic activity in the Venusian atmosphere with remote sensing from space to investigate the interior structure of Venus.
Secondary objectives: To demonstrate the detection of atmospheric-coupled Rayleigh waves. To observe and monitor the propagation of atmospheric-coupled Rayleigh waves. To study the background radiation emissions of Venus within the chosen electromagnetic range.

3.2 Mission Requirements

Starting from the mission characterisation concept, the mission requirements are defined in the following. Here we will focus on the imaging system, as this is the ultimate goal in the scope of this thesis and yet the critical element to fulfil the previously defined mission objectives. Therefore, the mission requirements reflect the mission objectives, which will define how well the imaging system should perform and operate in order to achieve the mission objectives in a quantitative way. Mission requirements are summarised in table 3.2 and will be discussed in the following.

The first requirement (MR01) on orbital lifetime does not directly influence the imaging system design process, but it is critical to achieve the primary objective. It serves as a general mission requirement that indirectly influences the performance of the imaging system as

a payload. The orbital lifetime requirement is of fundamental importance based on the findings in section 2.9, which indicate a relatively low frequency of detectable seismic quakes on Venus. In addition, the choice of specific mission concepts may impose additional constraints on the available measurement time, further reducing the probability of successful detection. For example, if the imaging system is only capable of detecting on one side of Venus (based on trade-off studies and mission concept evaluations), this will reduce the time available for scientific observations. It is therefore essential that the spacecraft, including the imaging system, remains operational for at least one year in orbit around Venus in order to meet the primary objective.

Table 3.2: Mission requirements of the imaging system

MR01: **Orbital Lifetime**	The mission including the imaging system should remain operational for a minimum of one year to increase the probability of detecting seismic activity.
MR02: **Field-of-View**	The imaging system should provide full-disk imaging of Venus to maximize the probability of detecting seismic activity.
MR03: **Pointing**	The imaging system should be oriented in a nadir-looking configuration enhancing probability of detecting seismic activity.
MR04: **Spatial Resolution**	The imaging system should achieve spatial resolution sufficient to resolve atmospheric-coupled Rayleigh waves in the Venusian atmosphere according to their wavelengths, enabling their observation and measurement.
MR05: **Spectral Range**	The imaging system should cover the specific wavelength range within the chosen electromagnetic spectrum enabling the observation of atmospheric-coupled Rayleigh waves.
MR06: **Sensitivity**	The imaging system should possess the sensitivity to detect and measure seismic activity in the form of atmospheric-coupled Rayleigh waves in the Venusian atmosphere.

The second requirement (MR02) relates directly to the design of the infrared camera system to maximise the probability of detecting seismic activity. The system should therefore have a field of view (FOV) that allows full disk imaging of Venus, enabling continuous monitoring of the entire surface of the planet. Seismic events can occur at different locations on Venus and limiting the field of view could result in missed opportunities to observe.

Another important requirement for extending the imaging system's ability to detect seismic activity in the Venusian atmosphere is the pointing of the camera (MR03). As previously investigated by [43], the camera should be pointed in a nadir-looking configuration. This increases the probability of detecting seismic activity as the nadir orientation minimises the path length of the observations through the Venusian atmosphere. Moreover, it reduces the

amount of atmospheric interference, which may reduce the amount of electromagnetic radiation detected and therefore the signal-to-noise ratio (SNR). In addition, nadir pointing minimises geometric distortion in the captured images. Distortion can lead to unintended measurement inaccuracies and positional errors when observing seismic waves propagating through the Venusian atmosphere.

The spatial resolution requirement (MR04) is central to the successful detection and observation of atmospheric-coupled Rayleigh waves in the Venusian atmosphere. By specifying the need for a spatial resolution that matches the wavelengths of these waves, the requirement ensures that the imaging system can accurately resolve the phenomena on the ground.

With the examined wavelenghts for quake detection described in section 2.8, the spectral range requirement (MR05) is necessary as it ensures that the imaging system is actually capable of effectively observing atmospheric-coupled Rayleigh waves. By specifying a range of wavelengths within the chosen electromagnetic spectrum, this requirement ensures that the camera system can capture the spectral signatures associated with these waves. This range must be well chosen in order to maximise signal-to-noise and thus optimise quake detection and measurement. Essentially, this requirement aligns the imaging system with the precise spectral characteristics of the phenomena being observed, enhancing its ability to contribute valuable data to the mission's scientific objectives. It also enables the system to filter out irrelevant wavelengths, reducing background noise and improving the accuracy of the observations.

Finally, the signal-to-noise requirement (MR06) is the cornerstone of the imaging system's ability to detect and measure seismic activity in the form of atmospheric-coupled Rayleigh waves in the Venusian atmosphere. It is fundamental in ensuring that the system can distinguish the signals of atmospheric-coupled Rayleigh waves from the high background emissions. By having the necessary signal-to-noise ratio, the imaging system can accurately detect and quantify these waves, which is critical to achieving the primary mission objective.

3.3 Mission Constraints

To determine the functional and operational performance to meet the mission objectives, mission constraints play a pivotal role in mission design, defining the boundaries and limitations to the system design. The key distinction between mission requirements and constraints lies in their impact on mission objectives: requirements guide what must be achieved to fulfill objectives, while constraints define the practical boundaries that must be respected to meet those objectives.

With its official inclusion in ESA's planned missions, the EnVision mission [16] has the potential to be used as a rideshare to Venus when launched in 2032, thereby keeping the complexity and cost of this mission low. This implies constraints not only on the mission, but also on the imaging system to be examined here. Consequently, it must be considered that the size, mass and volume must be accommodated within the EnVision spacecraft. Within

the scope of this thesis, only the selected focal length and the aperture diameter of the optical system provides an indication of size. Interplanetary ride-sharing has been successfully demonstrated for the first time by using the Insight mission to carry two CubeSats for the interplanetary mission to Mars [41]. Both satellites had a size of 6U (1U = $10 \times 10 \times 10$ cm) accommodating the typical subsystems and a camera as a payload. As this is still an early developement of the CubeSat going to Venus, the size of the payload shall be designed as small as possible in order to enable other subsystems to have a larger sizing margin, which will be defined in a later stage of the mission design process but not within the scope of this thesis. Consequently, the size of the payload shall be constrained to fit into 1U.

Another constraint is the final orbit. Currently the EnVision science orbit is planned to be a low Venus orbit with an altitude between 220 km to 527 km highly inclined with $i \approx 88°$. Prior to that, there are currently two possible options for Venus orbit insertion as shown in [16]: entering Venus via either the north or south pole, determining the location of the pericentre from which the aerobraking manoeuvre will begin. This implies that the pericentre will always be low and would result in high fuel demand to raise the orbit again in order to achieve the mission objectives. The time of deployment of the CubeSat is therefore critical to the following trade-offs with respect to the orbit altitude. If the requirements are not compatible with a low orbit altitude, the spacecraft should be ejected at a high orbit altitude immediately after the Venus insertion orbit, in order to use fuel-efficient manoeuvres to reach the target orbit suitable for this mission. The inclination is not critical, as the requirements aim for full-disk imaging. However, if it is determined later in the mission design process that a particular inclination is required, an early separation with a high orbital altitude would also be advantageous for fuel-saving orbital manoeuvres. Table 3.3 gives an overview over the potential mission constraints in the case of using EnVision as a rideshare for a CubeSat to Venus.

Table 3.3: Mission constraints

MC01: **Accommodation**	To accommodate the imaging system on board a small satellite using the EnVision spacecraft as a rideshare, it shall not exceed the size of 1U.	$f \leq 10$ cm $D \leq 10$ cm
MC02: **Orbit Insertion**	By using EnVision as a rideshare, the initial orbit insertion for the mission is constrained, with specific considerations for the orbit altitude.	$220 \leq h \leq 250000$ km

3.4 Figures of Merit

The figures of merit (FoM) are another key factor in the mission definition process as they quantify the performance of the imaging system directly related to the satisfaction of the mission objectives. FoMs bridge the gap between mission definition and evaluation, providing

a way to evaluate and prioritise design choices based on trade-off analysis. Moreover, FoMs are a critical component as they are highly useful in making informed decisions during the design phase to ensure that mission objectives and requirements are met. Therefore, FoMs must be both quantifiable and sensitive to system design and are formulated in table 3.4.

Table 3.4: Summarised figures of merit (FoM) with the corresponding quantifiable criterion

FoM01: **Spatial Resolution**	To observe atmospheric-coupled Rayleigh waves in the Venusian atmosphere the MTF must be higher than the defined threshold.	$MTF \overset{!}{\geq} 0.2$
FoM02: **Detectivity**	To detect atmospheric-coupled Rayleigh waves in the Venusian atmosphere against the high background noise the SNR must be higher than the defined threshold.	$SNR \overset{!}{\geq} 3$

In order to achieve the mission objectives of resolving the atmospheric-coupled Rayleigh waves in the atmosphere of Venus (MR04) at sufficient SNR (MR06), the imaging system must have adequate resolution. One of the most intuitive figures of merit for resolution performance can be found in the Ground Sampling Distance (GSD), defined in section 2.4 with eq. 2.29. Design choices such as orbital altitude and detector selection (pixel pitch) are highly sensitive to the GSD. However, the GSD is not sufficient to determine whether the spatial resolution is high enough to resolve the seismic waves in the Venusian atmosphere. The Nyquist theorem (Eq. 2.49 and 2.50) also needs to be taken into account. This is particularly important when considering pixel binning which directly affects the spatial resolution (Eq. 2.33). Furthermore, the contrast needs to be sufficient in order to resolve the spatial frequencies of the Rayleigh waves $\xi_{Rayleigh}$. As proposed by [5], the desired optical performance of an imaging system can be sufficient with a minimum of 10% contrast. However, this is a rather general quantification and in order to be sure the threshold in this thesis will be set to MTF = 0.2 (FoM01). Optical design choices and the choice of infrared detector, as well as orbital altitude, strongly influence this figure of merit.
In addition, pixel smear needs to be taken into account as it quantifies the extent to which a single pixel in the camera's sensor array is displaced during image capture due to spatial motion and integration time (eq. 2.31). It directly affects the camera's ability to observe seismic Rayleigh waves in the Venusian atmosphere, thus contributing to the mission's objectives. Therefore, it is desirable to have a pixel smear of not more than 20%, which is highly sensitive to the design choices of integration time and orbital altitude, and is also directly related to FoM01. It is part of the MTF and for a smear of less than 20% its contribution is minimised.

Finally, the desired signal-to-noise Ratio as a figure of merit (FoM02) needs to be defined. The SNR is directly related to the mission objectives, as it directly reflects the ability of the camera system to distinguish and capture the desired signal from the atmospheric-coupled Rayleigh waves against the high background noise. Note, that it is extremely sensitive to the selection of the infrared detector due to the characteristic noise contributions. The determination of the minimum required SNR of 3 given by [53], which is considered minimally

acceptable, ensuring a probability of the peak not being random noise at approximately 99.7% (3σ).

3.5 Mission Concepts

An essential step towards the preliminary design of a desired (payload) system within a spacecraft is the definition of different mission concepts. These concepts represent distinct approaches for the imaging system design to the challenge of observing seismic activity within the atmosphere of Venus. Furthermore, they play a crucial role in narrowing down the design possibilities. They restrict certain aspects of the system, such as sensor selection and other general considerations, in line with the defined mission requirements and constraints. These concepts will undergo further analysis, examined against the mission requirements and constraints, and evaluated using figures of merit. Through this systematic process, we will determine the most appropriate design in its preliminary state, ensuring that it is optimally aligned with the overarching mission objectives.
For this mission, there are two initial approaches: detection of atmospheric-coupled Rayleigh waves by observing O_2 nightside airglow or by observing CO_2 dayside non-local thermodynamic equilibrium (NLTE) emissions. The design decisions will therefore be based on these two mission concepts.

3.5.1 Full Disk Imaging

Chapter 2 has shown that the design of an imaging system for a remote sensing spacecraft is very complex, as many parameters are interconnected and influence each other. To provide a starting point for the design process, an elementary relationship can be derived from the MR02 mission requirement for full disk imaging. In the case of Venus, full disk imaging implies that the field of view must be as wide as the diameter of Venus with $2R_V = 12102$ km. The necessary link between the object and the image space is given by the following equation

$$2R_V \stackrel{!}{=} n_{pixel} \cdot GSD, \tag{3.1}$$

where the diameter of Venus is translated into the number of pixels of the sensor times the corresponding ground sampling distance. With the equations 2.28 and 2.29 it is possible to derive a function that relates the focal length to the orbital altitude in order to achieve full disk imaging:

$$2R_V = n_{pixel} \cdot iFOV \cdot h \tag{3.2}$$

$$2R_V = n_{pixel} \cdot 2 \arctan\left(\frac{p_{pitch}}{2f}\right) \cdot h \tag{3.3}$$

$$\Rightarrow f = \frac{p_{pitch}}{2 \cdot \tan\left(\frac{R_V}{n_{pixel} \cdot h}\right)} \tag{3.4}$$

Note that this derivation includes the choice of infrared sensor with number of pixels n_{pixel} and pixel pitch p_{pitch}. When looking back at eq. 3.1, one can see that this implies also the

fixation of the ground sampling distance

$$GSD = \frac{2R_V}{n_{pixel}} \tag{3.5}$$

leading to the GSD being constant and depending on the number of pixels based on the selected detector.
Figure 3.2 shows the basic geometry for the mission concepts described below. Also note that the figure is not to scale, as it is used for illustration purposes only.

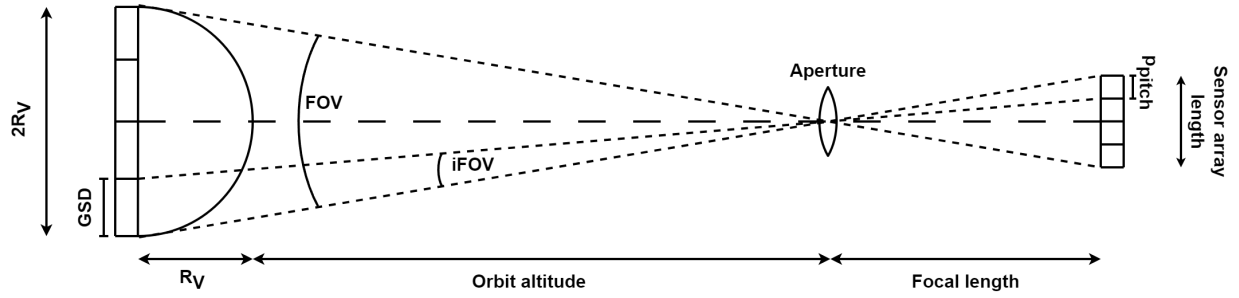

Figure 3.2: Full disk imaging geometry with Venus on the left and the detector on the right

3.5.2 Study Cases of the Expected Signals

Based on the assumed Gaussian normal distributions for the background signals, as described in section 2.8, three cases are defined for the emission strength of each background signal. Based on the radiance profiles measured by the Venus Express mission [35], a nominal case signal of the O_2 nightside airglow background is chosen to have a peak radiance $L_{\lambda_{peak}}$ of $0.07\,\mathrm{Wm^{-2}\mu m^{-1}sr^{-1}}$. In addition, a worst and best case peak radiance value $L_{\lambda_{peak}}$ at 0.02 and $0.12\,\mathrm{Wm^{-2}\mu m^{-1}sr^{-1}}$ are presumed, respectively. For the CO_2 NLTE dayside emissions the nominal, worst, and best case signals are chosen to be 0.15, 0.02 and $0.30\,\mathrm{Wm^{-2}\mu m^{-1}sr^{-1}}$ respectively. The choice of each emission strength per background is based on the distribution of measured signals discussed in section 2.8. By considering only three background signal strengths, the performance of the imaging system can be efficiently analysed over the full range of possible background emissions for the observations on the day- and nightside. Furthermore, this worst-to-best case approach allows the limitation of the design choices discussed later to be determined without neglecting any possible background signal. Finally, for each system driver trade-off, the nominal signal case shall be considered as the baseline background signal. Later, the best and worst case signals will be analysed for the limits of suitable system designs to further reduce the options. Besides the background signal, the seismic Rayleigh wave signal is determined using the same approach. It should be noted that a wave velocity of $4\,\mathrm{kms^{-1}}$ is chosen for all assumed seismic signals as an average of the values given in chapter 2.9. This simplifies the complexity of the analysis discussed in the following, and is not particularly relevant in this work in terms of figures of merit compared to, for example, the emission strength.

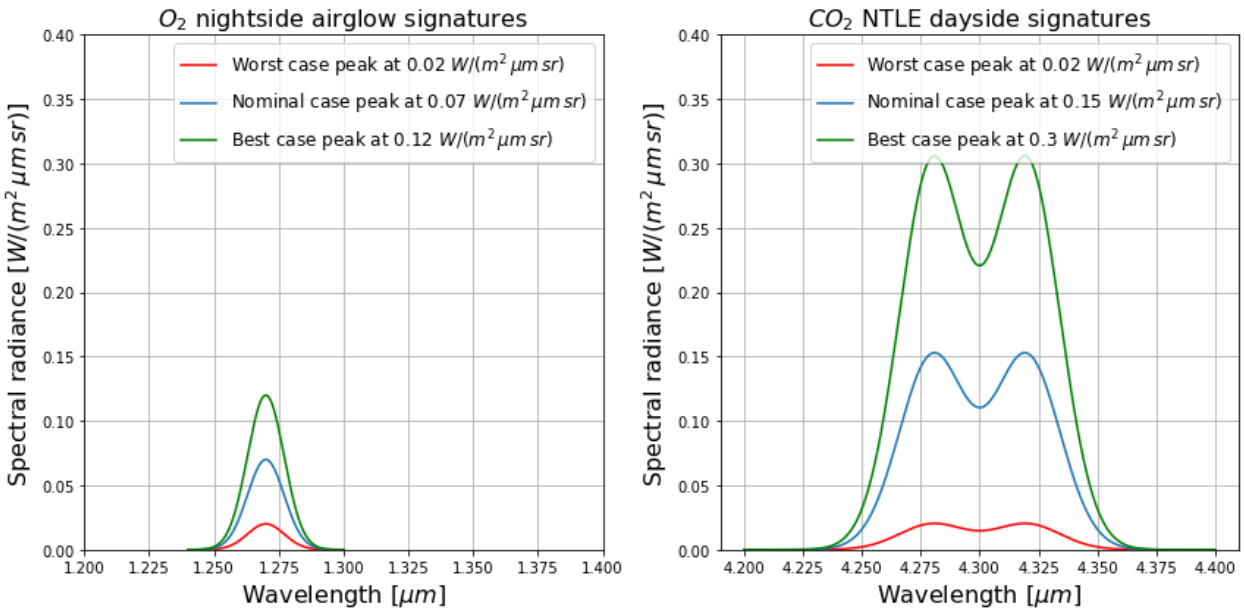

Figure 3.3: Spectral radiance background as a function of wavelength as derived based on Gaussian distributions of the nightside airglow (left) and dayside NLTE emission (right)

Based on the characteristics described in chapter 2.9, in particular the work of [43, 29], the nominal case signal is defined corresponding to a quake magnitude of $M_S = 6.5$. This corresponds to a frequency of 20 mHz and a wavelength of 200 km. In addition, the worst case signal shall have a surface magnitude of $M_S = 5.5$ with a corresponding frequency of 100 mHz and wavelength of 40 km as defined in [43]. In contrast, the best case signal is derived from the signals discussed by [27, 29] assuming a surface magnitude of $M_S = 7.5$ with a corresponding frequency of 5 mHz and wavelength of 800 km. The selection of these three signals agrees very well with the possible values of properties of the seismic waves presented in chapter 2.9. Since environmental characteristics are not considered as system drivers [49], they had to be determined at this point in the definition of the mission concepts in order to quantify initial values for the defined system drivers below. Table 3.5 summarise all properties of the assumed cases for the background and seismic signals. Note, that it was necessary to use the defined parameters from table 3.6 in order to derive the background intensities $I_{background}$ from the corresponding radiances $L_{\lambda_{peak}}$.

3.6 System Drivers

Before conducting trade-off studies for detailed analysis of the imaging system design, it is essential to identify the system drivers that form the basis of each trade-off. This approach will further reduce the number of possible designs without eliminating options that may be important to consider when deriving a preliminary design. System drivers are considered to be characteristics that largely determine system performance [49]. Based on the interrelated parameters described in chapter 2, together with the previously identified mission objectives and requirements, six system drivers (listed below) are identified as having the greatest

Table 3.5: Definition of the properties for the assumed cases of the background and seismic signals

Parameter	**1.27µm O_2 Airglow**			**4.3µm CO_2 NLTE Emission**			Unit
	Worst	Nominal	Best	Worst	Nominal	Best	
M_S	5.5	6.5	7.5	5.5	6.5	7.5	-
$\lambda_{Rayleigh}$	40	200	800	40	200	800	km
$f_{Rayleigh}$	100	20	5	100	20	5	mHz
$I_{Rayleigh}$	20	400	10000	720	14400	360000	R
$L_{\lambda_{peak}}$	0.12	0.07	0.02	0.30	0.15	0.02	$\frac{W}{m^2\,\mu m\,sr}$
$I_{background}$	5.7	3.3	0.9	289.3	144.6	19.3	MR

impact on imaging system performance in this case:

1. Detector
2. Bandpass of optical filter
3. Integration time
4. Image processing: binning and stacking
5. f-number
6. Orbit altitude

The selection of a suitable detector has a major impact on the performance of the payload system as it affects the radiometric, remote sensing and optical performance. Moreover, the bandwidth and transmission of the optical filter is highly critical to achieve the mission objectives, in particular affecting the incoming signal on the detector. As already explained, the orbit altitude is a cornerstone for the design of the imaging system, with the determination of the focal length (eq. 3.4) strongly influencing the remote sensing and optical performance. Furthermore, the integration time, binning and stacking have to be investigated in order to achieve the desired signal-to-noise ratio.

Table 3.6: Initial baseline concepts for the day- and nightside scenario

	O_2 Nightside Airglow	**CO_2 Dayside NLTE Emission**
Detector	Teledyne H2RG SWIR	Teledyne H2RG MWIR
Orbit	Circular: 45 000 km	Circular: 45 000 km
f#	4	4
Integration time	1s	1s
Bandwidth / Transmission	20 nm / 90%	100 nm / 70%
Binning	-	-
Stacking	-	-

For the baseline concept of each scenario the orbit altitude and f-number will be set as

proposed by [43] since the mission objectives are the same. Furthermore, the integration time will be set to an initial value of 1 s as a starting point. No binning or stacking will be considered for the baseline concepts in order to analyse the performance of the imaging system without image processing methods. The baseline detector for both cases will be the Teledyne H2RG detector as suggested by [43] and will be discussed in detail within the trade studies in chapter 4. In addition, the optical filter will have a transmission of 90% for observing at 1.27 µm and 70% at 4.3 µm based on the current state-of-the-art optical filters [9, 8, 48, 47]. The bandwidth of 20 nm for the nightside and 100 nm for the dayside based on the assumed background signals (see figure 2.47). Finally, the two baseline scenarios are shown in table 3.6, which emphasises that the only initial difference lies in the different detectors and optical filters corresponding to the different background signals. Note that these baseline concepts are only a starting point for the iterative trade process and will therefore change until becoming the preliminary system design at the end of this thesis.

4 Trade-off Analysis and Evaluation

The goal within this chapter is to analyse the viability of the defined mission concepts regarding their performance and their ability to meet the mission objectives. The approach of a trade-off analysis is a good choice for deriving a payload system design especially for a mission with such a unique scientific objective. Conducting a trade-off analysis is important, since the system drivers cause multiple effects on various system design choices. This means that the change of one specific parameter might improve certain characteristics of the imaging system, while degrading others. Therefore the goal is to achieve a solution which provides the best mix of results regarding the system performance and meeting the mission objectives. The previously defined system drivers will now constitute as a cornerstone of each trade in order to reduce the number of trade-off combinations without eliminating options that may be suitable later. As the system drivers have multiple effects on the system design each parameter, which is affected by the respective system driver, is going to be identified based on the relations given in the theoretical background.

4.1 Detectors

The detector is perhaps the system driver with the most impact on the performance of the imaging system. The selection of a suitable detector is primary driven by the spectral range it covers in order to be effective when measuring electromagnetic radiation at the target wavelengths. As already described in section 2.3, the detector is mainly characterised by the number of pixels with a specific pixel pitch and full well capacity and furthermore by its quantum efficiency, readout noise and dark current. These characteristics ultimately affect the figures of merit of the infrared camera making a trade between different detectors a crucial part of this analysis.

4.1.1 Short Wavelength Infrared Detectors

Regarding the observation of the nightside of Venus, three possible SWIR sensors have been identified based on the possible application in the particular infrared spectrum. In accordance with the recommendation by [43], the initial focus of this thesis is the examination of the H2RG detector, developed by Teledyne. Firstly, the H2RG detector utilizes HgCdTe as its semiconductor material, which has also been employed on the James Webb Space Telescope (JWST), which constitutes space flight heritage to the highest level. The H2RG detector demonstrates high quantum efficiency in the spectral range of 1 µm to 3 µm, exceeding 80% at a wavelength of 1.27 µm [45, 52], which requires cryogenic cooling at an operational tem-

perature of 80 K [43]. Additionally, the H2RG detector offers two resolution options, affecting dark and readout noise.
The two other selected infrared detectors originate from the discussed detectors for the Venus Emissivity Mapper (VEM) for the NASA Veritas mission [17]. The Xenics XSW640 is made of InGaAs with a cut-off wavelength at 1.7 µm and is therefore highly applicable for SWIR observations. The operating temperature lies between 213 K to 233 K, therefore cooling requirements are much lower compared to the H2RG/H4RG. Furthermore, it has two different gain modes, where high gain reduces the readout noise but also the full well capacity and vice-versa. The Cardinal 1280 detector by Semi Conductor Devices (SCD) is also an InGaAs detector operating between 213 K to 202 K with three different gain modes [17]. The spectral response lies between 0.4 µm to 1.7 µm with quantum efficiency of over 80%. All relevant characteristics of the chosen detectors for the observation of the Venus nightside are listed in table 4.1. Before looking at the imaging systems performance, the choice of the detector al-

Table 4.1: Overview of the material, spectral range λ, operational temperature T, pixel size p_{pitch}, number of pixels n_{pixel}, quantum efficiency η, dark current I_{dark}, readout noise n_{noise} and full well capacity FW of the selected SWIR detectors: Teledyne H2RG/H4RG, Xenics XSW 640 LG/HG and SCD Cardinal 1280 LG/MG/HG for the O_2 nightside airglow observation of Venus

Parameter	**Teledyne**		**Xenics XSW640**		**SCD Cardinal 1280**			Unit
	H2RG	H4RG	LG	HG	LG	MG	HG	
Material	HgCdTe		InGaAs		InGaAs			-
λ	1.0 - 3.0		0.9 - 1.7		0.6 - 1.7			µm
T	80		213 - 233		213 - 202			K
p_{pitch}	18	15	20		10			µm
n_{pixel}	2048×2048	4096×4096	640×512		1280×1024			-
η	>80		>75		>80			%
I_{dark}	8e-21	8.8e-22	48e-15		1e-15			A
n_{noise}	100	18	500	95	350	170	40	e^-
FW	80		800	63	1000	500	10	ke^-

ready affects some characteristics of the infrared camera (Table 4.2). As already mentioned, the focal length f is ultimately determined by the specifics of the detector (see eq. 3.1). Consequently, the lowest pixel size together with the highest resolution (n_{pixel}) results in the largest focal length of 228.5 mm with the Teledyne H4RG among the SWIR detectors. Despite the different detector specifications, the focal length when using the Xenics and Cardinal detectors is the same, demonstrating that pixel pitch and detector resolution have the same impact on the focal length. As shown in table 4.1, the pixel size of the Cardinal detectors is half that of the Xenics detectors, which is compensated by the doubled resolution of the Cardinal. Together with the fixed f-number the aperture diameter D can be determined with equation 2.8 showing that a longer focal length results in a longer aperture diameter. Furthermore, with the determination of the focal length, it is now possible to determine the FOV and iFOV (see eq. 2.27 and 2.28 respectively). As the Teledyne detectors have the same number of pixels horizontally and vertically, this results in a square FOV, while the

Xenics and Cardinal detectors have a larger number of pixels horizontally, which leads to a rectangular FOV.

When looking at the GSD for each detector, it is very clear that a larger number of pixels directly result in a lower GSD and thus better spatial resolution. Therefore, the Teledyne H4RG has the best spatial resolution and the greatest potential to improve signal-to-noise performance with binning, if later necessary, taking into account the Nyquist criterion. On the other hand, the Xenics detectors have the least potential, with a GSD that is eight times worse compared to Teledyne H4RG. Lastly, the pixel smear performance is sufficient for all detectors, whereas the Teledyne H4RG has a slightly higher pixel smear due to the lowest GSD (see eq. 2.31) while the ground velocity and integration time are fixed when using the considered detectors for the imaging system. The selected detector has a very high impact on

Table 4.2: Determined focal length f, aperture diameter D, (instantaneous) field-of-view $(i)FOV$, ground sampling distance GSD and pixel smear PS of the imaging system based on the selected SWIR detector for observing Venus' nightside

Parameter	**Teledyne**		**Xenics XSW640**		**SCD Cardinal 1280**			Unit
	H2RG	H4RG	LG	HG	LG	MG	HG	
f	137.075	228.46	38.076		38.076			mm
D	34.27	57.11	9.51		9.51			mm
FOV	15.31×15.31		19.08×15.31		19.08×15.31			deg
$iFOV$	0.1313	0.0656	0.525		0.2626			mrad
GSD	5.909	2.955	23.637		11.818			$\frac{\text{km}}{\text{pixel}}$
PS	1.57	3.139	0.39		0.78			%

the detectors SNR performance as several parameters determined by the detector specifications affect the SNR (see eq. 2.22). Figure 4.1 shows the SNR performance for the previously described detectors for each case (worst, nominal, best) in the current baseline design of the imaging system, which gives the performance range for each detector, demonstrating a big gap between the achieved and required SNR in order to detect seismic Rayleigh waves in the Venusian atmosphere on the nightside.

Nevertheless, both Teledyne detectors show the best SNR performance with the current baseline design, especially for the best-case-scenario as their dark current and therefore dark noise as well as their readout noise is lower showing the significant impact of the noise contributions, especially dark noise, on the SNR performance. On the other hand, worst-case SNR values are significantly lower for every considered detector with values between $1.4 \cdot 10^{-4}$ (Cardinal 1280 LG) up to $7 \cdot 10^{-4}$ (Teledyne H2RG/H4RG) and also the nominal-case values are still very low between $3 \cdot 10^{-3}$ (Cardinal 1280 LG) up to $1.7 \cdot 10^{-2}$ (Teledyne H4RG).

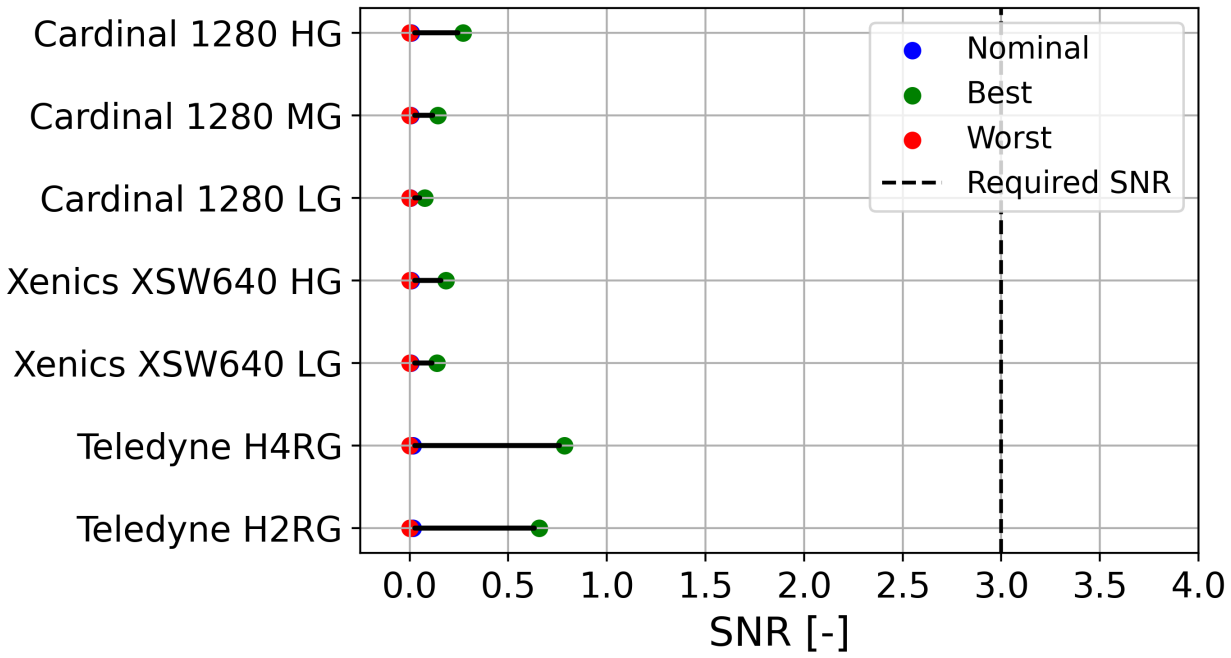

Figure 4.1: SNR performance of the considered SWIR detectors for best, nominal and worst case in the current baseline design when observing the O_2 nightside airglow

The optical performance of the imaging system is investigated using the same approach for the detectors for each case, giving the optical performance range in terms of the MTF at the spatial frequency corresponding to the wavelength of the considered seismic quake in each case, as shown in figure 4.2.

The Teledyne detectors show the best performance compared to the others with MTF values above 0.88 and 0.95 for the H2RG and H4RG respectively, which exceeds the MTF threshold by far. The slightly better performance of the H4RG lies in the higher spatial resolution capabilities due to a higher GSD compared to the H2RG.

Due to the fact that the GSD is the same for each detector of the Xenics and Cardinal, the performance range of the MTF is also the same for each of the Xenics and Cardinal detectors. While the performance of the Cardinal detectors is still sufficient with a MTF larger than 0.6, the optical performance of the Xenics detectors are very close to the MTF threshold with 0.21. Furthermore, the range of the optical performance is very large in comparison to the Teledyne and Cardinal detectors and will therefore be further investigated and compared in their MTF components and profiles in 1D for the best and the worst case when using the Xenics XSW640.

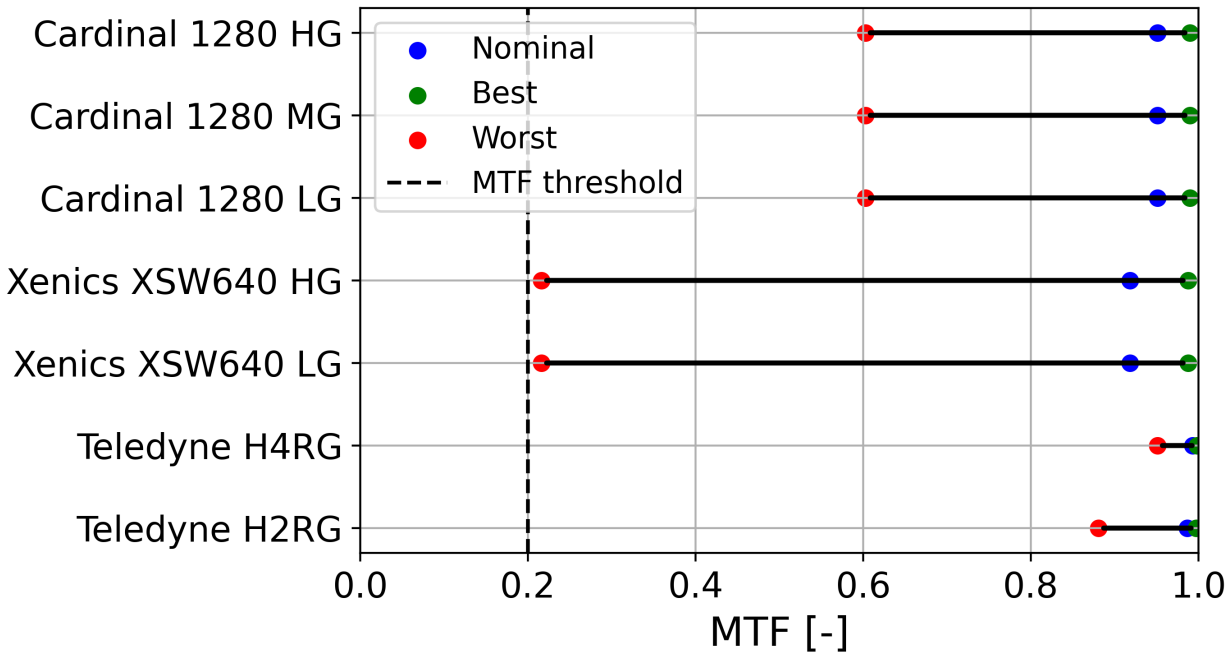

Figure 4.2: MTF for the considered SWIR detectors at the corresponding spatial frequency MTF($\xi_{Rayleigh}$) for best, nominal and worst case when observing the O_2 nightside airglow

The following is primarily intended as an exemplary analysis of optical performance to identify the need for adjustments in order to achieve the optimal design of the imaging system. Figure 4.3 shows the different MTF components and the total MTF over the spatial frequency given in the object space (see eq. 2.19) as introduced in section 2.2 for the current imaging system design with a focal length of 38.08 mm and a aperture diameter of 9.51 mm ($f/\# = 4$).
First of all, it can be seen that the pixel and sampling MTF are perfectly overlapping as expected being defined in the same way as described in the theoretical background. In addition, they have the biggest impact on the total MTF with increasing spatial frequencies compared to the lens and blur MTF. Nevertheless, the lens MTF still has the second biggest and significant impact on the optical performance, while the blur MTF does not affect the total MTF at all for the range of spatial frequencies, which is due to a vanishingly small pixel smear (see table 4.2) for an orbit altitude of 45 000 km. This demonstrates the various impacts of the current design choices on the optical performance of the imaging system, while the detector characteristics have the strongest impact as the pixel and sampling MTF are the decisive components of the total MTF.
Furthermore, it can be seen that for a quake with a magnitude of $M_S = 7.5$ (best case) and a corresponding wavelength of 800 km translating into the spatial frequency $\xi_{Rayleigh} = 0.001\,25\,\mathrm{km}^{-1}$, there is only a slight decrease in optical performance with a MTF = 0.99, which is also the case for the other SWIR detectors (see fig. 4.2).
In addition, the Nyquist criterion is clearly fulfilled as long as $\xi_{Rayleigh}$ is smaller than $\xi_{Nyquist}$ meaning that the corresponding line (blue-dotted) does not fall behind the Nyquist threshold (brown-dotted), which is clearly not the case here.

When now applying the MTF in 2D, as explained in section 2.2, figure 4.4 demonstrates that there is hardly any difference in the contrast between the perfect (MTF=1) and blurred image (MTF=0.99). Each image shows the emission in Rayleigh for a cut-out of the camera's FOV with the size of exactly one wavelength (see heading) in each dimension. In addition, the grid is scaled to the spatial resolution by the GSD, again confirming that the Nyquist criterion is clearly met in this case. Although this illustration refers to the Xenics XSW640, the results shown here can also be transferred to the other SWIR detectors, with the exception of the spatial resolution, since the optical performance in terms of MTF in the best case hardly differs from each other with MTF ≈ 1.

Moving on to the worst case scenario with a wavelength of 40 km and a corresponding spatial frequency of $\xi_{Rayleigh} = 0.025\,\mathrm{km}^{-1}$ results in clear differences regarding the optical performance when looking at the MTF profiles in figure 4.5. Although the MTF curves do not differ from the previous case, it is the spatial frequency at which the MTF is considered that is decisive. This becomes very clear when comparing the best and worst case using the Xenics XSW640 as the detector of the imaging system, because in the worst case the spatial frequency of the Rayleigh waves is larger than the Nyquist frequency (blue dotted line falls behind the brown dotted line) and, as already shown in Fig. 4.2 only just before the MTF threshold. Hence, not only the Nyquist condition is violated and thus the spatial resolution is insufficient, but also the optical performance in terms of image contrast is very poor compared to the other SWIR detectors discussed (Fig. 4.2).

Considering again the 2D-MTF (Fig. 4.6) with a FOV cut-out with the dimensions corresponding to the seismic wavelength of 40 km, two effects become clear compared to figure 4.4. First, since the GSD is too large in order to resolve the wavelength considered here (see heading), the violation of the Nyquist condition by the shifted and coarse grid becomes very evident. Secondly, it is no longer possible to distinguish between the peak and dip of the seismic wave due to the maximally increased background emission in the worst case, which underlines the poor SNR performance as previously discussed. The latter can also be transferred to the other considered detectors as their SNR values are in the same order of magnitude in the worst case (see Fig. 4.1).

To demonstrate the influence of the observed wavelengths and thus spatial frequencies only on the optical performance, without the degradation of contrast due to the changing background radiance in the analysed cases, the following figures A.1 and A.2 show FOV cut-outs for five seismic wavelengths in each case (see heading) **without** the background emission. This has the significant advantage that only the influence of the MTF on the images becomes explicitly clear, without considering the additional effect of the changing SNR performance on the image quality.
The strong contrast between the peaks (white) and the dips (black) of the waves remain almost unchanged in the best-case scenario due to the high MTF value near one caused by the low spatial frequency (Fig. A.1). Nevertheless, a slight blurring can be seen in the right image when the 2D MTF is applied.
Now turning to the worst case scenario, the effect of the applied MTF on the image contrast and therefore image quality finally becomes very striking in figure A.2. With an MTF value

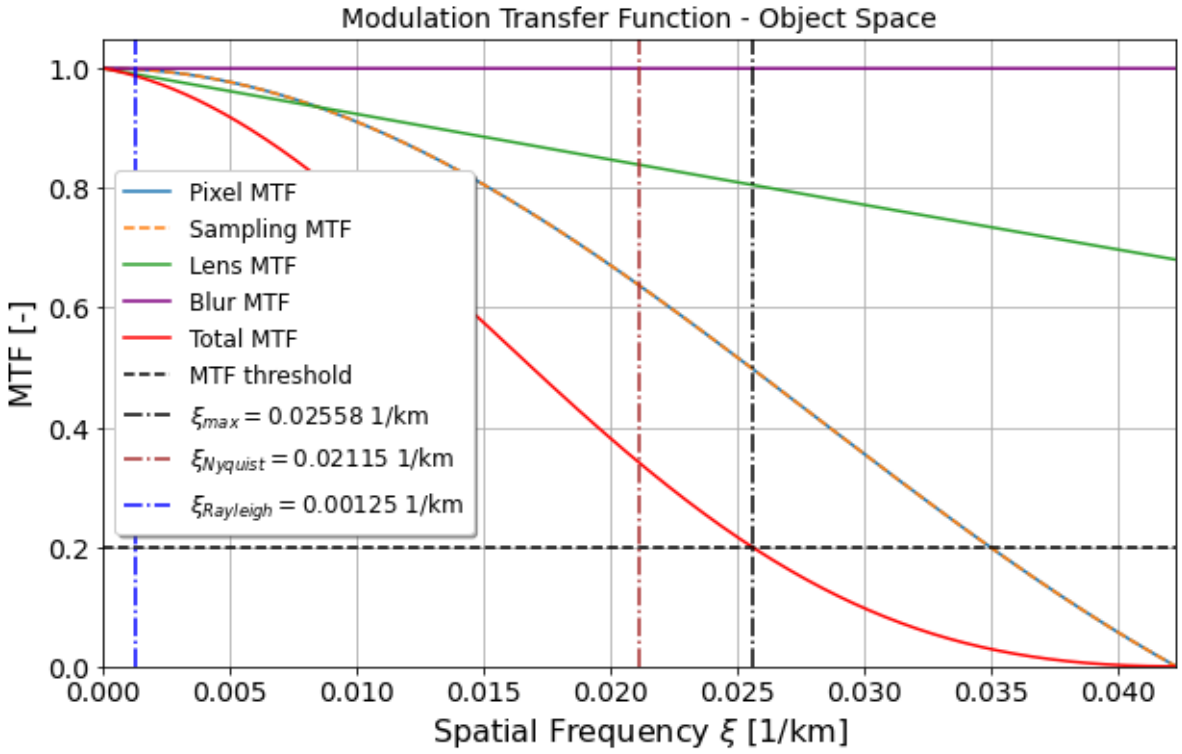

Figure 4.3: MTF as a function of the spatial frequency in object space for the current imaging system design using the Xenics XSW640 detector in the best case

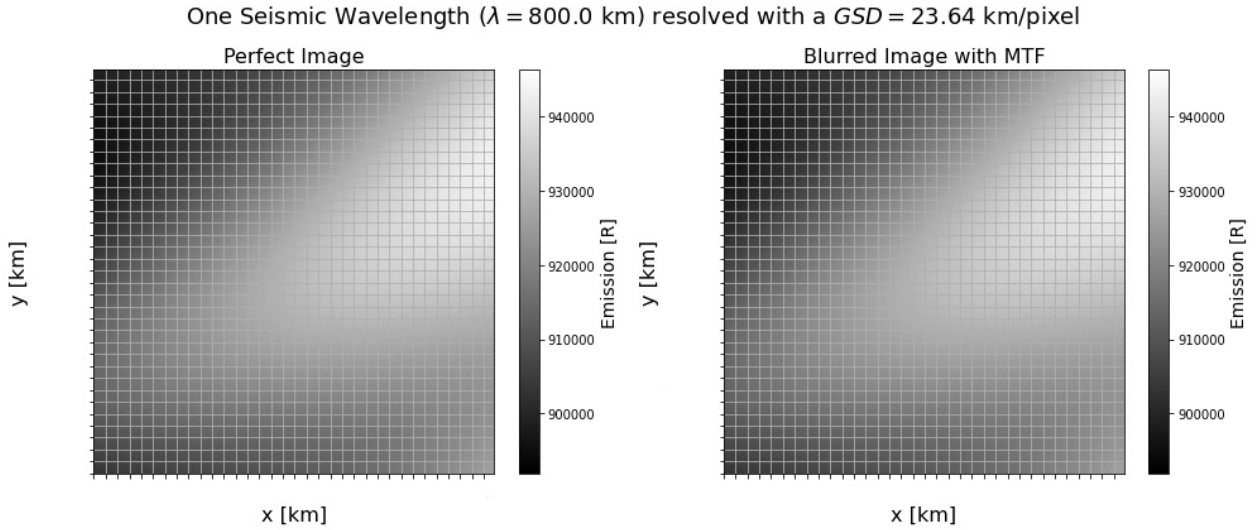

Figure 4.4: Contrast comparison for perfect (MTF = 1) and blurred image (applied MTF) with the expected emission in Rayleigh for a FOV cut-out (800 × 800 km) for a random background noise signal with $L_{\lambda_{peak}} = 0.02$ Wm^{-2}µm^{-1}sr^{-1} at 1.27 µm and a surface magnitude of $M_S = 7.5$ (best case) resulting in SNR = 0.14 using the Xenics XSW640 LG

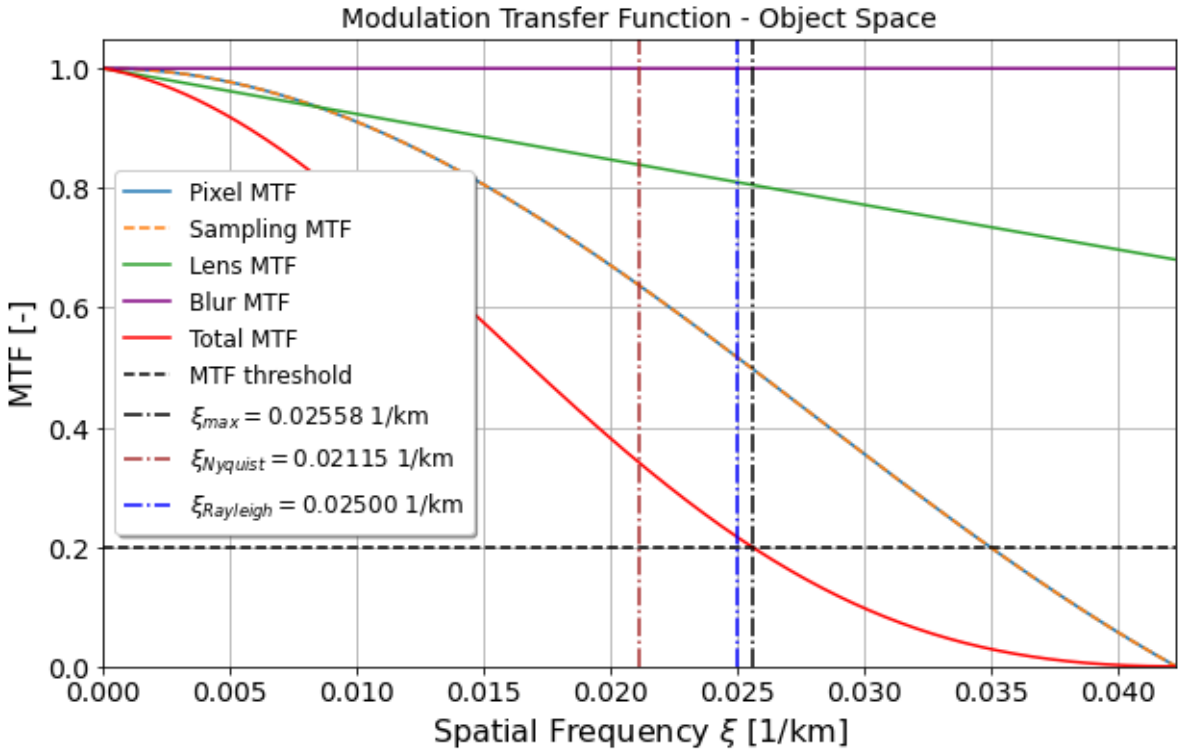

Figure 4.5: MTF as a function of the spatial frequency in object space for the current imaging system design using the Xenics XSW640 detector in the worst case

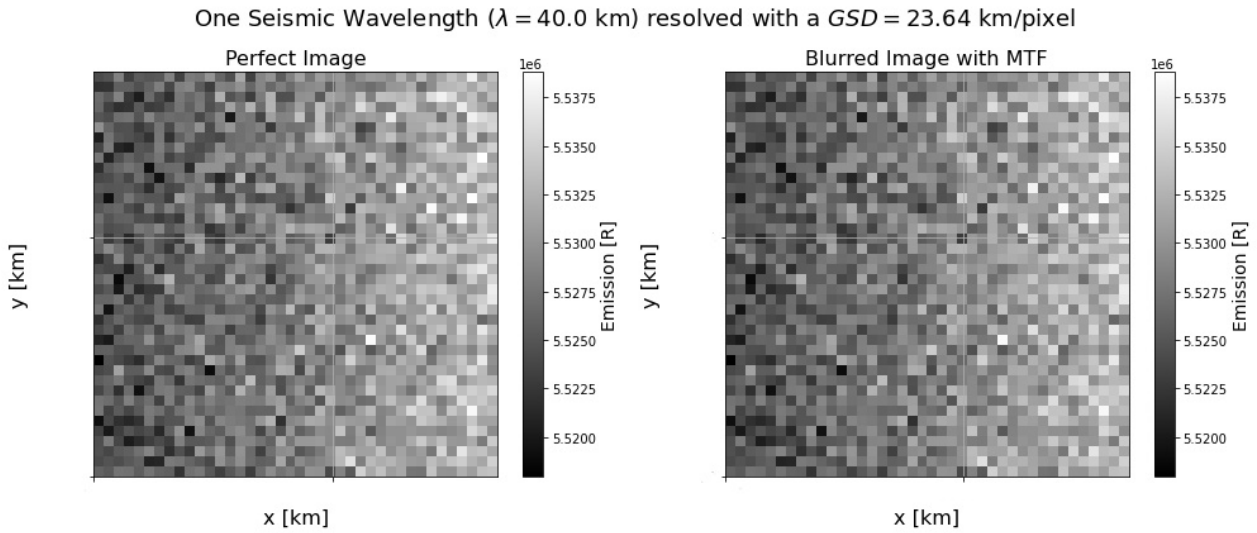

Figure 4.6: Contrast comparison for perfect (MTF = 1) and blurred image (applied MTF) with the expected emission in Rayleigh for a FOV cut-out (40 × 40 km) for a random background noise signal with $L_{\lambda_{peak}} = 0.12$ Wm^{-2}µm^{-1}sr^{-1} at 1.27 µm and a surface magnitude of $M_S = 5.5$ (worst case) resulting in SNR $= 3 \cdot 10^{-4}$ using the Xenics XSW640 LG

of around 0.2, the peaks and dips of the Rayleigh waves corresponding to a surface magnitude of $M_S = 5.5$ are barely distinguishable from each other in the blurred image on the right. It is worth mentioning that these are also concentric waves with the same origin as in the previous image, but here the curvature of the waves is no longer discernible due to the higher zoom and the smaller wavelength.

Figure 4.7 and 4.8 ultimately show the full FOV for the best and worst case respectively, using the Xenics XSW640 as the detector, where the full disk of Venus including the limb darkening effect can be seen from the assumed altitude (see heading). Due to the different number of pixels in the x and y directions, the FOV is shown as the expected rectangle (see table 4.2). At first glance, it is immediately apparent that in the worst case (Fig. 4.8), no waves can be seen at all confirming the poor SNR performance. In addition, the diminishing effect of the MTF is barely visible, as there is no contrast pattern to be compared due to the absence of detectable waves.

Although it is possible to distinguish between the wave peak and dip in the best case (Fig. 4.7), the SNR values are still too low for detection, as previously discussed. Here, the difference between the perfect and blurred image is also barely recognisable and refers to the still high MTF corresponding to the low spatial frequency affecting the MTF and therefore optical performance.

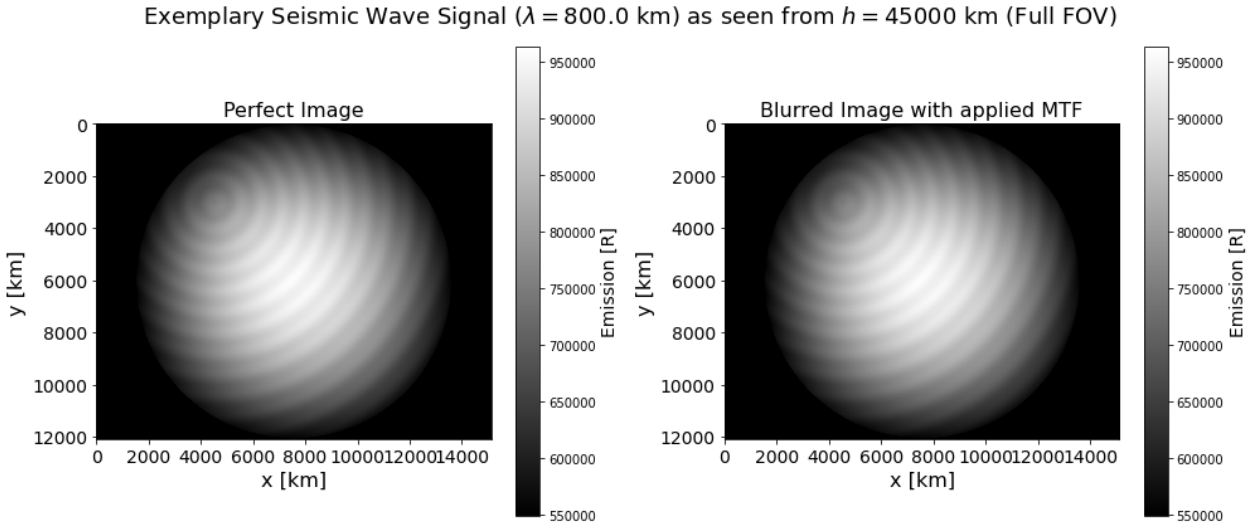

Figure 4.7: Contrast comparison for perfect (MTF = 1) and blurred image (applied MTF) with the expected emission in Rayleigh with Venus' full disk in the FOV for a random background noise signal with $L_{\lambda_{peak}} = 0.02$ Wm^{-2}µm^{-1}sr^{-1} at 1.27 µm and a surface magnitude of $M_S = 7.5$ (best case) resulting in SNR = 0.14 using the Xenics XSW640 LG

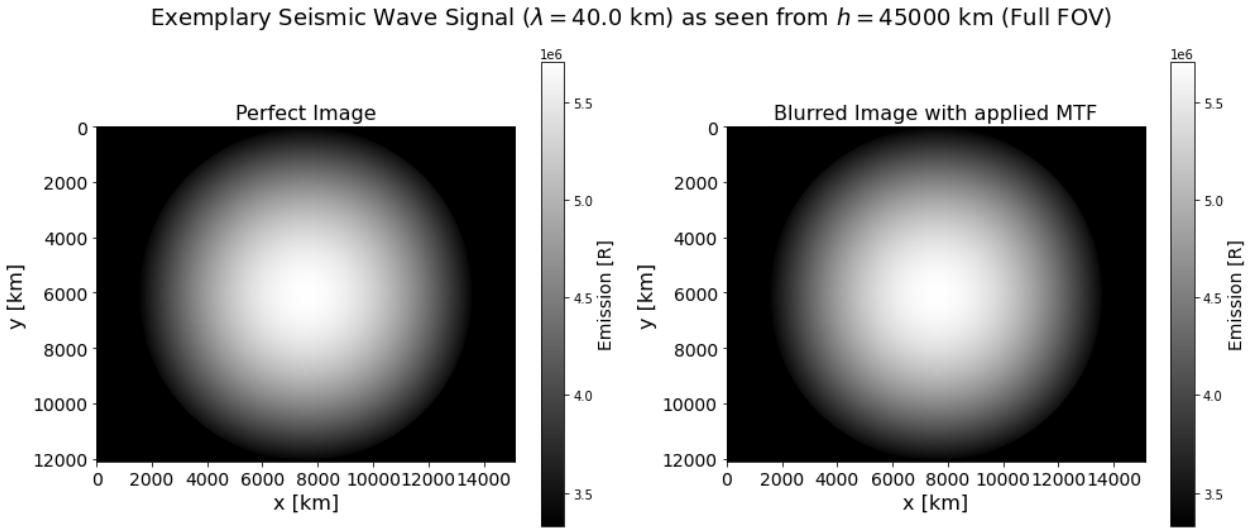

Figure 4.8: Contrast comparison for perfect (MTF = 1) and blurred image (applied MTF) with the expected emission in Rayleigh with Venus' full disk in the FOV for a random background noise signal with $L_{\lambda_{peak}} = 0.12$ Wm^{-2}µm^{-1}sr^{-1} at 1.27 µm and a surface magnitude of $M_S = 5.5$ (worst case) resulting in SNR = $3 \cdot 10^{-4}$ using the Xenics XSW640 LG

Another important factor when analysing the impact of the selected detector for a camera system is the maximum exposure time until full well capacity is reached. This is necessary and crucial especially, when considering stacking in order to improve the SNR performance. In the previous cases, an exposure time of 1 s was initially assumed on the basis of [43, 29] in order to ensure comparability of the detectors solely with regard to the figures of merit. However, Fig. 4.9 shows that the maximum exposure time depends not only on the signal and background emission determining the incoming photon flux, but also on the characteristic full-well capacity of each detector. In the case of the Xenics XSW640 HG and Cardinal 1280 HG with a full well capacity of 63 and 10 ke$^-$, respectively, an exposure time of one second cannot even be achieved regarding the incoming photon flux. On the other hand, it is clear that much longer maximum exposure times and therefore a higher stacking factor are possible in medium and high gain mode. It is also clear that the maximum exposure time increases significantly from worst to best case, which is due to the reduced dominant photon flux of the assumed background signal compared to the actual signal from the atmospheric-coupled Rayleigh waves.

It should be noted that only the maximum exposure time regarding the worst case is relevant for further consideration of the potential detectors, as a higher exposure time would lead to saturation of the pixels in the nominal or best case. For the Teledyne detectors, this results in maximum exposure times of 1.25 s and 1.8 s for the H2RG and H4RG, respectively, and 25 s and 50 s for the Cardinal 1280 MG and LG, respectively. Lastly, the maximum exposure time when using the Xenics XSW640 LG is 10.1 s.

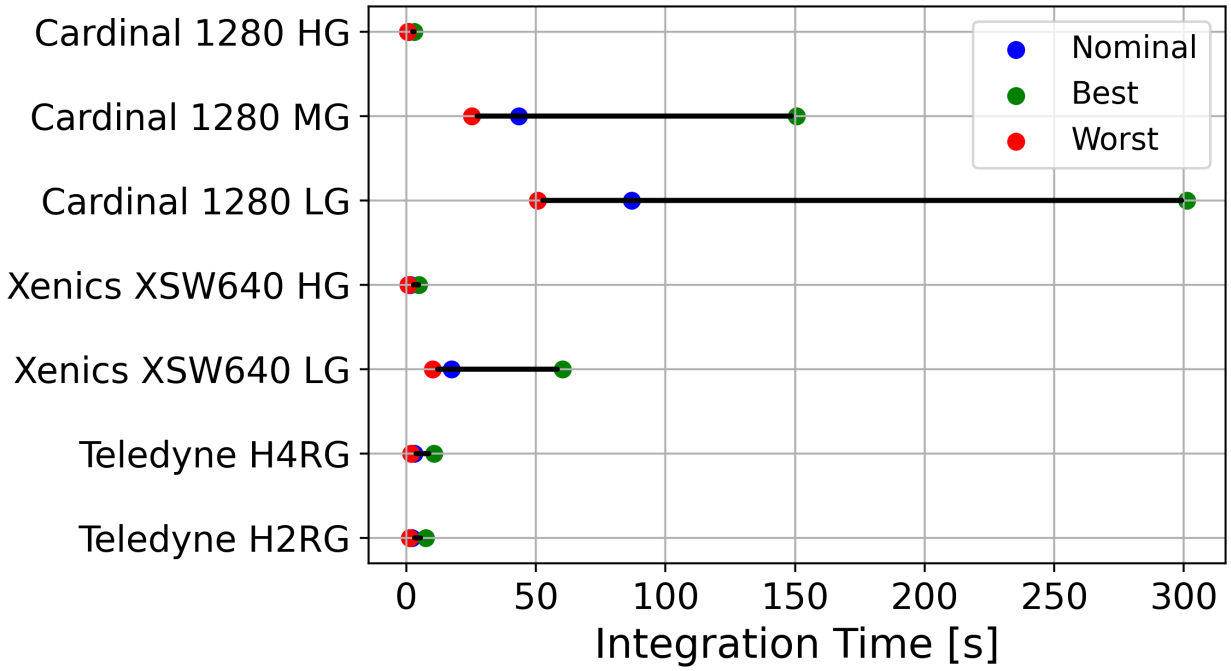

Figure 4.9: Effect of the detector selection on the maximum integration time with respect to the full well capacity in the best, nominal and worst case

On the basis of the results analysed with regard to the worst- to best-case-range, it is already

possible to exclude a number of detectors from further analysis at this point. On the one hand, the Xenics XSW640 HG is not considered any further, because the spatial resolution (GSD) in the worst case violates the Nyquist criterion with poor SNR, which could possibly be improved by binning, but this would result in a further reduction of the spatial resolution which would be destructive. On the other hand, the possible maximum integration time is shorter than previously assumed, which would not only result in a poorer SNR, but would also disallow the possibility of later achieving a better SNR by stacking. In addition, the Xenics XSW640 LG is not considered any further, as the MTF performance in the worst case is already close to the specified limit, and an increase in integration time or stacking as well as in spatial resolution through binning would exceed this limit. The SCD Cardinal HG will also not be considered any further for the same reasons as justified for the Xenics XSW640. Finally, due to its better performance in terms of figures of merit, the Teledyne H4RG replaces the H2RG as the baseline detector for the following trade-offs.

4.1.2 Middle Wavelength Infrared Detectors

With the second possibility to detect seismic Rayleigh waves on Venus' dayside when observing the NLTE emission at 4.3 µm infrared detectors are required with sufficient detectivity across the middle wavelength infrared spectrum (MWIR). Consequently, three potential detectors (see Table 4.3) shall be considered and will be analysed regarding their performance and their effect on the imaging system's performance as previously conducted for the SWIR detectors.

First of all, the Teledyne H2RG/H4RG [45, 52] will also be considered for the observation of the dayside, but this time with a higher cut-off wavelength in order to achieve sufficient detectivity between 3.0 µm to 5.0 µm and therefore also at 4.3 µm. The operational temperature is lower than in the previous case at 37 K, thus leading to higher cooling requirements. Quantum efficiency η and the full-well capacity are also slighty lower, while all the other detector characteristics remain the same as compared to the SWIR version.

In addition, the Raytheon Phoenix, made out of InSb, has relatively similar characteristics to the Teledyne H2RG [4]. However, it has a higher quantum efficiency and full well capacity, and with an operating temperature of 30 K it has the highest cooling requirements among all considered detectors in this thesis. It should also be noted that the Raytheon Phoenix has a spectral range of 0.4 µm to 5.5 µm and would also be suitable for observing the nightside at 1.27 µm.

The third option to be analysed will be the Blackbird 1920 from SCD [15] made out of InSb, as it has a spectral range of 3.6 µm to 4.9 µm and thus also suitable for observing the dayside signal. Furthermore, two gain modes (low and high) are available which, as in the previous case, affect the readout noise and full well capacity. With a slightly higher operating temperature of 77 K, the cooling requirements are slightly lower, but results in a higher dark current. All relevant characteristics of the potential MWIR detectors for the observation of the Venus dayside are listed in table 4.3.

Table 4.3: Overview of the material, spectral range λ, operational temperature T, pixel size p_{pitch}, number of pixels n_{pixel}, quantum efficiency η, dark current I_{dark}, readout noise n_{noise} and full well capacity FW of the selected MWIR detectors: Teledyne H2RG/H4RG, Raytheon Phoenix and SCD Blackbird 1920 LG/HG for the CO_2 dayside NLTE emission observation of Venus

Parameter	**Teledyne**		**Raytheon Phoenix**	**SCD Blackbird 1920**		Unit
	H2RG	H4RG		LG	HG	
Material	HgCdTe		InSb	InSb		-
λ	3.0 - 5.0		0.4 - 5.5	3.6 - 4.9		µm
T	37		30	77		K
p_{pitch}	18	15	25	10		µm
n_{pixel}	2048×2048	4096×4096	2048×2048	1920×1536		-
η	>70		>88	>80		%
I_{dark}	8e-21	8.8e-22	1.6e-19	0.8e-12		A
n_{noise}	100	17.5	20	800	60	e^-
FW	65		300	4000	300	ke^-

With the same geometrical specifications for the Teledyne H2RG/H4RG MWIR compared to the SWIR version the affected parameters of the imaging system remain the same (see Table 4.4) as the orbit altitude and f-number also remain unchanged compared to the nightside scenario (see Table 3.6). Due to larger pixels and an equal number of pixels compared to the Teledyne H2RG the imaging system's size results to be larger in terms of focal length and aperture diameter when using the Raytheon Phoenix with the same orbit altitude (eq. 3.4). In addition, FOV and iFOV and therefore spatial resolution (GSD) and pixel smear remain the same as the number of pixels are equivalent for the Raytheon Phoenix and Teledyne H2RG.

Based on the same ratio of number of pixels in each direction regarding the SCD Blackbird 1920 (1920/1536 = 5/4) compared to the Xenics XSW640 (640/512 = 5/4) and SCD Cardinal 1280 (1280/1024 = 5/4), focal length and aperture diameter as well as FOV are equivalent. Furthermore, the lower number of pixels compared to the Teledyne and Raytheon detectors result again in a slightly higher GSD, and thus in the lowest pixel smear among the discussed MWIR detectors when integration time and ground velocity are fixed.

As in the previous case, the influence of the detectors on the performance of the imaging system, in particular on the figures of merit, shall be investigated and analysed in the following. Fig. 4.10 shows the SNR range from worst to nominal to best case on the dayside for the MWIR detectors introduced above. It is clear that in the current configuration neither of the Blackbird 1920 detectors reaches the minimum threshold in any case. In contrast, using the Teledyne and Raytheon detectors in the best case result in sufficient SNR performance, which is well above the minimum threshold. The maximum SNR value using the Raytheon Phoenix as the detector is due to the higher quantum efficiency compared to the Teledyne detectors (see Table 4.3).
However, the SNR values in the nominal and worst case are still significantly smaller than

Table 4.4: Determined focal length f, aperture diameter D, (instantaneous) field-of-view $(i)FOV$, ground sampling distance GSD and pixel smear PS of the imaging system based on the selected MWIR detector for observing Venus' dayside

Parameter	**Teledyne**		**Raytheon Phoenix**	**SCD Blackbird 1920**		Unit
	H2RG	H4RG		LG	HG	
f	137.075	228.46	190.38	38.076		mm
D	34.27	57.11	47.595	9.51		mm
FOV	15.31×15.31		15.31×15.31	19.08×15.31		deg
$iFOV$	0.1313	0.0656	0.1313	0.175		mrad
GSD	5.909	2.955	5.909	7.879		$\frac{\text{km}}{\text{pixel}}$
PS	1.57	3.139	1.57	1.18		%

the required SNR=3, with the Teledyne H4RG still performing best with $\text{SNR}_{\text{nominal}} \approx 1$. In the worst case, the SNRs are still almost zero, with values between $6 \cdot 10^{-4}$ (SCD Blackbird 1920 LG) and $5 \cdot 10^{-3}$ (Raytheon Phoenix), similar to the nightside scenario.

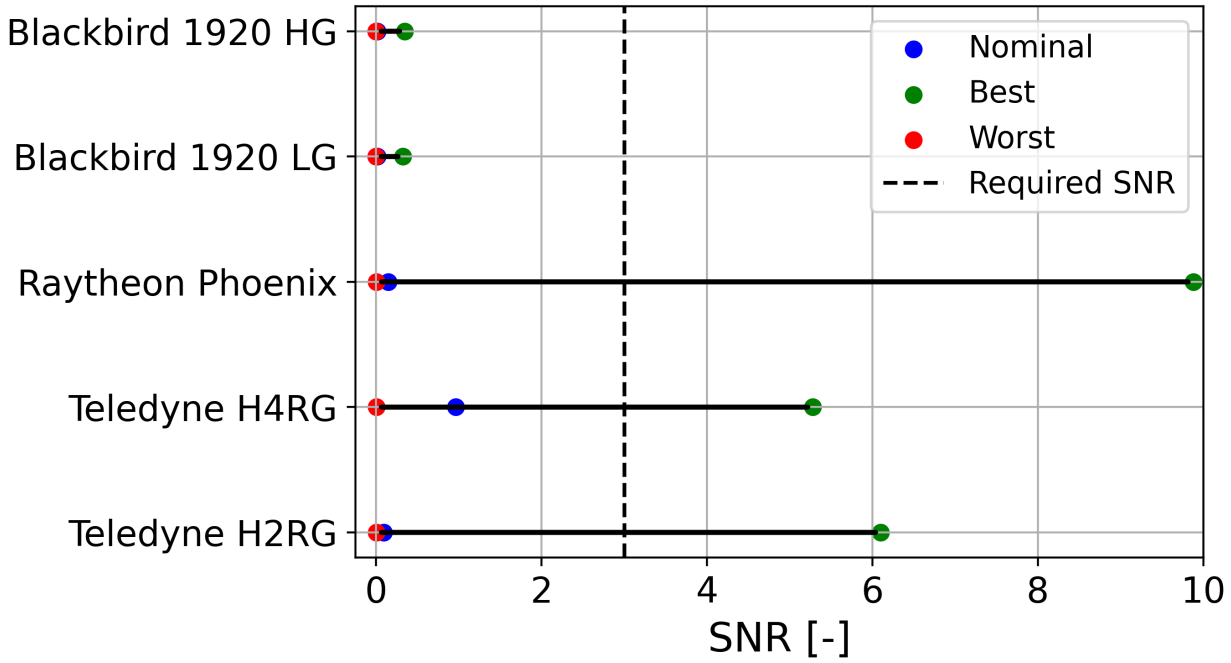

Figure 4.10: SNR performance of the considered MWIR detectors for best, nominal and worst case in the current baseline design

The SCD Blackbird 1920 detectors also perform worst when considering the impact on optical performance based on the MTF values at the spatial frequency corresponding to the seismic quake in each case, although in the worst case an MTF of around 0.5 is still well above the threshold (see Fig. 4.11). However, the optical performances of the Teledyne and Raytheon detectors are significantly better in terms of image contrast when applying the MTF. Similarly to the nightside scenario, the Teledyne H4RG is the best performer with MTF values

above 0.88, due to the low GSD. In both, the nominal and the best case, there are hardly any differences when using the Teledyne and Raytheon detectors with values of 0.97 and 0.99 for the nominal and the best case respectively, barely diminishing the optical performance in terms of contrast loss in the image. As for the previous scenario, the performance of the

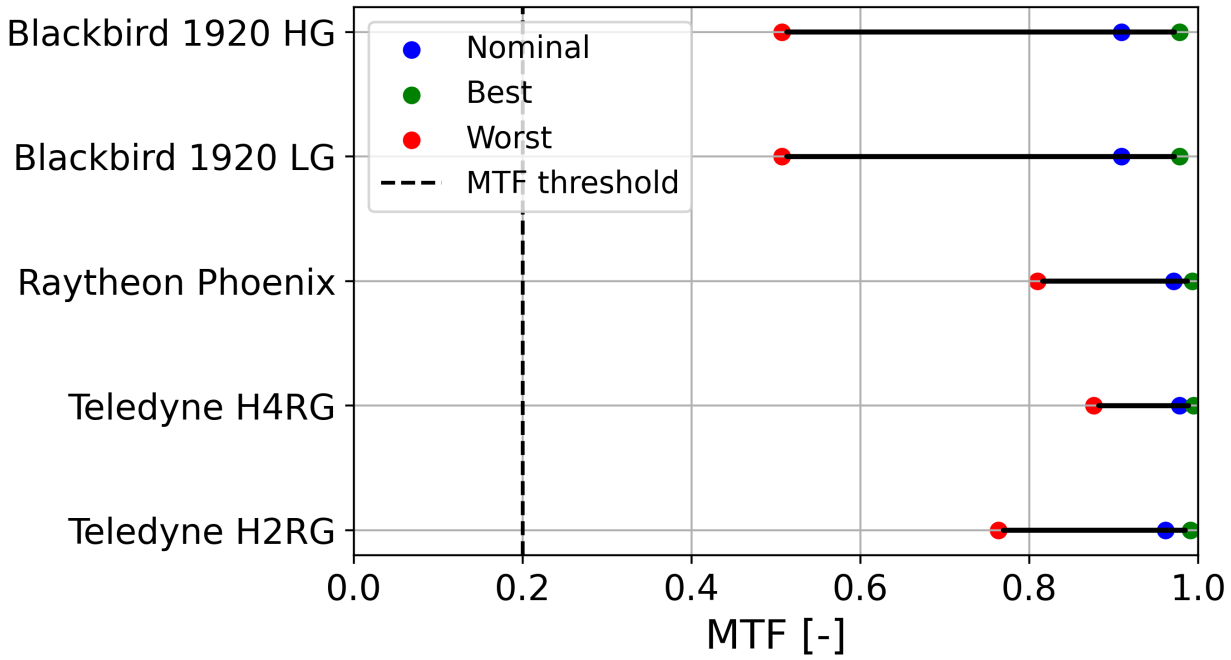

Figure 4.11: MTF for the considered MWIR detectors at the corresponding spatial frequency MTF($\xi_{Rayleigh}$) for best, nominal and worst case when observing the CO_2 dayside NLTE emission

MTF will be further analysed by examining the individual components and their impact on the total MTF. Figure 4.12 shows the MTF curves over spatial frequency in object space using the Raytheon Phoenix exemplary for the observation of the dayside. Compared to the nightside scenario, the spatial frequency range has shifted towards lower spatial frequencies because the cut-off frequency (eq. 2.12) is lower due to the higher observed optical wavelength of 4.3 µm.
Another significant difference compared to the nightside is that the contribution of MTF_{lens} has a greater effect on the total MTF than the pixel and sampling MTF, which is again due to the higher observed wavelength while the pixel and sampling MTF effect remains similar, thus leading to a greater reduction of the total MTF. Moreover, the contribution of MTF_{blur} remains almost unchanged and is still not noticeable due to the unchanged orbital altitude and correspondingly very low ground speed. Furthermore, it can also be seen that the spatial frequency corresponding to the Rayleigh wave and the Nyquist criterion are the same as in the best case on the nightside, but because of the shift towards smaller spatial frequencies, the Nyquist criterion and the MTF threshold are located closer together. In this case, the analysis of the optical performance can be seen as representative for all the considered MWIR detectors for the observation of the dayside as their MTF performance is almost the same in the best case (see Fig. 4.11).

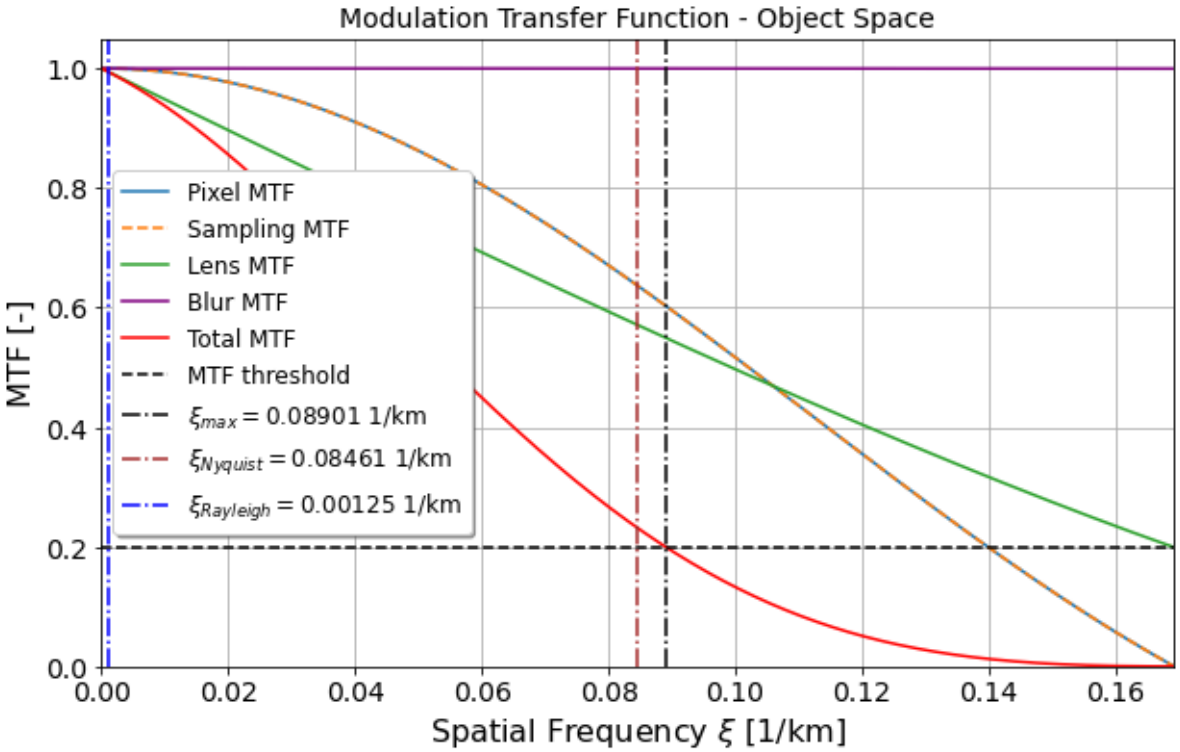

Figure 4.12: MTF as a function of the spatial frequency in object space for the current imaging system design using the Raytheon Phoenix detector in the best case

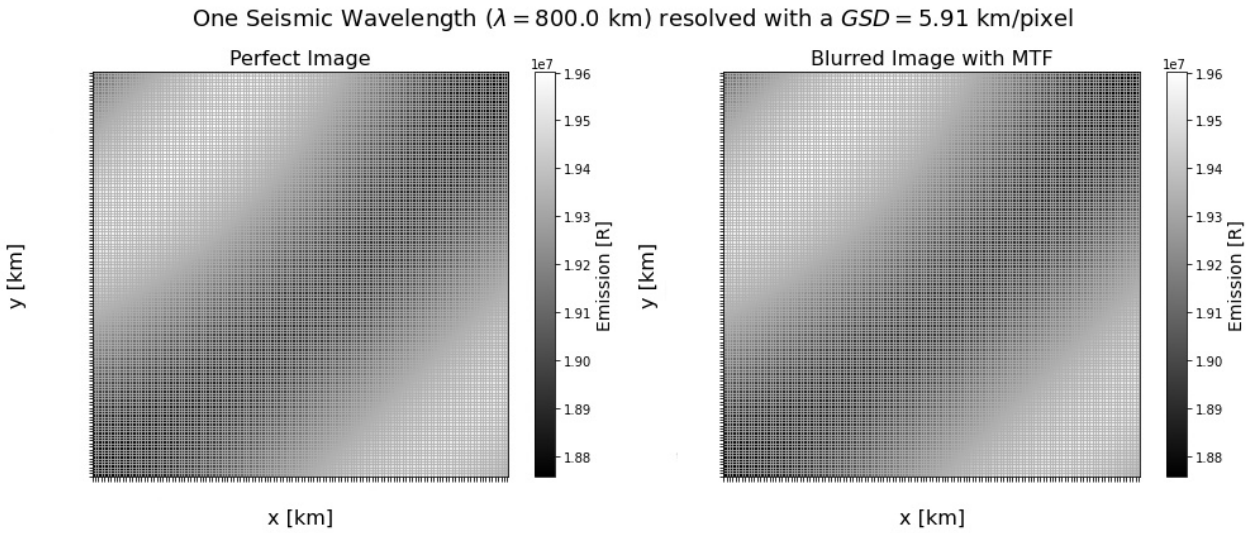

Figure 4.13: Contrast comparison for perfect (MTF = 1) and blurred image (applied MTF) with the expected emission in Rayleigh for a FOV cut-out (800 × 800 km) for a random background noise signal with $L_{\lambda_{peak}} = 0.02\,\mathrm{Wm^{-2}\mu m^{-1}sr^{-1}}$ at 4.3 µm and a surface magnitude of $M_S = 7.5$ (worst case) resulting in SNR = 10 using the Rayleigh Phoenix

Looking at the resolution capabilities for this case with figure 4.13 in 2D, it becomes clear that the spatial resolution requirement is abundantly met when using the Raytheon Phoenix detector. In this case the seismic Rayleigh wave is resolved by over 100 pixels with a GSD of 5.909 km per pixel (equivalent to the Teledyne H2RG), therefore leading to the very fine grid in the plot. Additionally, it also demonstrates the strong SNR performance as the peak and dip of the wave are clearly separable from each other and the image on the right with the applied image seems to have the same contrast.
As the GSD is similar for all detectors, this result can be transferred to the Teledyne and Blackbird 1920 detector as well, whereas with the Teledyne H4RG the resolution would be even better, while it would be slightly reduced using the Blackbird 1920 (see Tab. 4.4).

For the worst case the MTF curves remain the same, as already discussed in the previous section. The only difference again, is that the corresponding spatial frequency for the Rayleigh waves with a smaller wavelength is larger leading to a decrease of the total MTF to 0.8, which is still well above the required threshold. However, this shows that even in the worst case assuming wavelengths of 40 km there is still much potential to enhance the SNR performance with binning as the $\xi_{Rayleigh}$ is much smaller than $\xi_{Nyquist}$.
Compared to the worst case on the nightside using the Xenics XSW640, in Fig. 4.15 you can see that even the small waves are sufficiently resolved in the worst case using the Raytheon Phoenix. More than 6 pixels are used for resolving an area corresponding to the wavelength in the worst case, leaving the potential to further reduce the resolution by binning in order to increase the SNR for detectability. However, as the SNR is very low in this case and a wave signal is therefore not distinguishable from the noisy background similar to the worst case on the nightside (see fig. 4.6).

As in the previous case, figure 4.16 shows the full FOV of the imaging system when using the Raytheon Phoenix as the MWIR detector. Again, the full Venusian disk with limb darkening is clearly visible from the presumed orbital altitude, with an exemplary concentric wave for a strong seismic quake in the best case, as in the nightside scenario (Fig. 4.7). The FOV is a square in this case because the number of pixels is the same in both dimensions for the Raytheon Phoenix. In addition, due to the high MTF value corresponding to the spatial frequency $\xi_{Rayleigh}$ there is hardly any difference between the ideal case with MTF = 1 (left) and the image with the MTF applied (right), shown in figure 4.16. It should also be noted that the limb darkening, as discussed in the theory section, is slightly weaker on the dayside and therefore the waves can be seen even further towards the limb of Venus on the dayside.

Furthermore, figure 4.17 shows the full FOV for the worst case demonstrating that it is no longer possible to distinguish the peaks and dips of the seismic wave against the maximal background signal in the worst case on the dayside. In the blurred image on the right it is noticeable that the image appears slightly darker due to the reduced contrast of about 20% (see fig. 4.11) when applying the corresponding MTF in 2D.

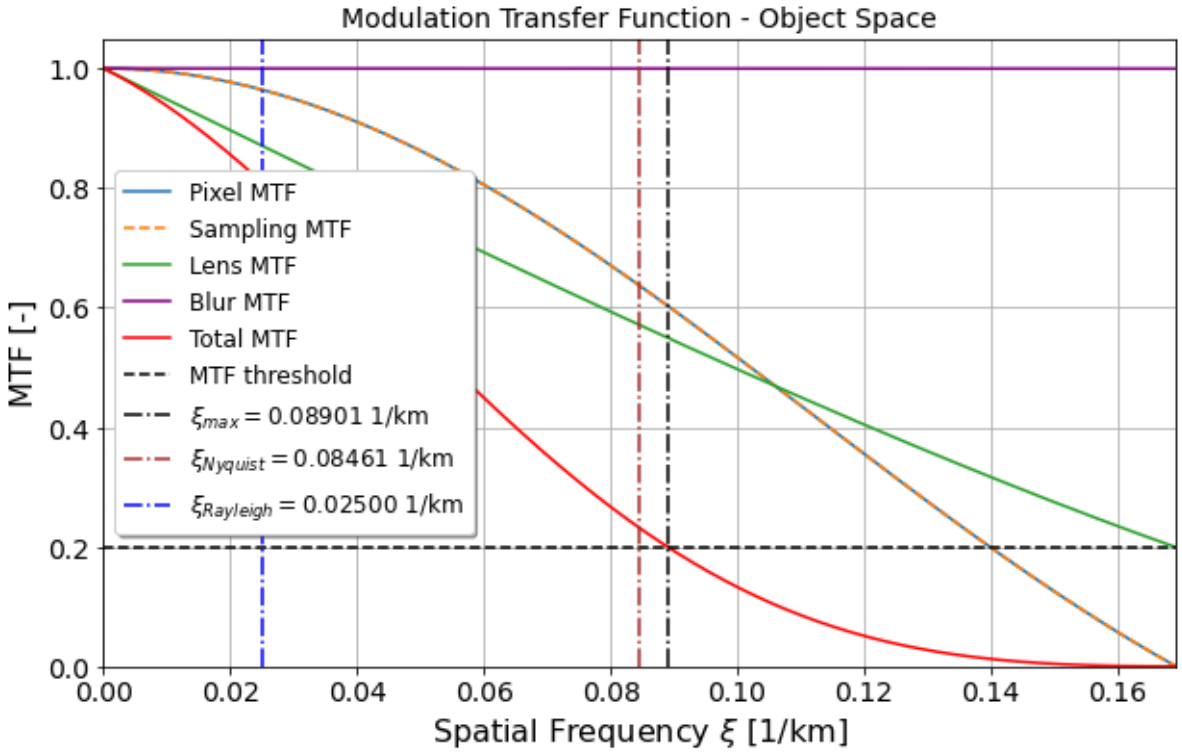

Figure 4.14: MTF as a function of the spatial frequency in object space for the current imaging system design using the Raytheon Phoenix detector in the worst case

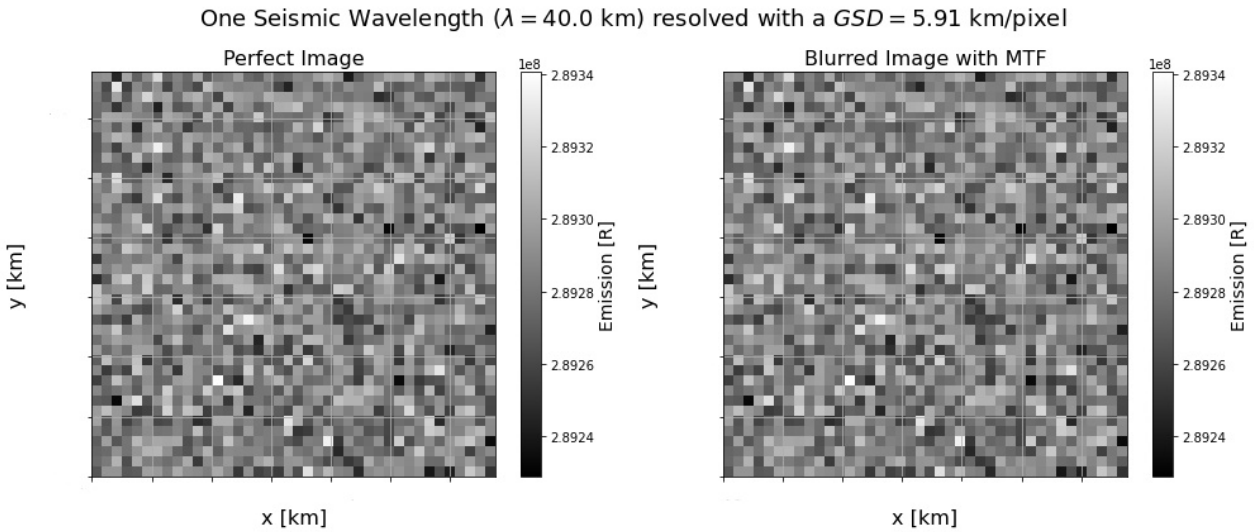

Figure 4.15: Contrast comparison for perfect (MTF = 1) and blurred image (applied MTF) with the expected emission in Rayleigh for a FOV cut-out (40 × 40 km) for a random background noise signal with $L_{\lambda_{peak}} = 0.30\,\mathrm{Wm^{-2}\mu m^{-1}sr^{-1}}$ at 4.3 µm and a surface magnitude of $M_S = 5.5$ (worst case) resulting in SNR $= 5 \cdot 10^{-3}$ using the Rayleigh Phoenix

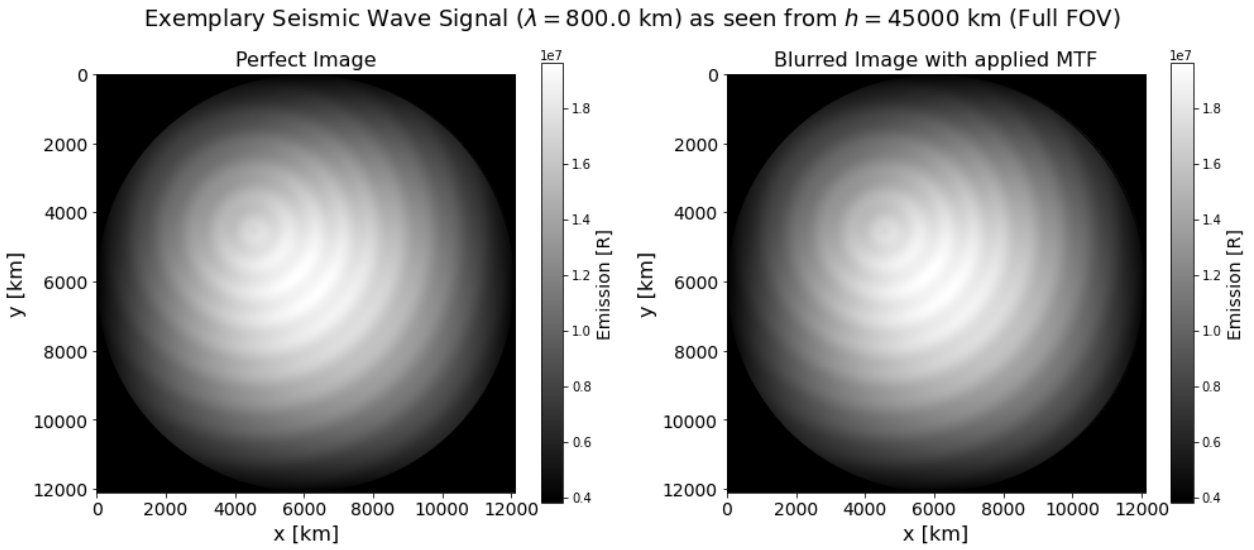

Figure 4.16: Contrast comparison for perfect (MTF = 1) and blurred image (applied MTF) with the expected emission in Rayleigh with Venus' full disk in the FOV for a random background noise signal with $L_{\lambda_{peak}} = 0.02\,\mathrm{Wm^{-2}\mu m^{-1}sr^{-1}}$ at 4.3 µm and a surface magnitude of $M_S = 7.5$ (best case) resulting in SNR = 10 using the Rayleigh Phoenix

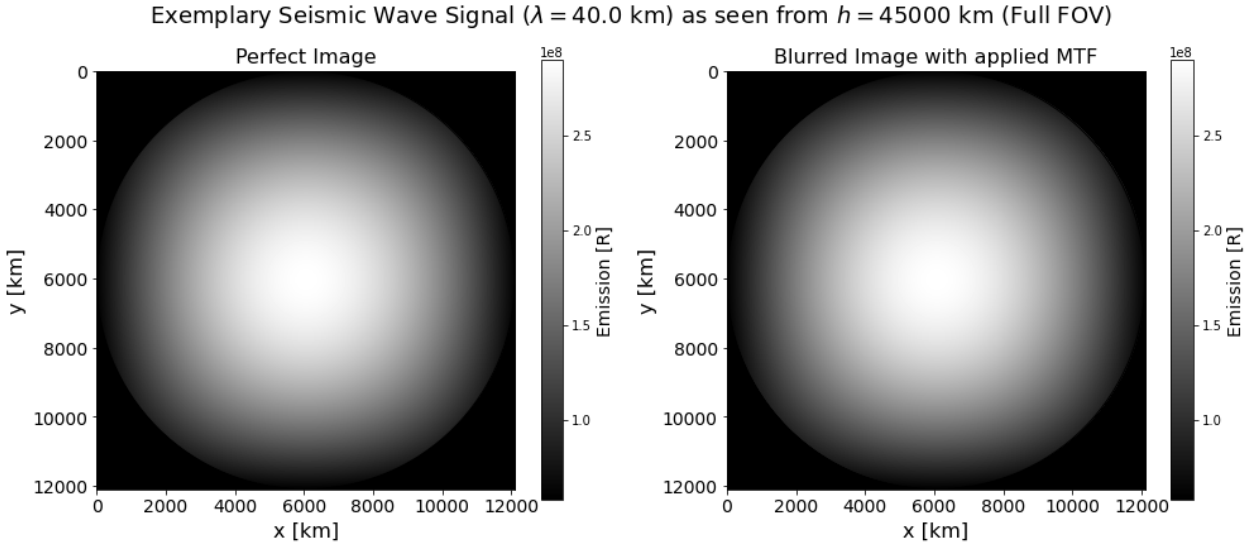

Figure 4.17: Contrast comparison for perfect (MTF = 1) and blurred image (applied MTF) with the expected emission in Rayleigh with Venus' full disk in the FOV for a random background noise signal with $L_{\lambda_{peak}} = 0.30\,\mathrm{Wm^{-2}\mu m^{-1}sr^{-1}}$ at 4.3 µm and a surface magnitude of $M_S = 5.5$ (worst case) resulting in SNR = $5 \cdot 10^{-3}$ using the Rayleigh Phoenix

The assumed baseline integration time of 1 s was chosen for all considered MWIR detectors in order to provide better comparability in terms of performance. However, as the full well capacity of the detectors may be exceeded with this assumed integration time, the maximum possible integration time is shown in Fig. 4.18 as a range from worst over nominal to best case for each MWIR detector.

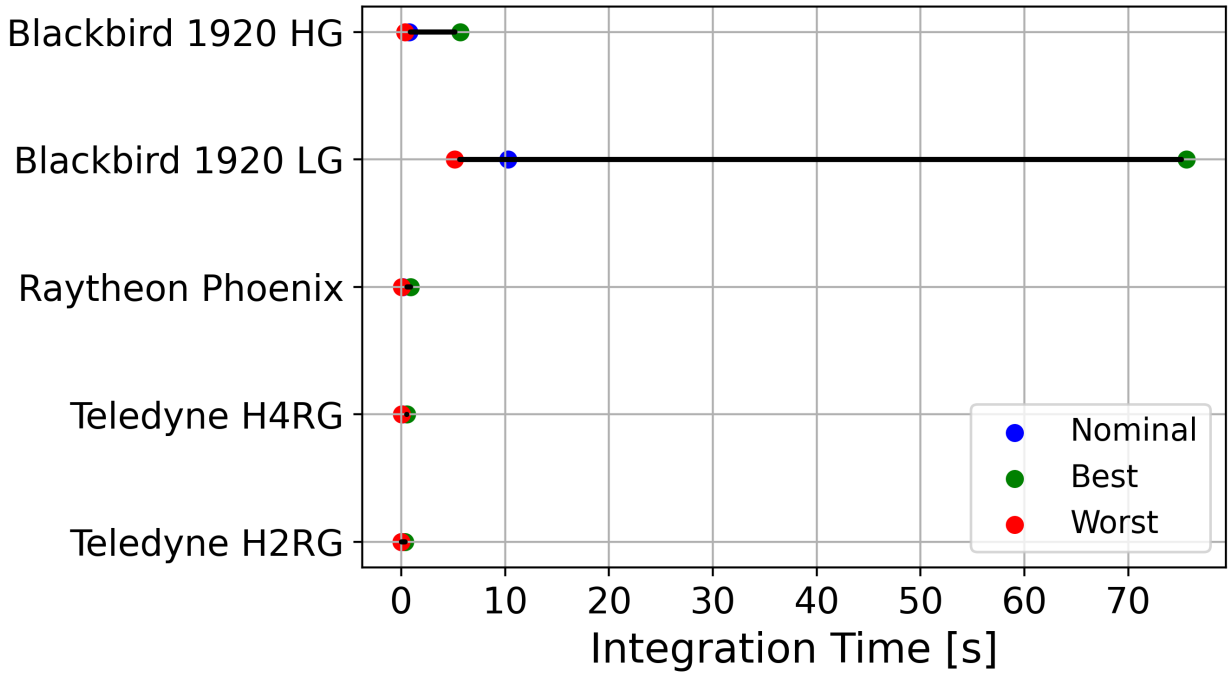

Figure 4.18: Effect of the detector selection on the maximum integration time with respect to the full well capacity in the best, nominal and worst case

At first sight it becomes clear that the Blackbird 1920 LG allows very long integration times compared to the other detectors, which is due to its higher full well capacity of 4000ke$^-$ (see Tab. 4.3). Especially in the worst case, a maximum integration time of 5 s is possible when using the Blackbird 1920 LG, and therefore higher than the currently assumed value giving the greatest potential for enhancing the SNR performance with stacking compared to the other MWIR detectors. Secondly, it is noticeable that the Blackbird 1920 HG allows significantly longer integration times than the Raytheon Phoenix, especially in the best case, although both have the same full well capacity of 300ke$^-$. However, the Raytheon Phoenix has a higher quantum efficiency than the Blackbird 1920 HG (Table 4.4), which means that more photons will be collected and hence the detector charges more quickly.
Nevertheless, considering the worst case, maximum integration times of 0.06 s and 0.38 s are possible when using the Raytheon Phoenix and Blackbird 1920 HG respectively and are thus significantly below the assumed value of 1 s. For the Teledyne detectors, only a maximum integration time of 0.037 s (H4RG) and 0.025 s (H2RG) is possible due to the relatively low full well capacity (Tab. 4.4). The significantly lower maximum integration times despite similar full well capacities of the SWIR detectors are mainly due to the significantly higher background signal on the dayside compared to the nightside.

In summary, none of the MWIR detectors can be excluded on the basis of optical performance, as they still exceed the MTF threshold for the smallest expected waves in the worst case. However, the SNR performance and therefore the detectability is not sufficient in all cases in the current configuration when considering both SCD Blackbird 1920 detectors. Since it is not possible to improve the SNR of the Blackbird 1920 HG by increasing the integrating time (lower maximum integration time as assumed), it will not be considered any further.
In addition, it must be examined whether the SNR requirement can still be met with the lower maximum integration times compared to the assumed value with respect to reaching the full well capacity. Moreover, the SNR performance needs to be improved especially in the worst and nominal case and due to the reason that the Teledyne H4RG has shown the best performance in the nominal case, further showing sufficient SNR performance in the best case, it will be the baseline detector for the dayside observation below.

4.2 Bandwidth of Optical Filter

In order to achieve a possible improvement in performance, particularly in terms of SNR, a more suitable choice of the bandpass will be examined in the following. The optimisation focuses on the choice of the centre wavelength (CWL), the bandpass bandwidth $\Delta\lambda$ and the associated maximum integration time, which is determined by the worst case for each bandpass option. Since the Teledyne H4RG was chosen as the new baseline detector for both, day- and nightside scenario, it gives sufficient comparability of the results in this trade-off.

For both scenarios, three bandpass filters of different bandwidths are going to be tested (Table 4.5), where the bandwidth shall based on industry standards [9, 8, 48, 47]. In addition to the baseline bandpass, which constitutes a wide bandpass in both cases including the full spectrum of the O_2 airglow when observing at 1.27 µm and the double peak at 4.3 µm of the CO_2 NLTE emission. Furthermore a narrow bandpass will also be considered along with the bandpasses used by [43] as an intermediate version with respect to the day- and nightside.

Table 4.5: Bandpass specifications for the day and nightside signal using the Teledyne H4RG

Parameter	**Nightside**			**Dayside**			Unit
	Baseline	VAMOS	Narrow	Baseline	VAMOS	Narrow	
CWL	1.27			4.3	4.28		µm
$\Delta\lambda$	20	12	2	100	30	15	nm
$t_{int,max}$	1.8	3	18	0.037	0.12	0.24	s

First of all, the narrow bandpass for the nightside signal is chosen with a bandwidth of 2 nm in order to include the peak as accurately as possible, but at the same time as narrow as possible regarding to the results of [6]. For observing the dayside, the narrow bandpass bandwidth is half of the VAMOS bandwidth with a CWL of 4.28 µm and thus is located around the first of the double-peak nightside signal. A smaller bandwidth would no longer contain the whole peak [34] resulting in loss of information similar to the choice of the narrow

bandpass when observing the O_2 airglow peak. In addition to the bandpass characteristics, Table 4.5 shows the maximum integration times in relation to the corresponding worst case. The anti-proportionality between bandwidth and maximum integration time is apparent as the photon flux decreases with decreasing bandwidth and therefore more time is required to reach the full well capacity of the detector.

In figure 4.19 it is clearly visible that the SNR performance increases significantly with a narrower bandwidth. With the baseline bandpass and from [43] the SNR requirement is not met in any case. On the other hand, with the narrow bandpass, an SNR of 10 is possible in the best case, which is significantly above the requirement. However, the problem remains that the nominal and worst case values are still very low at $2 \cdot 10^{-1}$ and $9 \cdot 10^{-3}$ respectively, when using the narrow bandpass.

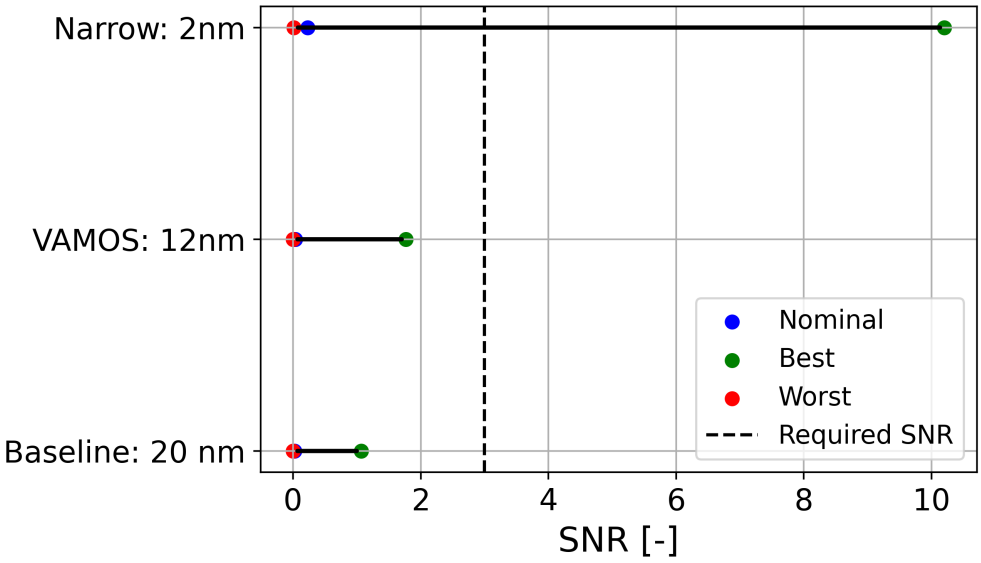

Figure 4.19: SNR performance using the considered bandpasses with the Teledyne H4RG SWIR for observing the nightside in the best, nominal and worst case

The same result can be seen in Fig. 4.20 for the dayside observation with the Teledyne H4RG MWIR as the SNR improves with a narrower bandpass. Again, the baseline bandpass with a wide bandwidth over the double-peak does not meet the minimum SNR requirement in any case, whereas the two narrower bandpasses both exceed an required SNR of 3 in the best case. Nevertheless, the problem of a low SNR of $3 \cdot 10^{-3}$ in the worst case and $1 \cdot 10^{-1}$ nominal case remains, when using the narrow bandpass. It should also be noted that the combination of a narrower bandpass with a higher integration time than previously assumed has a desirable effect on the SNR performance, especially on the nightside.
Although the seismic signal is amplified stronger on the dayside (see 2.8), the SNR performance is more limited as described in the previous section due to the very limited integration time caused by the high background signal. Furthermore, it shall be mentioned that the optical performance is not affected by the selection of the bandpass for both scenarios. Due to the significant improvement of the SNR performance, the narrow bandpass will be assumed in the following for both wavelengths. Although a further narrowing of the bandpass

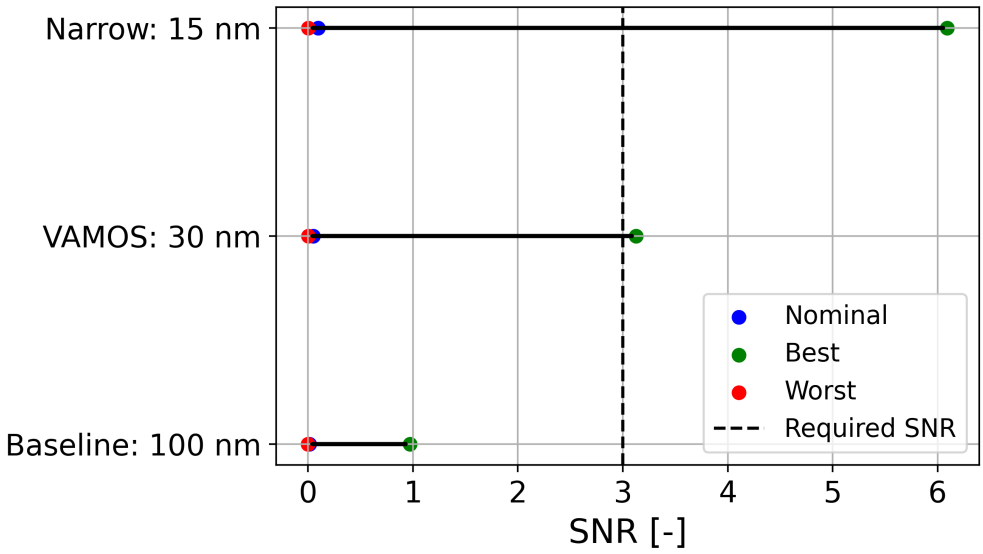

Figure 4.20: SNR performance using the considered bandpasses with the Teledyne H4RG MWIR for observing the dayside in the best, nominal and worst case

would result in a further improvement in SNR, it is not desirable as the spectral resolution of the characteristic signal would no longer be given regarding the spectral radiance curves described in section 2.8.

A possible use of the SCD Cardinal 1280 LG for nightside observation will be ruled out for further consideration, due to higher readout noise and therefore worse SNR performance compared to the medium gain mode version (MG), which still has sufficient full well capacity (see table 4.3). Moreover, the SCD Blackbird 1920 LG will not be considered as a possible detector for dayside observations with the maximum integration time with respect to the full well capacity, due to insufficient SNR performance with respect to the minimum threshold in all considered cases.

4.3 Image Processing: Binning and Stacking

Since the SNR performance is still significantly below the requirements for the worst and nominal case in both scenarios (day- and nightside), image processing methods: binning and stacking, as described in section 2.5, will be used in order to increase the SNR sufficiently in the following.
As examined above, the SNR values for the worst case on the nightside lie between $8 \cdot 10^{-3}$ and $1 \cdot 10^{-2}$ and would therefore need to be increased by a factor of at least 300 in order to reach the required threshold. When using the SCD Cardinal 1280 MG as a detector for observing the nightside, a maximum integration time of 253.5 s and thus 253 stacks at an integration time of 1 s per image is possible with respect to the full well capacity. When observing the smallest waves with a wavelength of 40 km with a corresponding GSD of the detector of 11.818 km it is not possible to increase the SNR by binning, as the Nyquist criterion would

already be violated with a binning factor of 2:

$$b_{max} \leq \frac{\lambda_{Rayleigh}}{2 \cdot GSD} = \frac{40}{2 \cdot 11.818} = 1.69 \tag{4.1}$$

An improvement of the SNR with binning is therefore not possible when aiming the observation of seismic waves with a surface magnitude of $M_S = 5.5$ using the SCD Cardinal 1280 MG.

Using the Teledyne H2RG with a maximum integration time of 12.5 s results in a maximum of 12 stacks with 1s integration time per image and with a GSD of 5.909 km a binning factor of 3 can be achieved without violating the Nyquist-criterion. In total, it is therefore possible to improve the SNR by a factor of $\sqrt{12 \cdot 3} = 6$ resulting in an enhanced SNR value of 0.012 for the smallest waves in the worst case.
On the other hand, 18 stacks with t_{int} =1 s are possible with a maximum integration time of 18s when using the Teledyne H4RG. In addition, a GSD of 2.955 km results in a maximum of 6 pixels, which can be binned with respect to the Nyquist criterion. All in all, this results in an improved SNR of 0.022, which is the highest value compared to the previous values when using the Teledyne H2RG or SCD Cardinal 1280 MG, but is still far below the required value.
Considering the best case for the smallest waves with the lowest possible background of $0.02\,\mathrm{W\mu m^{-1}m^{-2}sr^{-1}}$, it is possible to further increase the number of stacks to 108 with an integration time of 1 s with respect to the full well capacity of the Teledyne H4RG, giving a maximum SNR of 0.125. Therefore, it becomes clear that it is not possible to detect the waves corresponding to a surface magnitude of $M_S = 5.5$ when observing the O_2 airglow at 1.27 µm on the nightside of Venus using the methods discussed in this thesis.

Similarly, the SNR performance is also poor in the worst and nominal case when observing Venus' CO_2 NLTE dayside emission, due to the higher background radiance compared to the nightside. Using the Teledyne H2RG with a maximum exposure time of 0.17 s, it is possible to stack 17 images with an integration time of 0.01 s. Since the GSD and wavelength do not differ from the nightside scenario for this detector, a binning factor of up to 3 is possible in order to fulfill the Nyquist-criterion resulting in a maximum SNR of 0.004 and therefore still not sufficient in the worst case.
Similarly, using the Teledyne H4RG, a maximum of 24 stacks with an integration time of 0.01 s and a binning factor of 6 can increase the SNR further, but not beyond a value of SNR = 0.008. Furthermore, a maximum of 40 stacks with an integration time of 0.01 s and a binning factor of 3 when using the Raytheon Phoenix can achieve a maximum SNR = 0.015 in this case.
Again, this raises the question of whether detecting the smallest waves is possible at all, when observing the dayside. Considering again, a minimal background of $0.02\,\mathrm{W\mu m^{-1}m^{-2}sr^{-1}}$ with a weak seismic signal corresponding to a surface magnitude of $M_S = 5.5$, 6 stacks with 1 s integration time and a binning of 3 can enhance the SNR up to 0.22 when using the Raytheon Phoenix. Therefore, it can be concluded that the detection of Rayleigh waves with a surface magnitude of $M_S = 5.5$ would not be possible at all, either on the nightside or on the dayside, with the methods considered in this thesis and will therefore not be investigated any further in the following.

Considering now the nominal case, the lower background signal compared to the worst case leads to a higher maximum integration time for each detector, which also allows for a higher number of stacks in order to improve the SNR performance. In addition, when considering quakes with a surface magnitude of $M_S = 6.5$ as assumed for the nominal case, this results in a higher seismic wavelength, allowing more binning according to the Nyquist criterion. When using the SCD Cardinal 1280 MG it would therefore be possible to stack up to 434 images with an integration time of 1 s and a maximum binning of 8 pixels:

$$b_{max} \leq \frac{200}{2 \cdot GSD} = 8.46 \tag{4.2}$$

However, this only gives an SNR of 0.63, which is still below the required threshold. By reducing the f-number to 1, the maximum integration time is only 33 s, but the SNR for 33 stacks with 1 s integration time increases to SNR = 0.38 only by using stacking. In order to achieve the required SNR of 3, 26 pixels would have to be binned in this configuration.
However, since the Nyquist criterion for this case allows only a maximum of 8 pixels to be binned, the only option in this case is to reduce the GSD using the same optical design, which means that the FOV can no longer image the full disk of Venus. Therefore, it would be necessary to have a GSD of

$$GSD \leq \frac{200}{2 \cdot 26} = 3.84\,\text{km} \tag{4.3}$$

in order to obtain an SNR = 3 in the nominal case by binning 26 pixels and stacking 33 images with $t_{int} = 1$ s.
With a Teledyne H2RG it is possible to achieve a nominal SNR = 1.09 when stacking up to stacks with an integration time of 1 s per image and a maximum binning factor of 16. However, as the double pixel count of the Teledyne H4RG is accompanied by a double binning factor of 33, an SNR of 1.72 can be achieved using 30 stacks with the same integration time. Reducing the f-number to 2 results in a maximum integration time of 8 s and with 8 stacks (1 s integration time) the SNR would further increase to a value of 1.74, which is still not sufficient with respect to the required threshold.
Consequently, a binning factor of b = 99 would be required in order to achieve the required threshold. According to the Nyquist criterion, this results in a reduction of the GSD to

$$GSD \leq \frac{200}{2 \cdot 99} = 1.01\,\text{km} \tag{4.4}$$

and would also narrow the FOV when using the same optical design.

Finally, Figure 4.21 shows the maximum possible SNR values with varying background radiance for the potential detectors SCD Cardinal 1280 MG and Teledyne H4RG for the observation of the nightside. The Teledyne H2RG will not be further investigated due to better SNR and MTF performance compared to the H4RG.
On the left of figure 4.21, the SNR values of the respective detectors are shown for full disk imaging and improved SNR performance (Zoomed FOV) for a seismic quake of magnitude $M_S = 6.5$. In addition, with respect to the background signal and thus the total number of

photons, the number of stacks was always optimised with respect to the full well capacity. This means that with increasing background emission, the number of stacks decreases and therefore the calculated SNR value.
Since the SNR performance was enhanced based on the nominal case, the SNR values for both detectors pass through the SNR threshold for a background emission of exactly SNR = 3, when using the Zoomed FOV configuration. Furthermore, the SNR curves for the full disk imaging design are significantly lower than the improved curves with a narrow FOV over the entire spectrum. However, the SNR for the SCD Cardinal 1280 MG with full-disk imaging is already below the required threshold at a radiance of $0.03\,\mathrm{W\mu m^{-1}m^{-2}sr^{-1}}$ and the Teledyne H4RG at $0.04\,\mathrm{W\mu m^{-1}m^{-2}sr^{-1}}$. With low background signals, the Teledyne H4RG with enhanced SNR performance (Zoomed FOV) can even achieve SNRs above 10 and therefore well above the threshold. Additionally, the full-spectrum performance is also better with the Teledyne H4RG in both design configurations and is clearly superior when using the SCD Cardinal 1280 MG at lower background emissions. However, at higher background emissions there is little difference in performance between the two detectors, and although the SNR values are below the threshold, the SCD Cardinal 1280 MG performs slightly better at high background levels with improved SNR performance (Zoomed FOV).

When looking at signals from seismic quakes of magnitude $M_S = 7.5$ on the right side of figure 4.21 it can also be clearly seen here that significantly higher SNR values are possible with a smaller FOV but a higher binning factor. Nevertheless, the SNR values are already well above the threshold when using the full disk imaging design (not SNR optimised) and even exceed values of SNR greater than 20 with a maximum background emission of $0.12\,\mathrm{W\mu m^{-1}m^{-2}sr^{-1}}$. Therefore, no further improvement of the SNR by limiting the FOV would be necessary to observe seismic quakes of magnitude $M_S = 7.5$ when observing O_2 airglow on the Venusian nightside.

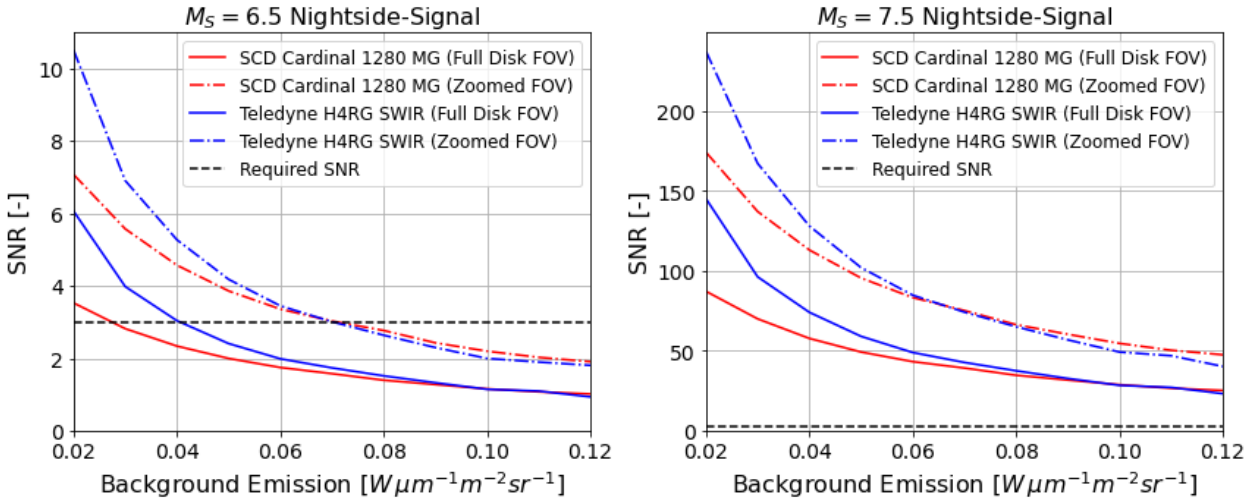

Figure 4.21: Maximum SNR performance of the final imaging system design options when observing the seismic quakes of magnitude $M_S = 6.5$ (left) and $M_S = 7.5$ (right) with optimised stacking over the background emission range on the nightside

Continuing with the observation of the dayside, the use of the Teledyne H2RG with a maximum integration time of 0.34 s thus using 34 image stacks with an integration time of 0.01 s and $b_{max} = 16$ results in a signal-to-noise ratio of 0.46. This can be increased to SNR = 0.78 by using the H4RG with $b_{max} = 33$ and a maximum stack number of 12 at 0.01s integration time and a optimised f-number of 2 for slighlty better SNR performance. Moreover, using the Raytheon Phoenix with the baseline f-number of 4 further increases SNR performance, where a maximum of 82 stacks at 0.01s and a maximum binning factor of 16 can achieve a SNR = 1.36. However, in order to achieve the required SNR for the nominal case, it would be necessary to bin 80 pixels, resulting in a GSD of

$$GSD = \frac{200}{2 \cdot 80} = 1.25\,\mathrm{km} \tag{4.5}$$

Figure 4.22 shows again the maximum possible SNR values with varying background radiance now for the remaining potential detectors Teledyne H4RG and Raytheon Phoenix for the observation of the dayside (Teledyne H2RG MWIR was neglected once againg due to the better performance of the H4RG version). Again, on the left side of the plot the SNR corresponding to the signal of the seismic signal with $M_S = 6.5$ is shown for the full-disk imaging and zoomed FOV imaging sytem design for each detector.
On the one hand, it is clear that using the imaging system with the Teledyne H4RG designed to show the full disk within the FOV hardly allows the seismic signal to be detected above the background signal. Only for weak background radiation below $0.4\,\mathrm{W\mu m^{-1}m^{-2}sr^{-1}}$ the SNR is above the threshold. Although an improvement in the SNR performance of the Teledyne H4RG can be seen by reducing the GSD and thus increasing the maximum possible binning factor, the SNR is still not sufficient over the majority of the background radiance range (blue-dotted curve). It should be noted that in this case the improved design in terms of SNR was adopted from the nightside design if the detector could be used with the appropriate quantum efficiency to observe both sides.
In comparison, it can be seen that using the Raytheon Phoenix with full disk imaging has an almost identical performance compared to the Teledyne H4RG with enhanced SNR performance (Zoomed FOV), which is due to the fact that the SNR is improved by binning and stacking with a factor of to a similar extent as when using for the Teledyne H4RG.
However, the SNR performance of the Raytheon Phoenix with an optimised design for a better SNR performance is clearly superior to the others (Fig. 4.22 (left)). With minimal background signal, SNR values of over 20 can be achieved, while with maximum background noise, a SNR = 1.5 can still be achieved and has good potential for further enhancement by the factor of two in order to reach the threshold with other image processing methods for example.

Regarding the SNR of seismic signals caused by earthquakes of magnitude $M_S = 7.5$ on the right hand side, it can be said that the performance over the whole background spectrum at 4.3 µm when obsvering the Venusian dayside is sufficiently high with all the remaining detectors and imaging system options. Even at the maximum background signal of $0.30\,\mathrm{W\mu m^{-1}m^{-2}sr^{-1}}$, the SNR is at least 10 with the Teledyne H4RG (Full-disk imaging), leaving plenty of room for possible detection at the highest background radiance.

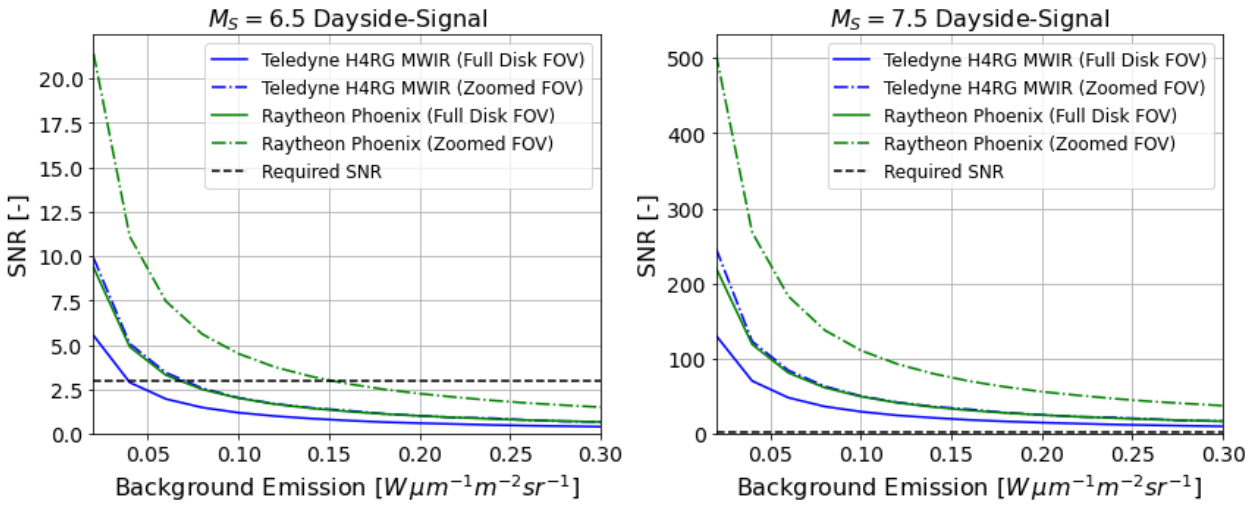

Figure 4.22: Maximum SNR performance of the final imaging system design options when observing the seismic quakes of magnitude $M_S = 6.5$ (left) and $M_S = 7.5$ (right) with optimised stacking over the background emission range on the dayside

4.4 Orbit Altitude and Optics

In this final step, the orbit altitude shall be determined based on the full disk imaging condition discussed in section 3.5. The focal length and thus the orbit altitude shall be chosen to ensure that the imaging system fits into a 1U Cubesat with respect to MC01.
Figure 4.23 shows the relationship between focal length and orbit altitude from equation 3.4 for the remaining detectors. If the equation is now rearranged according to the orbit altitude, it can be seen that for full disk imaging the focal length, and thus the payload size, increases continuously with increasing orbit altitude, as shown in figure 4.23. Due to its high resolution, the Teledyne H4RG requires the largest payload size at the same orbit altitude compared to the other detectors. On the other hand, using a SCD Cardinal 1290 MG results in a much higher orbit altitude with full disk imaging, because of the lower dimensions of the detector. As the imaging system also needs a housing, which takes up additional space, the focal length is chosen with a margin of 20% with respect to the maximum length of 100 mm (1U CubeSat). In addition, the focal length should not be smaller than this to prevent a degradation of the optical performance in terms of MTF performance, because a smaller focal length results in a lower orbit altitude thus increasing motion blur.
Consequently, for a focal length of 80 mm, using the SCD Cardinal 1280 MG results in an increase in orbital altitude to 94 546 km. This also results in an iFOV of 0.125 mrad and over the required GSD this leads to an orbit altitude of 30 400 km using equation 2.29 for the SNR enhanced imaging system. In addition, the product of the GSD and the number of pixels leads to a FOV area of 4864 × 3891 km and would correspond to a coverage of 72.3% of the entire Venusian disk.
Using the Teledyne H4RG with the same focal length the orbit altitude decreases to 15 757 km compared to the default altitude. Morever, an iFOV of 0.1875 mrad and a required GSD of 1 ^{k}m leads to a further reduction of the orbit to 5333 km with a coverage of 4096 × 4096 km,

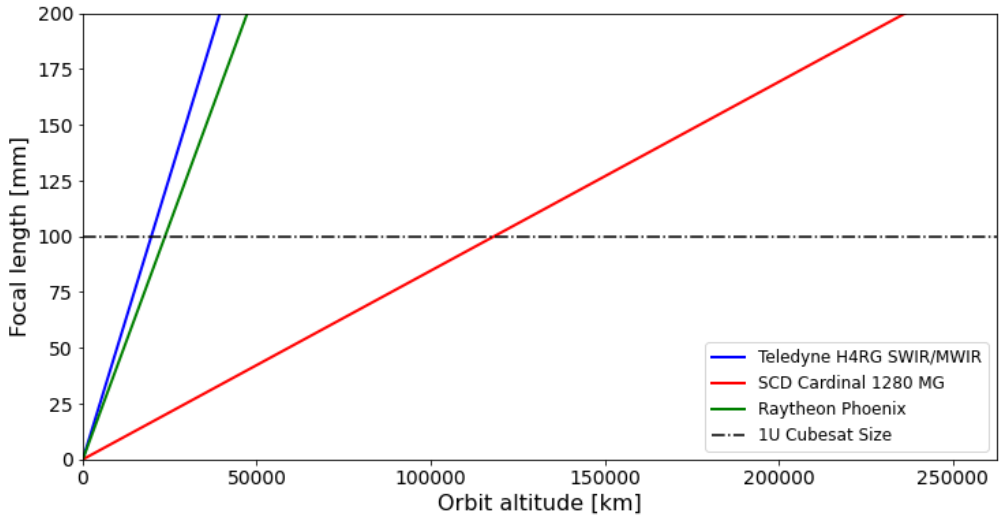

Figure 4.23: Focal length over orbit altitude for full-disk imaging of Venus with the remaining detectors

which represents 67.7% of the Venusian disk.
When observing Venus with the Raytheon Phoenix with a focal length of 80 mm, it results in a slightly higher orbit at 18 909 km compared to the Teledyne H4RG. For the required GSD of 1.25 km an orbit altitude of exactly 4000 km is required using the same imaging system for better SNR performance and ultimately resulting in a coverage of 2560 × 2560 km.

With the selected focal length and therefore the different orbits along with the chosen f-numbers for each design the final optical performance regarding the optical performance is determined and shown in figure 4.24. For each design option the MTF performance is given

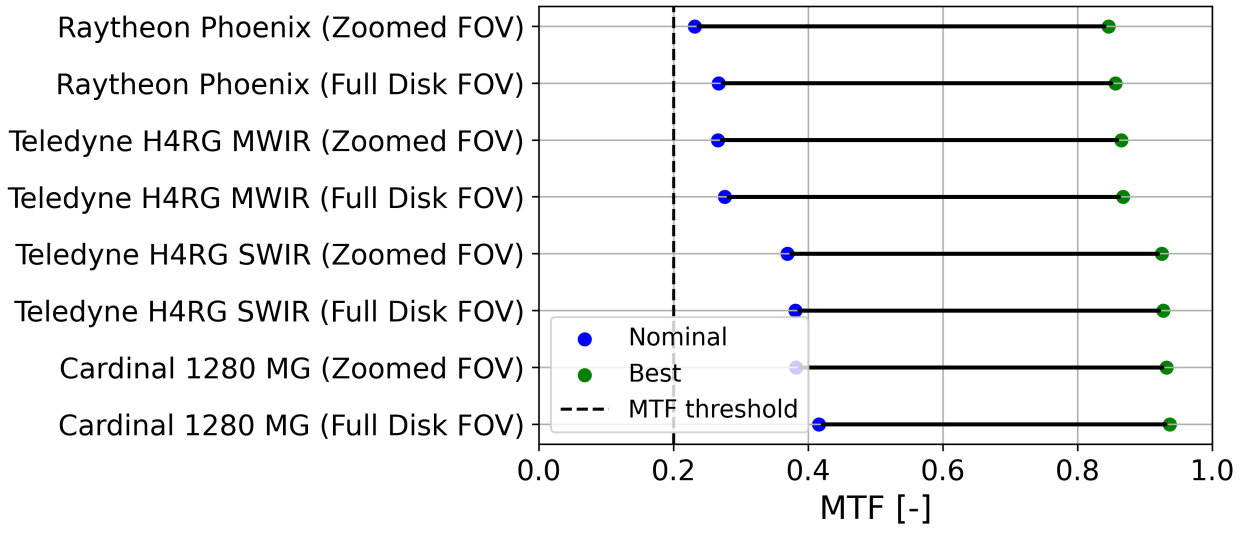

Figure 4.24: MTF performance at the corresponding spatial frequency MTF($\xi_{Rayleigh}$) for best and nominal case

at the corresponding spatial frequency MTF($\xi_{Rayleigh}$) for the seismic waves corresponding to a magnitude of $M_S = 6.5$ (nominal) and $M_S = 7.5$ (best). In comparison to the previous analysis of the MTF performance (Fig. 4.2 and 4.11) it has noticeably reduced, since binning was used in order to maximise the SNR performance. However, the MTF performance is still sufficiently above the required minimum of 0.2 for all potential designs in order to reach maximum SNR performance. Also note, that the MTF values for the best case correspond to unchanged binning and stacking factors as used for maximising the SNR performance in the nominal case and therefore well above 0.8. However, if the binning and stacking factor would have been maximised for the best case as well, the MTF performance would be comparable to the nominal case, as with a higher wavelength less GSD and therefore higher binning factor and through a lower background more integration time thus higher stacking would be possible. This is not required as the SNR performance is far above the required threshold for seismic magnitudes of $M_S = 7.5$. Lastly, it can be said that for the selected orbit altitudes due to the imaging system design the orbit is still high enough and therefore motion blur trough pixel smear has not sufficient impact on the optical performance of the designs. All MTF curves for each design option based on the remaining detectors are given in appendix B.

5 Preliminary Design Options

With the final determination of the orbit altitude and therefore size of the imaging system, all parameters of the imaging system are now set as a preliminary design for the detection of seismic Rayleigh waves in the atmosphere of Venus. In the following, all options for observing the day- and nightside of Venus are explained and a final recommendation for a preliminary design of the imaging system is presented.

5.1 Observation of Venus' Nightside

For the O_2 airglow observation on the nightside, two designs with two settings each were determined based on the Teledyne H4RG SWIR detector and the SemiConductor Devices Cardinal 1280 in medium gain mode. For all design options, a focal length of 80 mm was chosen in order to fit into a 1U Cubesat with the best possible performance, taking a payload housing into account. For the established f-numbers in order to maximise SNR performance, this results in an aperture diameter of 40 mm when using the Teledyne H4RG ($f/\# = 2$) and 80 mm for the SCD Cardinal 1280 MG ($f/\# = 1$). In addition, the Teledyne H4RG has a larger FOV and iFOV than the Cardinal 1280 due to the slightly larger pixel size and higher pixel number. Moreover, based on the significantly lower GSD, the orbit altitude is significantly lower for both settings when using the Teledyne H4RG. The limited FOV design for achieving better SNR performance results in similarly high coverage areas for both detectors when observing the Venusian nightside. A narrow bandpass with a bandwidth of $\Delta\lambda = 2$ nm was determined for measuring at 1.27 µm in order to achieve high SNR without losing information in terms of spectral resolution. An integration time of 1 s has been selected with respect to the full well capacity and stacking capability in order to improve SNR performance. At the bottom of the table the binning and stacking factor are referenced for the use in the nominal case and are especially important for the enhanced designs with a narrow FOV. As the SNR performance is far above the threshold, there was no need to further optimise for the waves corresponding to higher magnitudes (best case). Finally, the SNR values for the nominal case are given based on the respective binning and stacking factors for each design option. As already shown in figure 4.21, the SNR can be improved to the required threshold by reducing the FOV as explained in section 4.3. All final set and selected parameters of the preliminary design options for observing the nightside are summarised in Table 5.1.

Lastly, a final analysis of the performance of the imaging system using the Teledyne H4RG SWIR exemplary for nightside observation and H4RG MWIR exemplary for the dayside, both in the full disk imaging option, is presented below.

Table 5.1: Preliminary imaging system design parameters for the O_2 nightside airglow observation of Venus

Parameter	**Teledyne H4RG**		**SCD Cardinal 1280 MG**		Unit
	Full-Disk FOV	Zoomed FOV	Full-Disk FOV	Zoomed FOV	
f	80				mm
$f\#$	2		1		-
D	40		80		-
FOV	42.02 × 42.02		9.15 × 7.32		deg
$iFOV$	0.1875		0.1250		mrad
GSD	2.955	1	11.818	3.8	km
h	15757	5333	94546	30400	km
FOV Range	12102×12102	8192×8192	12102×12102	9728×7782	km
Venus Coverage	100	67.7	100	72.3	%
$\Delta\lambda$	2				nm
t_{int}	1				s
T	80		213-202		K
$b_{nominal}$	33	99	8	26	-
$s_{nominal}$	8		33		-
$SNR_{nominal}$	1.74	3.01	1.58	3.03	-

First of all, the profile of the MTF_{total} and its components can be seen in figure 5.1. Compared to the baseline design using the XenicsXSW640 as an example (Fig. 4.5 and 4.3), there are hardly any differences at first sight. Although the orbit altitude has been reduced from 45000 to 15757 km, the influence of MTF_{blur} is still negligible. MTF_{blur} also remains unchanged at the lower orbital altitudes of 5333 km for SNR improvement with the Teledyne H4RG (Fig. B.3) or even further to 4000 km with the use of the Raytheon Phoenix (Fig. B.6).
As already shown in figure 4.5 in the case of an observation at 1.27 µm, the overlapping curves of MTF_{pixel} and $MTF_{sampling}$ are the dominant components compared to MTF_{lens}, which lead to a reduction of the total MTF with increasing spatial frequencies. At second glance, it is noticeable that the cut-off frequency ξ_C is significantly lower than in the baseline design, so that lower spatial frequencies are significantly more affected in this design. This is mainly due to the high GSD caused by the binning applied and the halving of the f-number in order to improve the SNR performance sufficiently. However, this does not affect the MTF performance in a critical way, as can be seen from the fact that $\xi_{Rayleigh}$ is still ahead of $\xi_{Nyquist}$ therefore meeting the Nyquist criterion. In addition, the MTF threshold is even further behind, thus the MTF threshold of 0.2 is also met for wavelengths of 200 km and therefore also for larger wavelengths. The MTF curves for the other three design options (Fig. B.1, B.2 and B.3) from Table 5.1 are almost identical for the observation of the nightside, hence the previous interpretation applies to them as well. Only in the case of the designs optimised for SNR performance with limited FOV, the spatial frequencies $\xi_{Rayleigh}$ and $\xi_{Nyquist}$ are almost

superimposed, since the binning was optimised with respect to the Nyquist criterion.

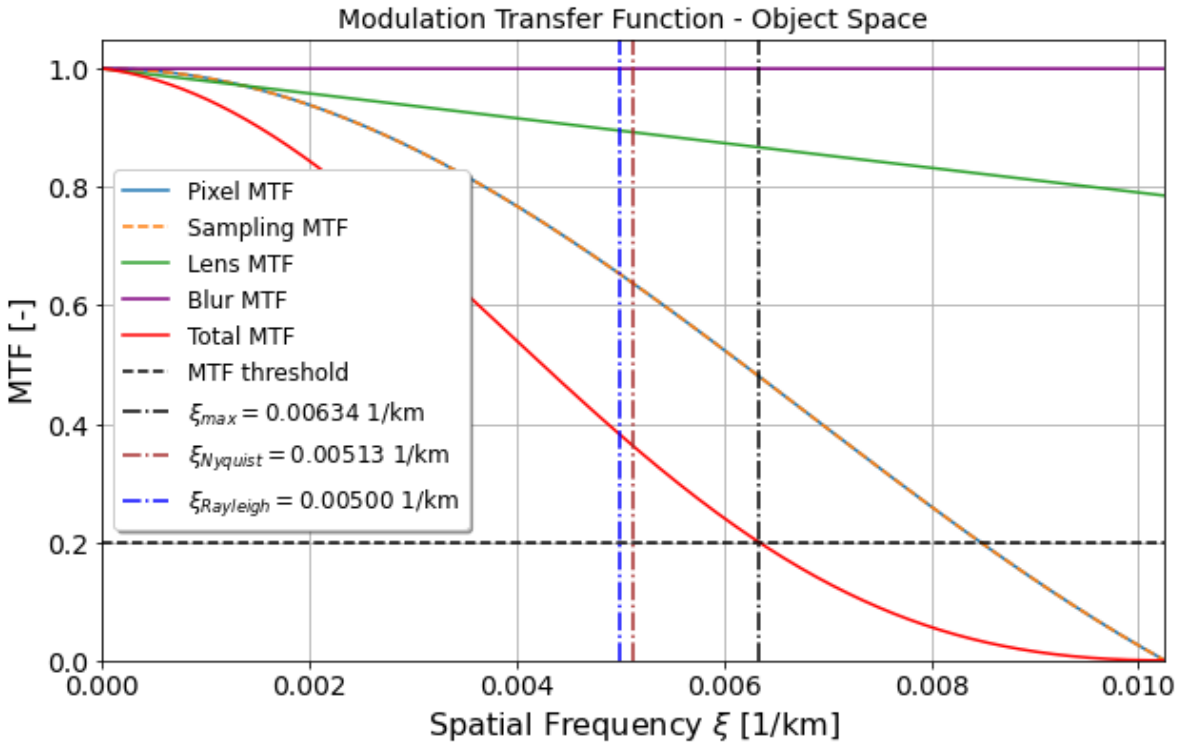

Figure 5.1: MTF as a function of the spatial frequency in object space for the imaging system with the Teledyne H4RG SWIR detector (Full disk FOV) for the nominal case

Examining the simulated images with and without the application of the MTF in 2D with the full-disk imaging design, no waves can be seen in front of the background signal on the nightside of Venus as shown in figure 5.2. The same applies to all full disk imaging system designs in the nominal case, for both the day- and the nightside (see Fig. 5.4, C.1 and C.5).

However, looking at figure 5.2 the contrast pattern between the peaks and dips of the waves is better recognisable, whereas when using the SCD Cardinal 1280 MG in the full-disk imaging design they are clearly less recognisable (Fig. C.1).
Furthermore, figure 5.2 shows the resolution performance when using the Teledyne H4RG in the full-disk imaging design. Here it is clear that the Nyquist criterion is still met with a maximum binning of 33, as two pixels ($2 \cdot 95$ km) sufficiently resolve the distance of one wavelength ($\lambda = 200$ km) in this case. However, the contrast decreases when applying the MTF and it becomes almost impossible to distinguish the wave signal from the background even with an SNR = 1.74 in this case. However, this is counteracted by using the SNR-optimised design with SNR = 3 in the nominal case.

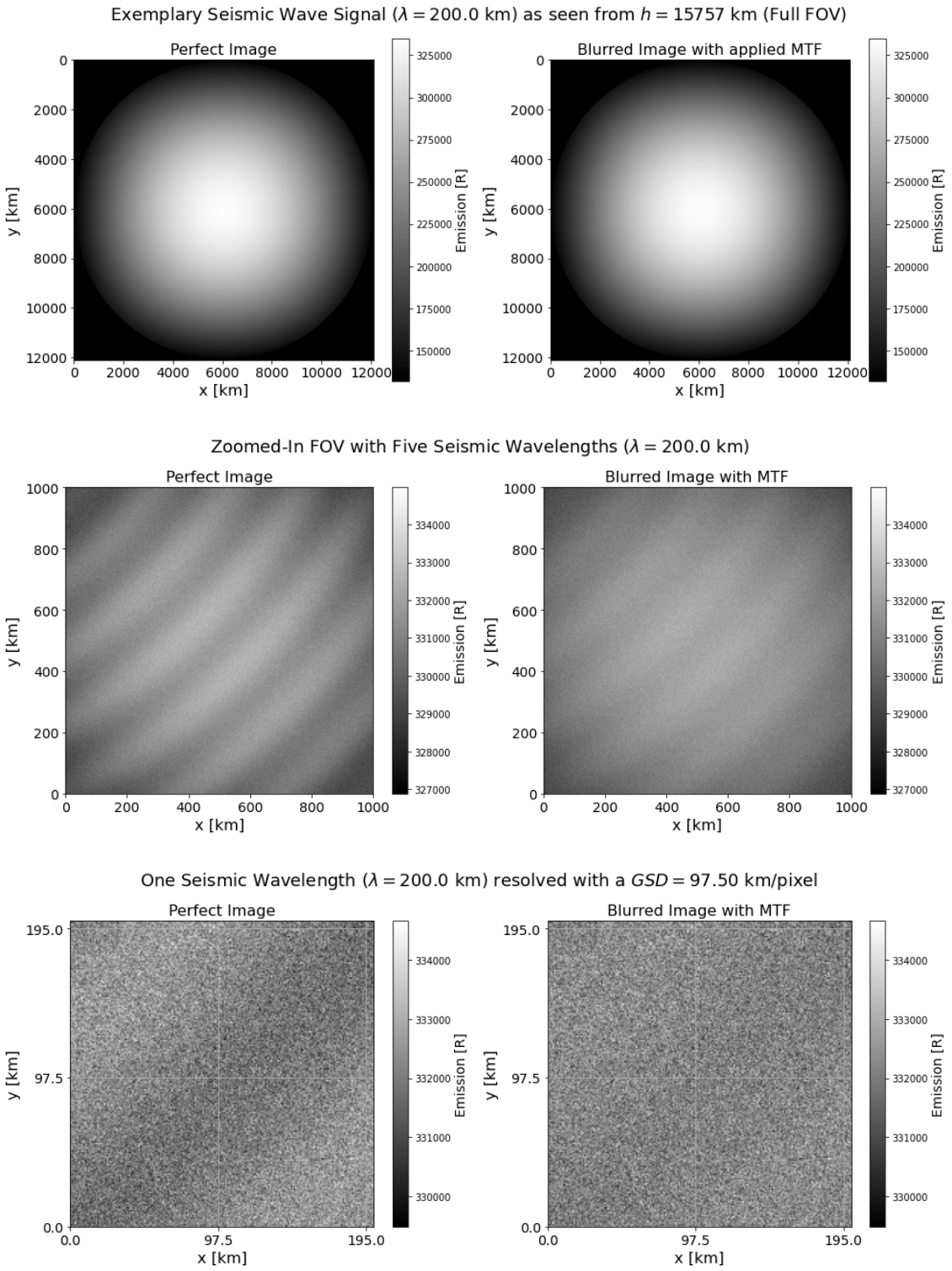

Figure 5.2: Contrast comparison for perfect (MTF = 1) and blurred image (applied MTF) with the expected emission in Rayleigh with Venus' full disk in the FOV (top), for a 5 × 200 × 200 km FOV cut-out (center) and for a 200 × 200 km FOV cut-out (bottom) for a background signal with $L_{\lambda_{peak}} = 0.07$ Wm^{-2}µm^{-1}sr^{-1} at 1.27 µm and a surface magnitude of $M_S = 6.5$ (nominal case) resulting in SNR = 1.74 using the Teledyne H4RG SWIR

5.2 Observation of Venus' Dayside

For the scenario of detecting seismic waves on the dayside by observing the CO_2 NLTE emission, two designs for the imaging system have been developed, each with two settings as well. The parameters when using the Teledyne H4RG MWIR have been chosen identically in case it would be feasible to use the detector for both day and night side observations with a corresponding adjustment of the quantum efficiency with respect to the observed bandwidths. The integration times are much shorter in comparison to the nightside observation in order to allow stacking with respect to the full well capacity and is due to the high background radiance on the dayside. Again, the focal length is set to 80 mm for the same reasons as in the previous scenario. The higher f-number reduces the aperture diameter to 20 mm in the case of using the Raytheon Phoenix and remains the same when using the Teledyne H4RG with $f/\# = 2$. The number of pixels is only half that of the Teledyne H4RG, resulting in a smaller FOV and iFOV when using the Raytheon Phoenix, which ultimately leads to an orbital altitude of 4000 km in the case of the adapted design with limited FOV in order to enhance SNR perofrmance. However, since the GSD is similar to that of the Teledyne H4RG in the adapted cases (Zoomed FOV), the Raytheon Phoenix has a coverage of less than 50% of the Venusian disk. Furthermore, a bandwidth $\Delta\lambda$ of 15 nm with a CWL at 4.28 µm has been determined in order to enhance SNR performance without losing information of the first peak of the double-peak background signature at 4.3 µm. All parameters for the imaging system design options for the dayside are summarised in Table 5.2.

Table 5.2: Preliminary imaging system design parameters for the CO_2 dayside NLTE emission observation of Venus

Parameter	**Teledyne H4RG**		**Raytheon Phoenix**		Unit
	Full-Disk FOV	Zoomed FOV	Full-Disk FOV	Zoomed FOV	
f	80				mm
$f\#$	2		4		-
D	40		20		-
FOV	42.02 × 42.02		35.49 × 35.49		deg
$iFOV$	0.1875		0.3125		mrad
GSD	2.955	1	5.909	1.25	km
h	15757	5333	18909	4000	km
FOV Range	12102×12102	8192×8192	12102×12102	5120×5120	km
Venus Coverage	100	67.7	100	42.3	%
$\Delta\lambda$	15				nm
t_{int}	0.01				s
T	37		30		K
$b_{nominal}$	33	99	16	80	-
$s_{nominal}$	12		82		-
$SNR_{nominal}$	0.93	1.57	1.57	3.04	-

Comparing the curve of the total MTF and its components when observing the dayside with the Teledyne H4RG MWIR in the full disk imaging design at 4.3 µm, many similarities as with the baseline design in Figure 4.14 remain.
Due to the same orbital altitude and the shorter integration time, the influence of MTF_{blur} is still negligible. However, the influence of MTF_{lens} increases with increasing wavelength. MTF_{pixel} and $MTF_{sampling}$ remain the same due to the same design of the imaging system (see Table 5.1 and 5.2) resulting in a stronger decrease of MTF_{total} with increasing spatial frequencies compared to the 1.27 µm observation, which was already the case for the baseline design (see Fig. 4.14). Both the MTF threshold and the Nyquist criterion are met here, because: $\xi_{Rayleigh} < \xi_{Nyquist} < \xi_{MTF_{threshold}}$.

The MTF curves for the other three design options (see Fig. B.4, B.5 and B.6) from Table 5.2 are almost identical for the observation of the dayside, and the previous interpretation applies to them as well. Again, only in the case of the designs optimised regarding the SNR performance with limited FOV the spatial frequencies at $\xi_{Rayleigh}$ and $\xi_{Nyquist}$ are almost superimposed. As already mentioned, in the nominal case without the SNR improved design,

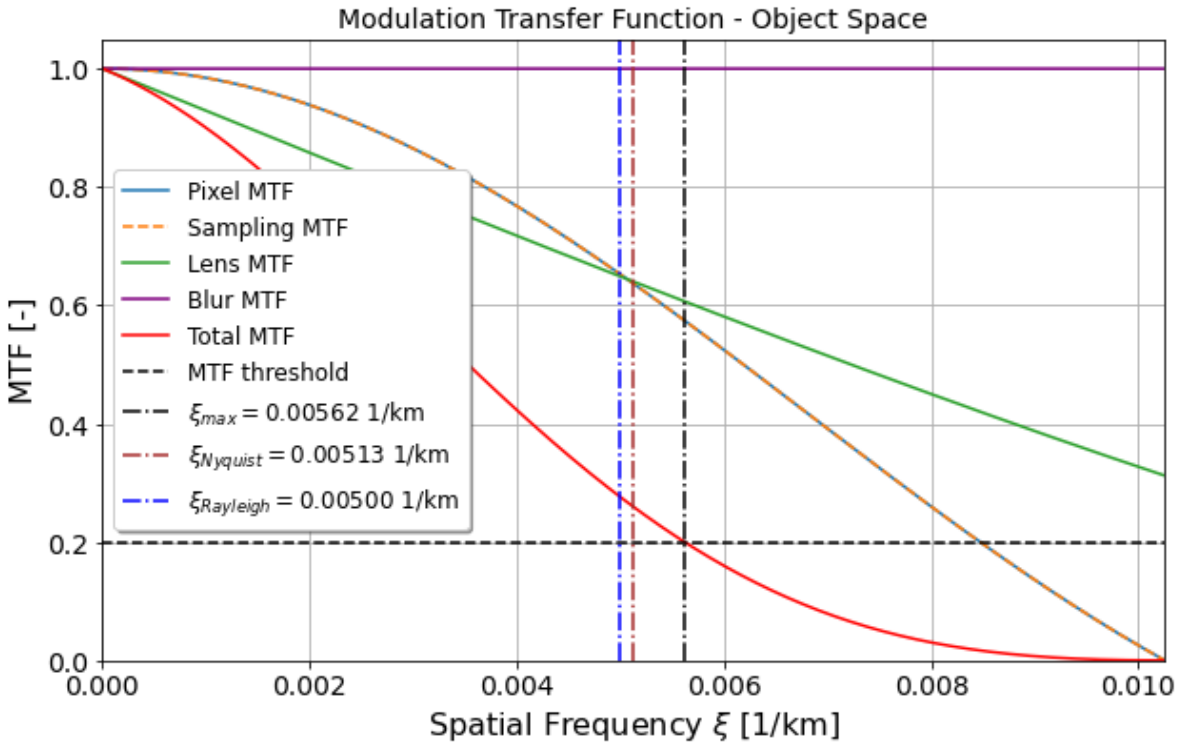

Figure 5.3: MTF as a function of the spatial frequency in object space for the imaging system with the Teledyne H4RG MWIR detector (Full disk FOV) for the nominal case

no contrast pattern of the waves is present when looking at Venus within the full FOV shown in figure 5.4, and is also the case for the full disk imaging design when using the Raytheon Phoenix (Fig. C.5). Looking at the cut-out shown in figure 5.4, peaks and dips of the waves can be distinguished (left). However, when applying the corresponding MTF, the contrast diminishes to such an extent that it is almost impossible to distinguish between them any-

more (right).
Finally, figure 5.4 shows the cut-out FOV demonstrating the spatial resolution. Compared to Fig. 5.2, it is noticeable that the signal on the dayside is much stronger, but after applying the MTF, the waves are less discernible and hardly distinguishable. When now using the Raytheon Phoenix instead, the performance is slightly better, but the choice of the SNR-improved design is essential in the nominal case for detection on the dayside as well.

By looking at the seismic signal corresponding to $M_S = 7.5$, the potential for detecting seismic Rayleigh waves in the Venusian atmosphere becomes very clear. Either in the full FOV (Fig. C.2, C.3, C.4 and C.6 (top)) down to resolving the distance of a wavelength at the pixel level (Fig. C.2, C.3, C.4, C.6 (center)), peaks and dips are clearly distinguishable, and this ultimately applies to both the day and night sides, regardless of the design (see also Fig. C.2, C.3, C.4, C.6 (bottom)).

Ultimately, the Raytheon Phoenix is recommended as the detector for the infrared imaging system and therefore all resulting parameters of the payload system. Its adequate SNR and MTF performance, along with the ability to observe both the O_2 nightside airglow at 1.27 µm and the CO_2 dayside NLTE emission at 4.3 µm, offer the most promising potential for the detection of atmospheric-coupled waves in the Venusian atmosphere. Nevertheless, the imaging system based on the Teledyne H4RG provides a strong back-up for observing both the day- and nightside and should not be ruled out entirely without further investigations.

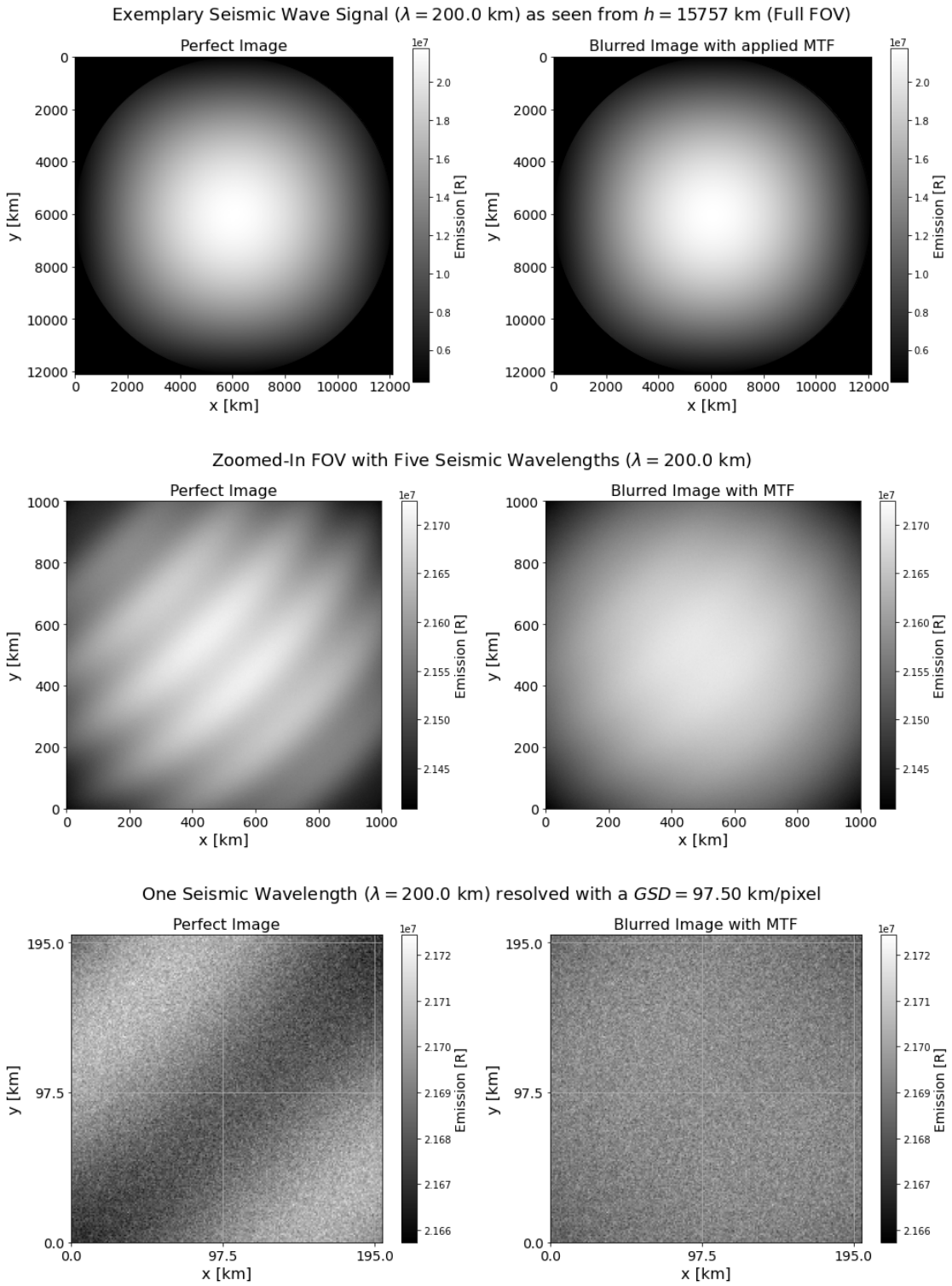

Figure 5.4: Contrast comparison for perfect (MTF = 1) and blurred image (applied MTF) with the expected emission in Rayleigh with Venus' full disk in the FOV (top), for a 5 × 200 × 200 km FOV cut-out (center) and for a 200 × 200 km FOV cut-out (bottom) for a background signal with $L_{\lambda_{peak}} = 0.15$ Wm^{-2}µm^{-1}sr^{-1} at 4.28 µm and a surface magnitude of $M_S = 6.5$ (nominal case) resulting in SNR = 0.93 using the Teledyne H4RG MWIR

6 Conclusion

In this study, the primary objective was to derive an initial instrument concept for the design of an infrared camera for application on a small satellite mission to Venus. The aim is to detect seismic Rayleigh waves within the Venusian atmosphere, ultimately providing valuable insights into the planet's interior structure.
Based on the fundamentals of radiometry, optics, infrared detectors, remote sensing, image processing and planetary research for Venus, a definition of the mission and instrument design has been established, providing the baseline for trade-off analysis and evaluation in this thesis to ultimately derive an instrument design fulfilling the mission objective.

The results of this research provided information on the feasibility and limitations of detecting seismic waves on Venus using remote sensing infrared imaging instrumentation. Through careful analysis of assumed emissions of atmospheric-coupled Rayleigh waves and background signals on both the night- and dayside of Venus, it became evident that certain surface magnitudes of seismic activity with certain background noise levels pose challenges for detection due to insufficient signal-to-noise ratio performance.

Nevertheless, the study showed promising results, with seismic waves corresponding to surface magnitudes of $M_S = 6.5$ and $M_S = 7.5$ being detectable with appropriate imaging system configurations. Trade-off analyses based on the identified system drivers led to the identification of two preliminary designs based on suitable infrared detectors for each side, each with two options, one focusing on full disk imaging and the other one on a narrower field-of-view with improved signal-to-noise ratio performance.

Following an extensive evaluation, the imaging system design based on the use of the Raytheon Phoenix detector emerged as the recommended approach to effectively achieve the mission objectives, with the required detectivity and spatial resolution performance being essential to meet the mission requirements and constraints, as well as having the potential to observe and detect seismic waves on both sides, thus offering a higher probability of detection.

In essence, this thesis not only advances the understanding of the challenges of detecting seismic activity in the Venusian atmosphere using space-based remote sensing, but also provides a feasible approach to the realisation of this ambitious small satellite mission. By demonstrating the feasibility of deriving an instrument concept capable of achieving the mission objectives, this thesis provides a solid foundation for the upcoming work and investigations for this mission.

7 Outlook

The process towards the design of an instrument to detect seismic Rayleigh waves in the Venusian atmosphere is a key element in the exploration of the interior of Venus. Several critical issues for further refinement and investigation emerge when moving from the conclusions of the preliminary design to the upcoming stages of the mission and instrumentation design.

As a first step, further simulations of the atmospheric-coupled Rayleigh waves at both wavelengths should be conducted in order to increase the insight into the detection capabilities. A pivotal aspect to be further investigated is the comparative effectiveness between employing a full-disk imaging approach or utilizing a narrower FOV with improved SNR performance based on precise models and simulations of observed dynamics in the Venusian atmosphere. Advanced analysis and simulation will help to determine which observing strategy offers the best chance of detection. Another aspect that can be further optimised is the optimisation of the orbit altitude with regard to more stacking in order to increase the SNR while taking the motion blur into account.

Furthermore, investigating the feasibility of observing both wavelengths simultaneously represents a significant advancement in the instrument design. In parallel, mechanical and thermal design aspects of the payload system have to be addressed to ensure robustness and resilience in the severe environment of space around Venus. Accommodation as a rideshare presents unique challenges that require careful planning and optimisation to maximise payload utilisation and minimise interference with other on-board systems.

In addition, the development of detection algorithms and on-board data handling protocols will be crucial for extracting useful scientific data from the observations, while efficient data handling procedures will facilitate real-time processing and transmission of data back to Earth.

Careful consideration must also be given to the design and strategy for the deployment, maintenance and pointing stability with respect to the science orbit. Precision in orbital parameters and attitude control mechanisms is essential to ensure optimal positioning for data acquisition and to mitigate challenges when observing the Venusian atmosphere from the satellite.

References

[1] ASTM. 2000 astm standard extraterrestrial spectrum reference e-490-00, 2019. Last access on 28.01.2024.

[2] Mario Bačić, Lovorka Librić, Danijela Jurić Kaćunić, and Meho Saša Kovačević. The usefulness of seismic surveys for geotechnical engineering in karst: some practical examples. *Geosciences*, 10(10):406, 2020.

[3] Doran J Baker. Rayleigh, the unit for light radiance. *Applied Optics*, 13(9):2160–2163, 1974.

[4] Eric Beuville, David Acton, Elizabeth Corrales, John Drab, Alan Levy, Michael Merrill, Richard Peralta, and William Ritchie. High performance large infrared and visible astronomy arrays for low background applications: instruments performance data and future developments at raytheon. In *Infrared Systems and Photoelectronic Technology II*, volume 6660, pages 72–81. SPIE, 2007.

[5] Glenn D Boreman. *Modulation transfer function in optical and electro-optical systems*. SPIE press Bellingham, Washington, 2021.

[6] D Crisp, VS Meadows, B Bézard, C De Bergh, J-P Maillard, and FP Mills. Ground-based near-infrared observations of the venus nightside: 1.27-μm o_2 ($a^1\delta_g$) airglow from the upper atmosphere. *Journal of Geophysical Research: Planets*, 101(E2):4577–4593, 1996.

[7] Edmund Optics. Optical filters. `https://www.edmundoptics.com/knowledge-center/application-notes/optics/optical-filters/`, 2024. Last access on: 06.02.2024.

[8] EdmundOptics. Infrared bandpass filters, 2024. Last access on: 14.02.2024.

[9] EdmundOptics. Optical bandpass filters, 2024. Last access on: 14.02.2024.

[10] Thomas J. Fellers, Kimberly M. Vogt, and Michael W. Davidson. CCD Signal to Noise Ratio. `https://www.microscopyu.com/tutorials/ccd-signal-to-noise-ratio`, 2023. National High Magnetic Field Laboratory, 1800 East Paul Dirac Dr., The Florida State University, Tallahassee, Florida, 32310.

[11] Robert D Fiete. *Modeling the imaging chain of digital cameras*. SPIE press Bellingham, Washington, 2010.

[12] Raphaël Garcia, Philippe Lognonné, and Xavier Bonnin. Detecting atmospheric perturbations produced by venus quakes. *Geophysical Research Letters*, 32(16), 2005.

[13] RF Garcia, Pierre Drossart, Giuseppe Piccioni, M López-Valverde, and G Occhipinti. Gravity waves in the upper atmosphere of venus revealed by co2 nonlocal thermodynamic equilibrium emissions. *Journal of Geophysical Research: Planets*, 114(E5), 2009.

[14] J-C Gérard, Lauriane Soret, Alessandra Migliorini, and Giuseppe Piccioni. Oxygen nightglow emissions of venus: Vertical distribution and collisional quenching. *Icarus*, 223(1):602–608, 2013.

[15] G Gershon, E Avnon, M Brumer, W Freiman, Y Karni, T Niderman, O Ofer, T Rosenstock, D Seref, N Shiloah, et al. 10um pitch family of insb and xbn detectors for mwir imaging. In *Infrared Technology and Applications XLIII*, volume 10177, pages 334–349. SPIE, 2017.

[16] Richard Ghail et al. Envision assessment study report. Technical report, European Space Agency (ESA), February 2021.

[17] Joern Helbert, Martin Pertenaïs, Ingo Walter, Gisbert Peter, Thomas Säuberlich, Andrei Cacovean, Alessandro Maturilli, Giulia Alemanno, B Zender, C Arcos Carrasco, et al. The venus emissivity mapper: implementation for flight on the nasa veritas mission. In *Infrared Remote Sensing and Instrumentation XXX*, volume 12233, pages 13–23. SPIE, 2022.

[18] DM Hunten, FE Roach, and JW Chamberlain. A photometric unit for the airglow and aurora. *Journal of Atmospheric and terrestrial Physics*, 8(6):345–346, 1956.

[19] Ibsen Photonics. Noise in detectors. `https://ibsen.com/resources/detector-resources/noise-in-detectors/`, 2021.

[20] Naomoto Iwagami, Seiko Takagi, Shoko Ohtsuki, Munetaka Ueno, Kazunori Uemizu, Takehiko Satoh, Takeshi Sakanoi, and George L Hashimoto. Science requirements and description of the 1 μm camera onboard the akatsuki venus orbiter. *Earth, planets and space*, 63(6):487–492, 2011.

[21] Takahiro Iwata, Kohei Kitazato, Masanao Abe, Makiko Ohtake, Takehiko Arai, Tomoko Arai, Naru Hirata, Takahiro Hiroi, Chikatoshi Honda, Naoya Imae, et al. Nirs3: the near infrared spectrometer on hayabusa2. *Space Science Reviews*, 208:317–337, 2017.

[22] B Kenda, P Lognonné, A Komjathy, B Banerdt, J Cutts, B Sutin, A Didion, and J Jackson. Modeling airglow disturbances induced by quakes on venus: Perspectives for future observations. In *49th Annual Lunar and Planetary Science Conference*, page 2393, 2018.

[23] A Komjathy, A Didion, B Sutin, B Nakazono, A Karp, M Wallace, G Lantonie, S Krishnamoorthy, M Rud, J Cutts, et al. Remote sensing of seismic activity on venus using a small spacecraft: initial modeling results. In *49th Annual Lunar and Planetary Science Conference*, page 1731, 2018.

[24] Vladimir A Krasnopolsky. Venus night airglow: Ground-based detection of oh, observations of o2 emissions, and photochemical model. *Icarus*, 207(1):17–27, 2010.

[25] Vladimir A Krasnopolsky. Excitation of the oxygen nightglow on the terrestrial planets. *Planetary and Space Science*, 59(8):754–766, 2011.

[26] Sanjay S Limaye, Davide Grassi, Arnaud Mahieux, Alessandra Migliorini, Silvia Tellmann, and Dmitrij Titov. Venus atmospheric thermal structure and radiative balance. *Space Science Reviews*, 214:1–71, 2018.

[27] P Lognonné, CL Johnson, and G Schubert. 10.03—planetary seismology. *Treatise on geophysics*, 2:65–120, 2015.

[28] Philippe Lognonné and Catherine Johnson. Planetary seismology. *Treatise on Geophysics*, 10:69–122, 2007.

[29] Philippe Lognonné, Foivos Karakostas, Lucie Rolland, and Yasuhiro Nishikawa. Modeling of atmospheric-coupled rayleigh waves on planets with atmosphere: From earth observation to mars and venus perspectives. *The Journal of the Acoustical Society of America*, 140(2):1447–1468, 2016.

[30] Andrea Longobardo, Ernesto Palomba, Angelo Zinzi, Giuseppe Piccioni, Constantine CC Tsang, and Pierre Drossart. Limb darkening study using venus nightside infrared spectra from virtis-venus express data. *Planetary and Space Science*, 69(1):62–75, 2012.

[31] Ernst Messerschmid and Stefanos Fasoulas. *Raumfahrtsysteme*, volume 2. Springer, 2011.

[32] M Nakamura, T Imamura, N Ishii, T Abe, T Satoh, M Suzuki, M Ueno, A Yamazaki, N Iwagami, S Watanabe, et al. Overview of venus orbiter, akatsuki. *Earth, planets and space*, 63(5):443–457, 2011.

[33] Giovanni Occhipinti, Florent Aden-Antoniow, Aurélien Bablet, Jean-Philippe Molinie, and Thomas Farges. Surface waves magnitude estimation from ionospheric signature of rayleigh waves measured by doppler sounder and oth radar. *Scientific Reports*, 8(1):1555, 2018.

[34] Javier Peralta, Miguel A López-Valverde, Gabriella Gilli, and Arianna Piccialli. Dayside temperatures in the venus upper atmosphere from venus express/virtis nadir measurements at 4.3 μm. *Astronomy and Astrophysics*, 2016.

[35] Giuseppe Piccioni, Ludmilla Zasova, Alessandra Migliorini, Pierre Drossart, A Shakun, Antonio García Muñoz, Franklin P Mills, and A Cardesin-Moinelo. Near-ir oxygen nightglow observed by virtis in the venus upper atmosphere. *Journal of Geophysical Research: Planets*, 114(E5), 2009.

[36] Jon Rista. Astrophotography Basics: Understanding Signal to Noise Ratio (SNR). `https://jonrista.com/the-astrophotographers-guide/astrophotography-basics/snr/#:~:text=Stacking%20images%20integrates%`

20all%20the,of%20individual%20sub%20frames%20stacked., 2023. Last access on 30.01.2024.

[37] Antoni Rogalski. Infrared detectors: an overview. *Infrared Physics and Technology*, 43(3):187–210, 2002.

[38] Antoni Rogalski. Infrared detectors: status and trends. *Progress in Quantum Electronics*, 27(2):59–210, 2003.

[39] Antonio Rogalski. *Infrared detectors*. CRC press, 2000.

[40] Christian von Savigny. Airglow in the earth atmosphere: basic characteristics and excitation mechanisms. *ChemTexts*, 3(4):14, 2017.

[41] Josh Schoolcraft, Andrew Klesh, and Thomas Werne. *MarCO: Interplanetary Mission Development on a CubeSat Scale*, pages 221–231. Springer International Publishing, Cham, 2017.

[42] A Stern and NS Kopeika. Analytical method to calculate optical transfer functions for image motion and vibrations using moments. *JOSA A*, 14(2):388–396, 1997.

[43] Brian M Sutin, James Cutts, Alan M Didion, Mélanie Drilleau, Matthew Grawe, Jörn Helbert, Ashley Karp, Balthasar Kenda, Attila Komjathy, Siddharth Krishnamoorthy, et al. Vamos: A smallsat mission concept for remote sensing of venusian seismic activity from orbit. In *Space Telescopes and Instrumentation 2018: Optical, Infrared, and Millimeter Wave*, volume 10698, pages 1651–1670. SPIE, 2018.

[44] Teledyne. Binning. https://www.photometrics.com/learn/camera-basics/binning. Last access on: 29.01.2024.

[45] Teledyne. H2RG Visible & Infrared Focal Plane Array. Technical report, Teledyne Imaging Sensors, April 2012. Cleared for Public Release by the DoD's Office of Security Review Case 12-S-1868.

[46] Nicolas Thomas, Gabriele Cremonese, Ruth Ziethe, Michael Gerber, Mathias Brändli, Giordano Bruno, Marc Erismann, Lisa Gambicorti, Thomas Gerber, Kaustav Ghose, et al. The colour and stereo surface imaging system (cassis) for the exomars trace gas orbiter. *Space science reviews*, 212:1897–1944, 2017.

[47] Thorlabs. Infrared bandpass filters, 2024. Last access on: 14.02.2024.

[48] Thorlabs. Optical bandpass filters, 2024. Last access on: 14.02.2024.

[49] J.R. Wertz and W.J. Larson. *Space Mission Analysis and Design*. Space technology library. Kluwer Academic, 1991.

[50] Dave Williams. Venus Fact Sheet, 2024. Last access on 28.01.2024.

[51] William L Wolfe. *Introduction to infrared system design*, volume 24. SPIE Press, 1996.

[52] Majid Zandian, Mark Farris, William McLevige, Dennis Edwall, Erdem Arkun, Eric Holland, James E Gunn, Stephen Smee, Donald NB Hall, Klaus W Hodapp, et al. Performance of science grade hgcdte h4rg-15 image sensors. In *High Energy, Optical, and Infrared Detectors for Astronomy VII*, volume 9915, pages 148–158. SPIE, 2016.

[53] H. Zhou. Signal-to-noise (snr) and uncertainty estimates. `https://nmr.chem.ucsb.edu/protocols/SNR.html#:~:text=A%20SNR%20of%203%20(3ÏČ,or%20ratios%20between%20different%20peaks`, 2019. Last access on: 30.01.2024.

A Additional Plots: Trade-off Analysis

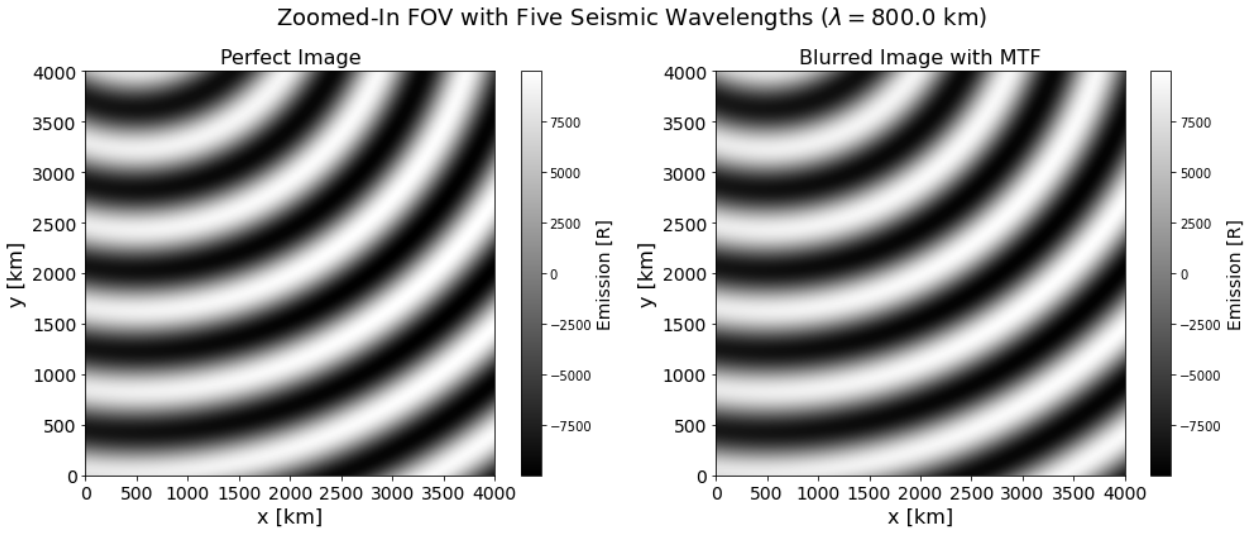

Figure A.1: Contrast comparison for perfect (MTF = 1) and blurred image (applied MTF) with the expected emission in Rayleigh for a FOV cut-out (5 × 800 × 800 km) **without** a background noise signal for a surface magnitude of $M_S = 7.5$ (best case) using the Xenics XSW640 LG

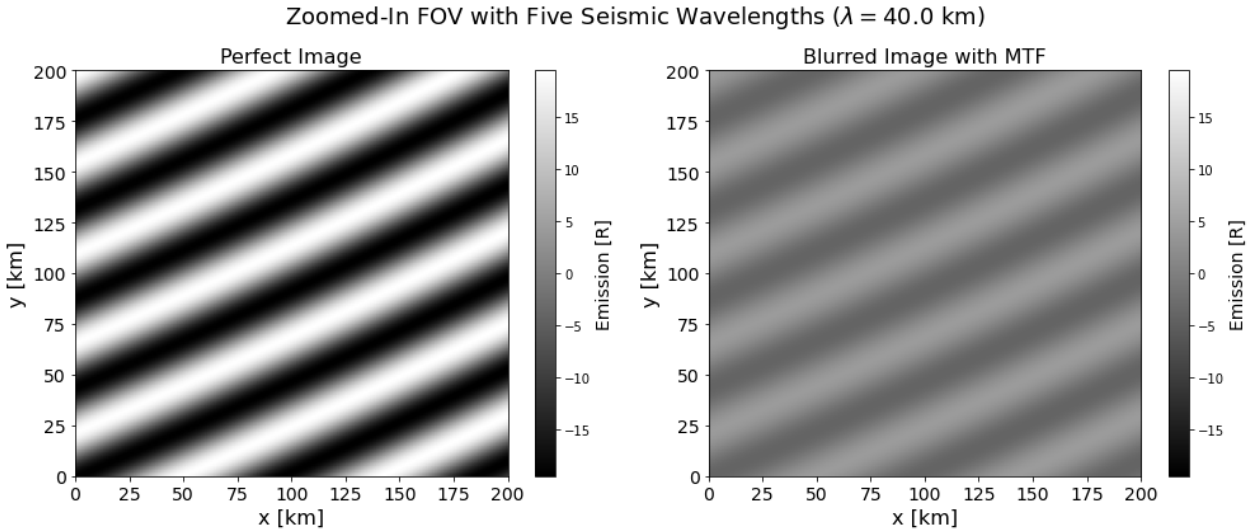

Figure A.2: Contrast comparison for perfect (MTF = 1) and blurred image (applied MTF) with the expected emission in Rayleigh for a FOV cut-out (5 × 40 × 40 km) **without** a background noise signal for a surface magnitude of $M_S = 5.5$ (worst case) using the Xenics XSW640 LG

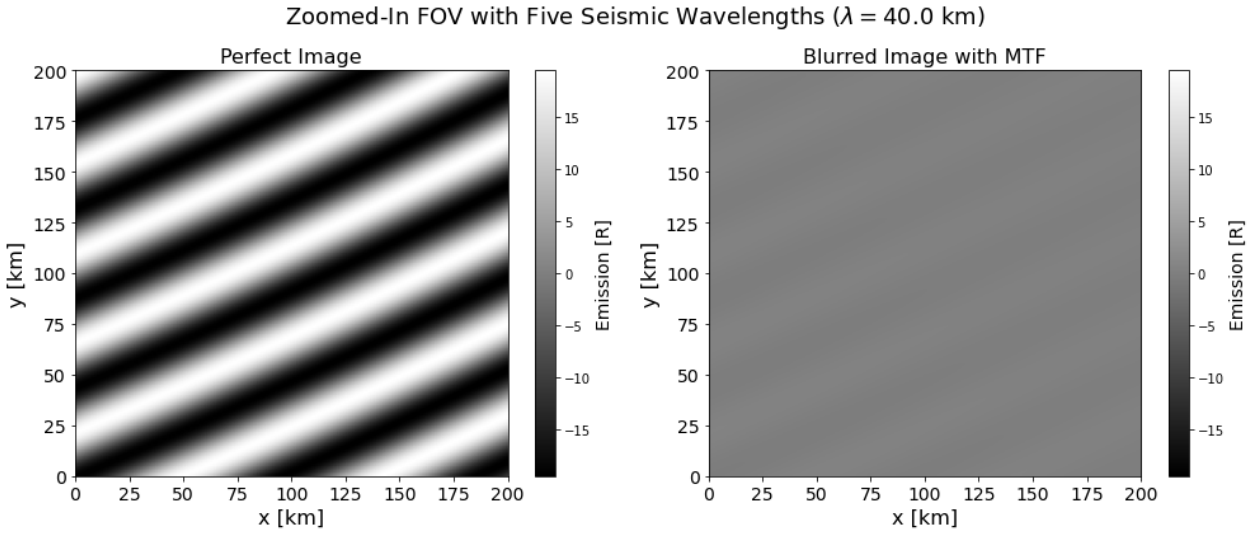

Figure A.3: Contrast comparison for perfect (MTF = 1) and blurred image (applied MTF) with the expected emission in Rayleigh for a FOV cut-out (5 × 40 × 40 km) **without** a background noise signal for a surface magnitude of $M_S = 5.5$ (worst case) using the SCD Cardinal 1280 LG

B 1D MTF Curves of Preliminary Design Options

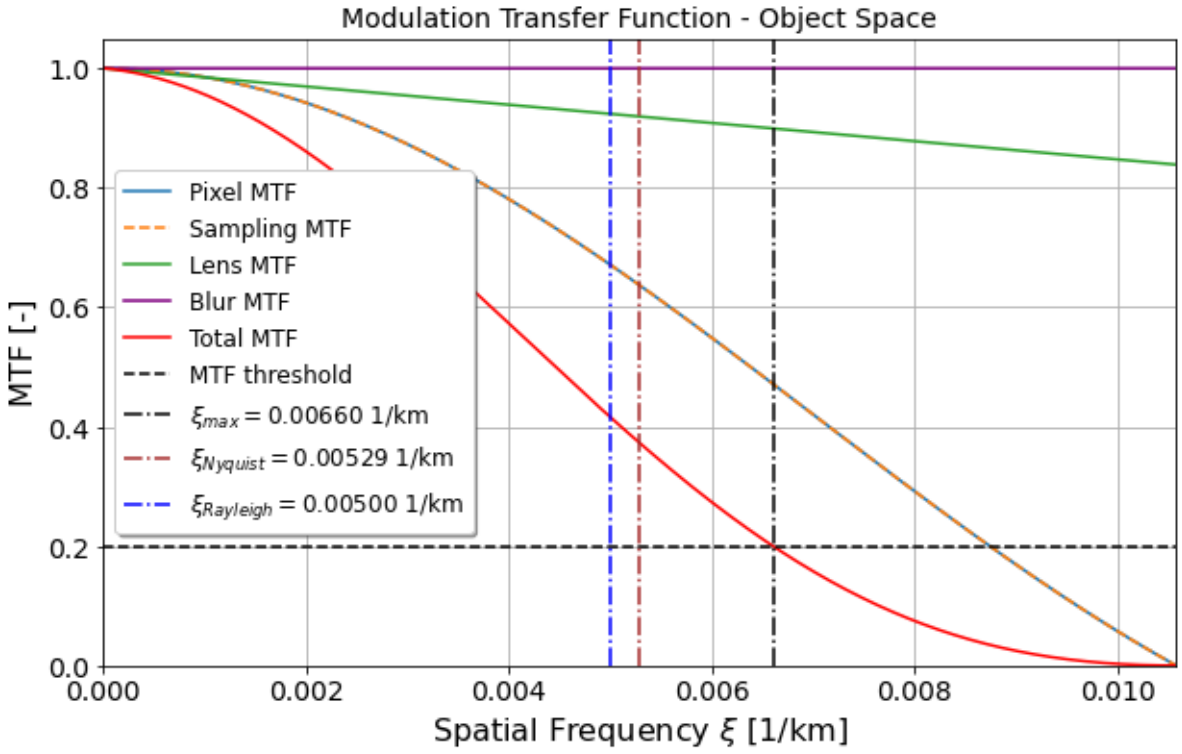

Figure B.1: MTF as a function of the spatial frequency in object space for the imaging system with the SCD Cardinal 1280 MG detector (Full disk FOV) for the nominal case

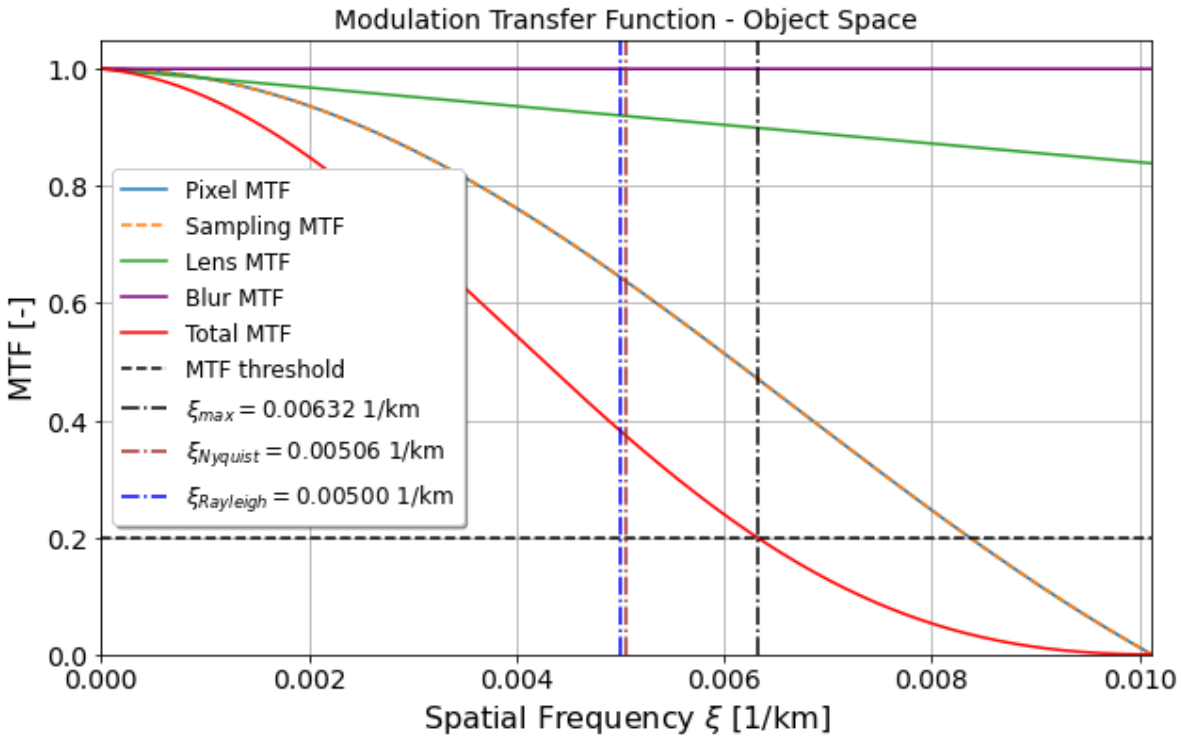

Figure B.2: MTF as a function of the spatial frequency in object space for the imaging system with the SCD Cardinal 1280 MG detector (Zoomed FOV) for the nominal case

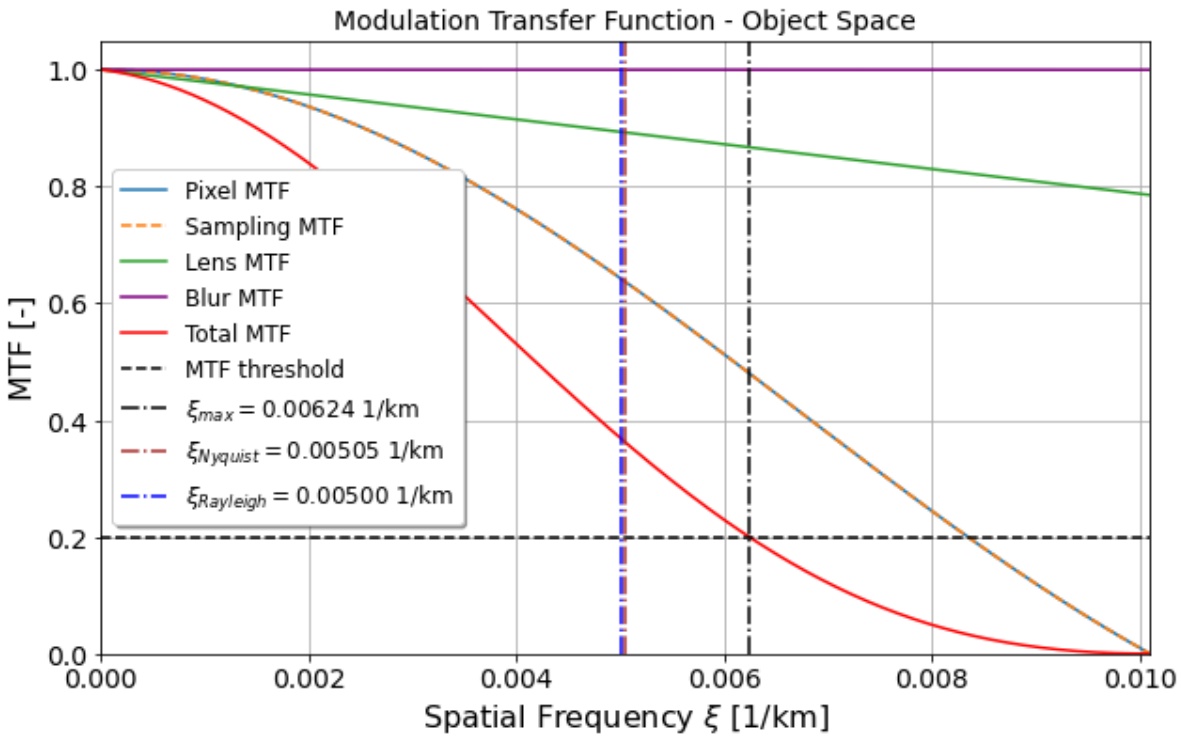

Figure B.3: MTF as a function of the spatial frequency in object space for the imaging system with the Teledyne H4RG SWIR detector (Zoomed FOV) for the nominal case

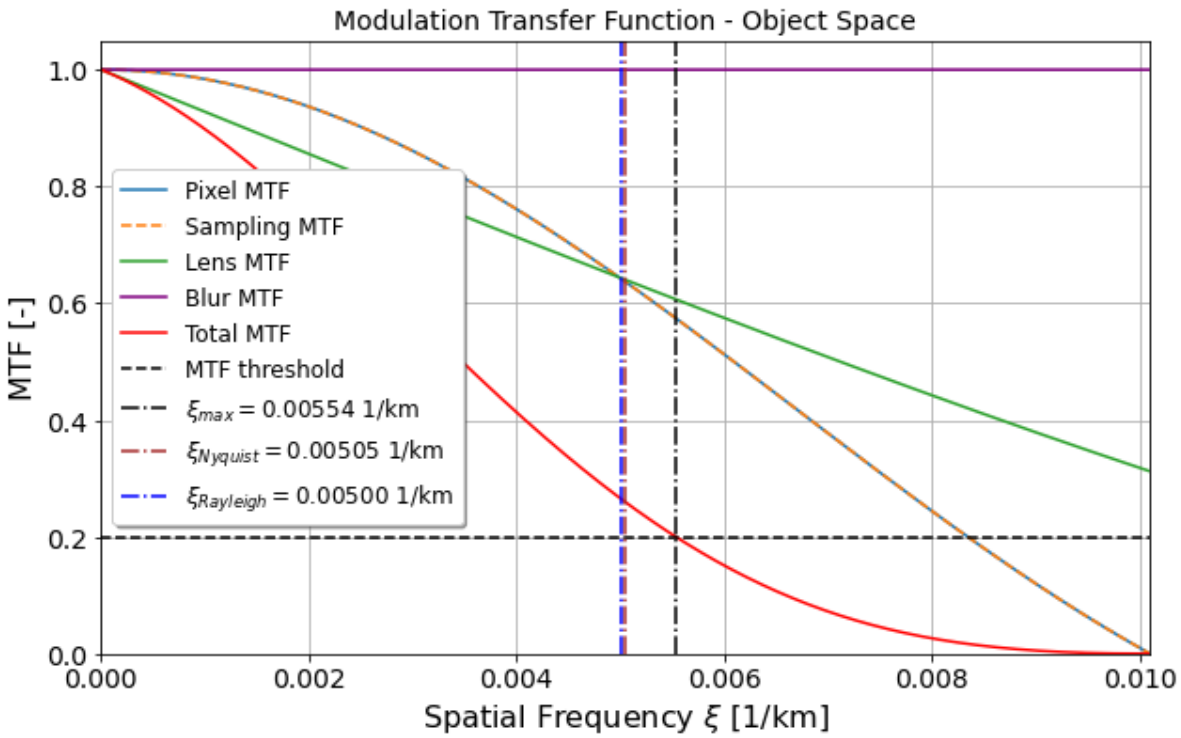

Figure B.4: MTF as a function of the spatial frequency in object space for the imaging system with the Teledyne H4RG MWIR detector (Zoomed FOV) for the nominal case

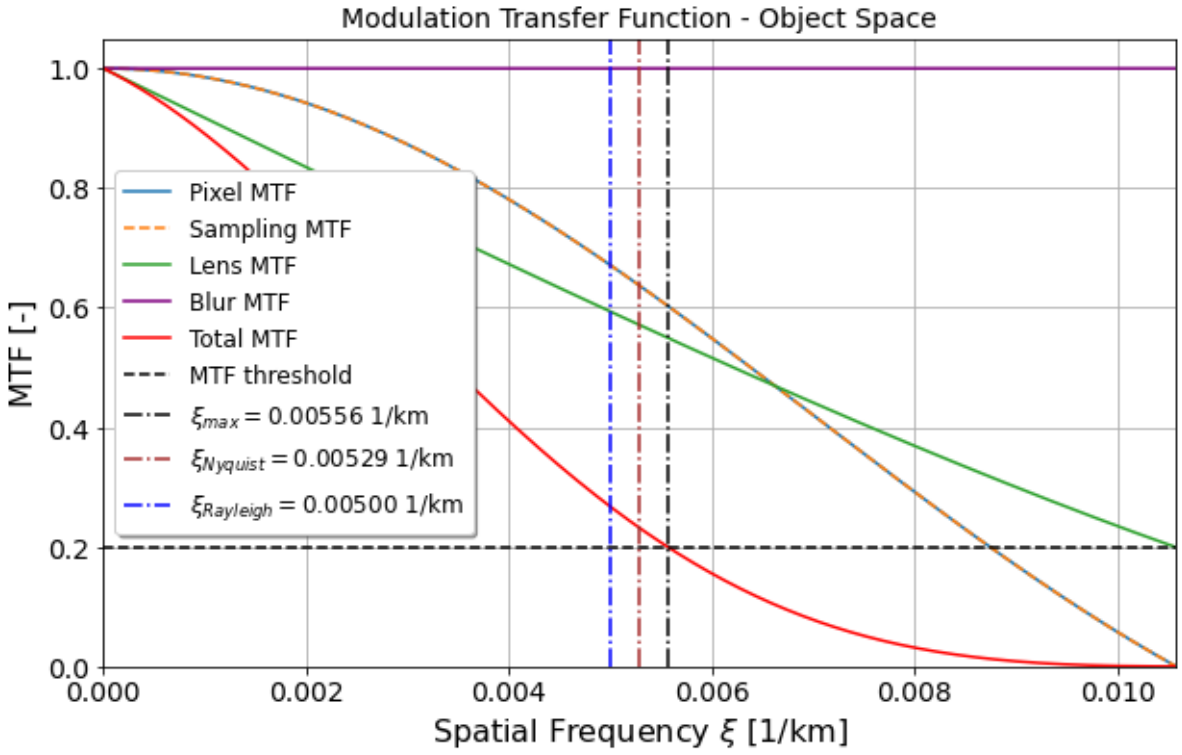

Figure B.5: MTF as a function of the spatial frequency in object space for the imaging system with the Raytheon Phoenix detector (Full disk FOV) for the nominal case

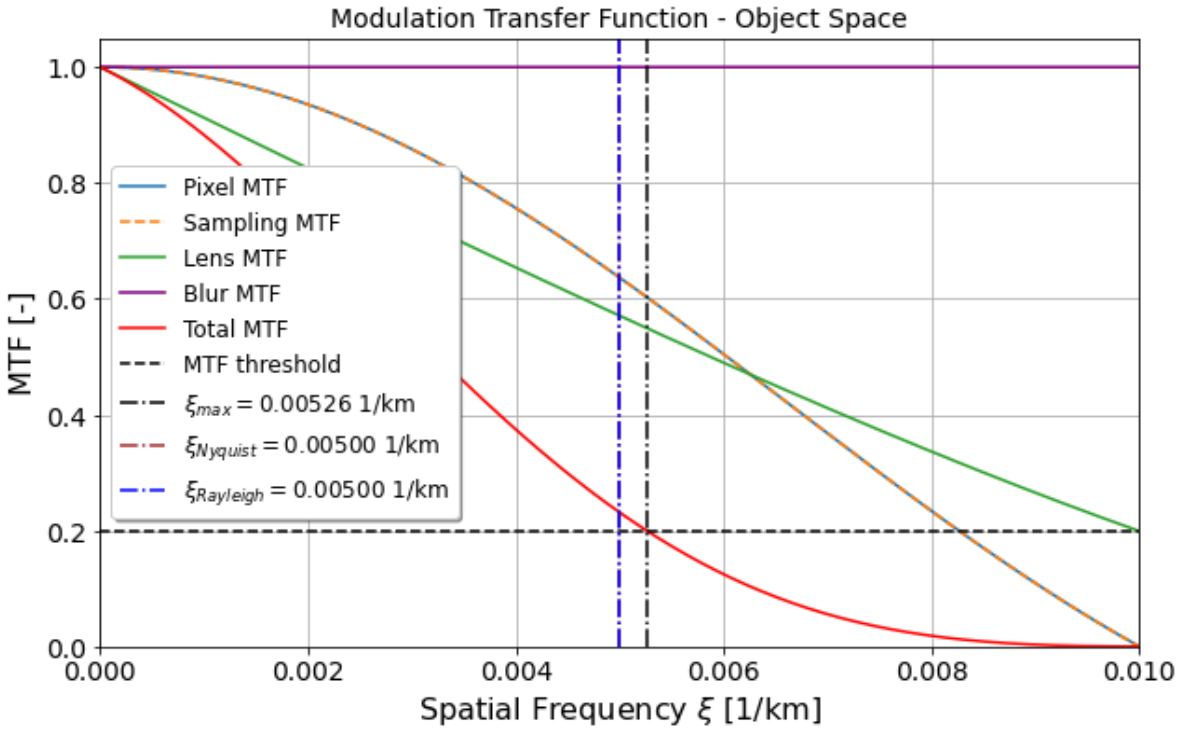

Figure B.6: MTF as a function of the spatial frequency in object space for the imaging system with the Raytheon Phoenix detector (Zoomed FOV) for the nominal case

C Simulated Images

C.1 Nightside observation

- SCD Cardinal 1280 MG Full Disk FOV (Nominal)
- SCD Cardinal 1280 MG Full Disk FOV (Best)
- Teledyne H4RG SWIR Full Disk FOV (Best)

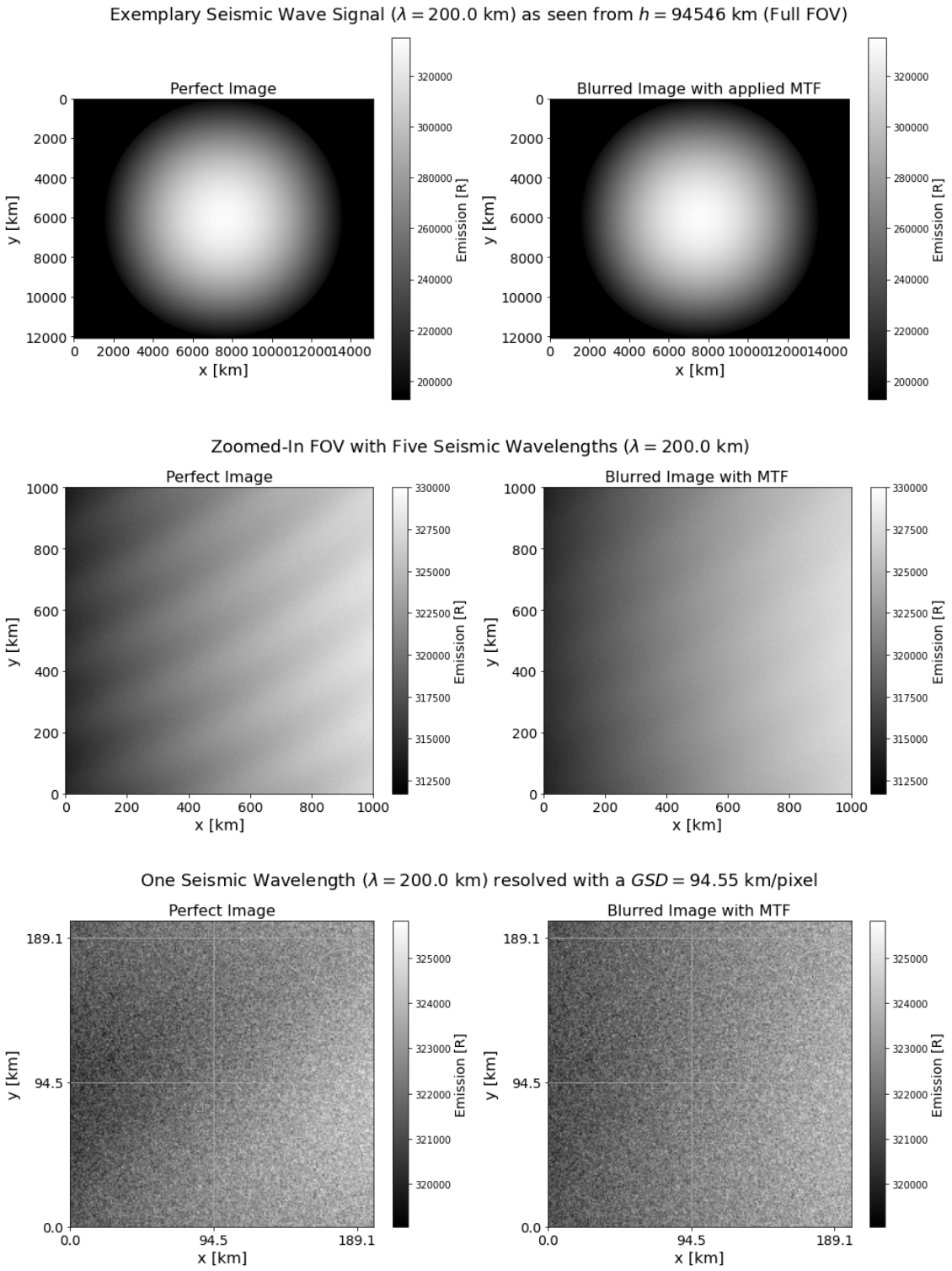

Figure C.1: Contrast comparison for perfect (MTF = 1) and blurred image (applied MTF) with the expected emission in Rayleigh with Venus' full disk in the FOV (top), for a 5 × 200 × 200 km FOV cut-out (center) and for a 200 × 200 km FOV cut-out (bottom) for a background signal with $L_{\lambda_{peak}} = 0.07$ Wm^{-2}µm^{-1}sr^{-1} at 1.27 µm and a surface magnitude of $M_S = 6.5$ (nominal case) resulting in SNR = 1.58 using the SCD Cardinal 1280 MG

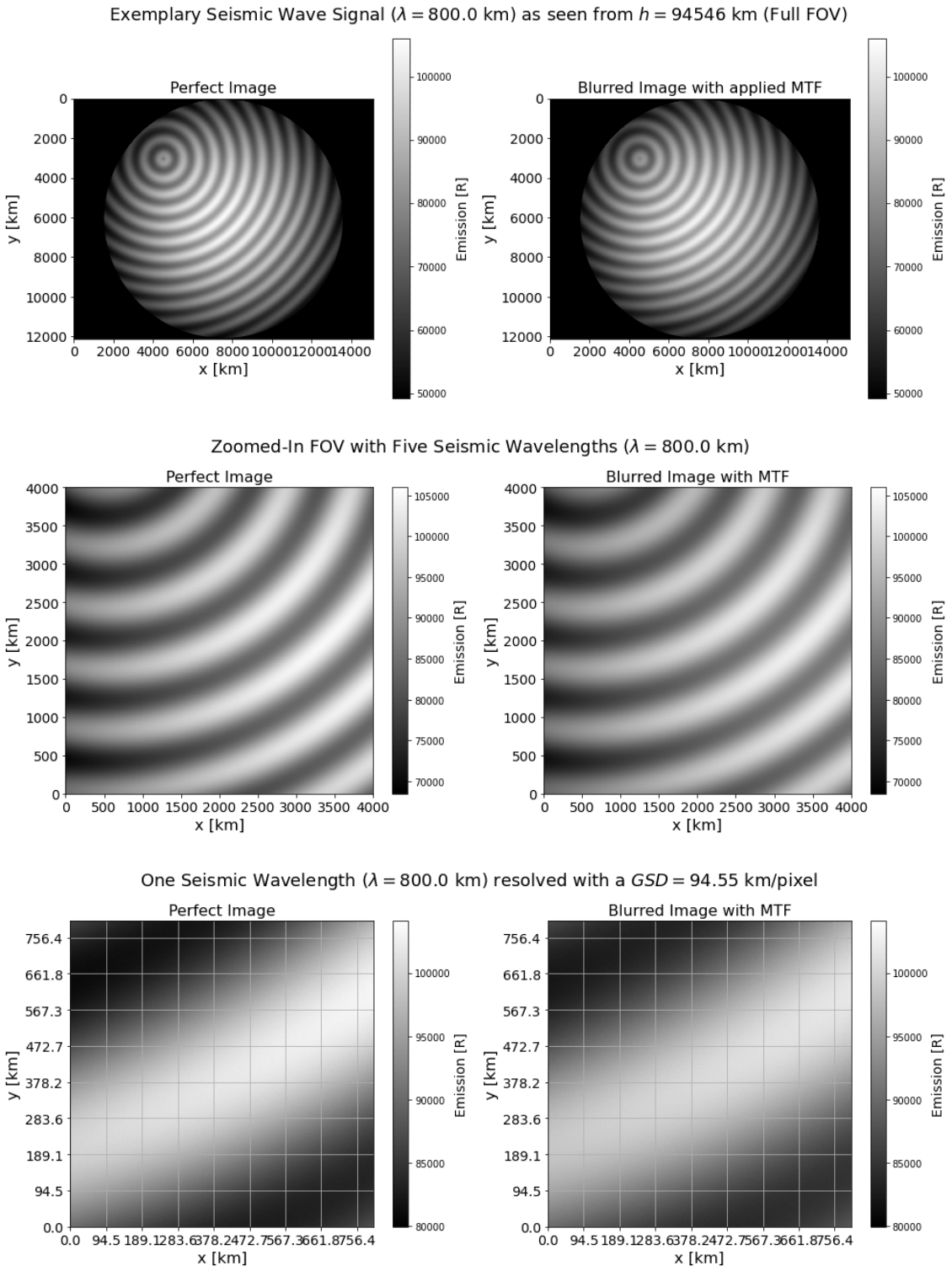

Figure C.2: Contrast comparison for perfect (MTF = 1) and blurred image (applied MTF) with the expected emission in Rayleigh with Venus' full disk in the FOV (top), for a 5 × 800 × 800 km FOV cut-out (center) and for a 800 × 800 km FOV cut-out (bottom) for a background signal with $L_{\lambda_{peak}} = 0.02$ Wm^{-2}µm^{-1}sr^{-1} at 1.27 µm and a surface magnitude of $M_S = 7.5$ (best case) resulting in SNR = 39 using the SCD Cardinal 1280 MG

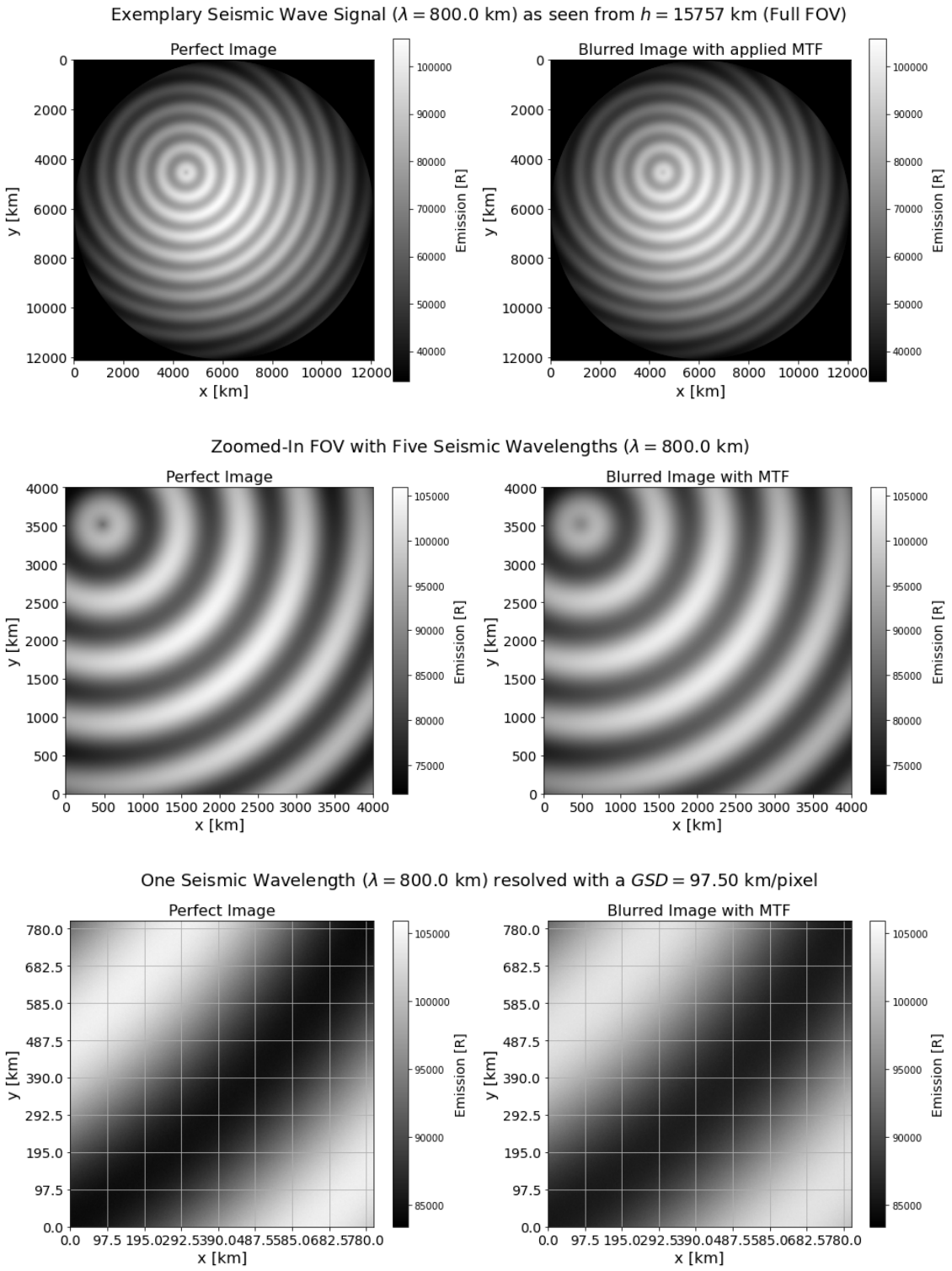

Figure C.3: Contrast comparison for perfect (MTF = 1) and blurred image (applied MTF) with the expected emission in Rayleigh with Venus' full disk in the FOV (top), for a 5 × 800 × 800 km FOV cut-out (center) and for a 800 × 800 km FOV cut-out (bottom) for a background signal with $L_{\lambda_{peak}} = 0.02$ Wm^{-2}µm^{-1}sr^{-1} at 1.27 µm and a surface magnitude of $M_S = 7.5$ (best case) resulting in SNR = 43 using the Teledyne H4RG SWIR

C.2 Dayside observation

- Teledyne H4RG MWIR Full Disk FOV (Best)
- Raytheon Phoenix Full Disk FOV (Nominal)
- Raytheon Phoenix Full Disk FOV (Best)

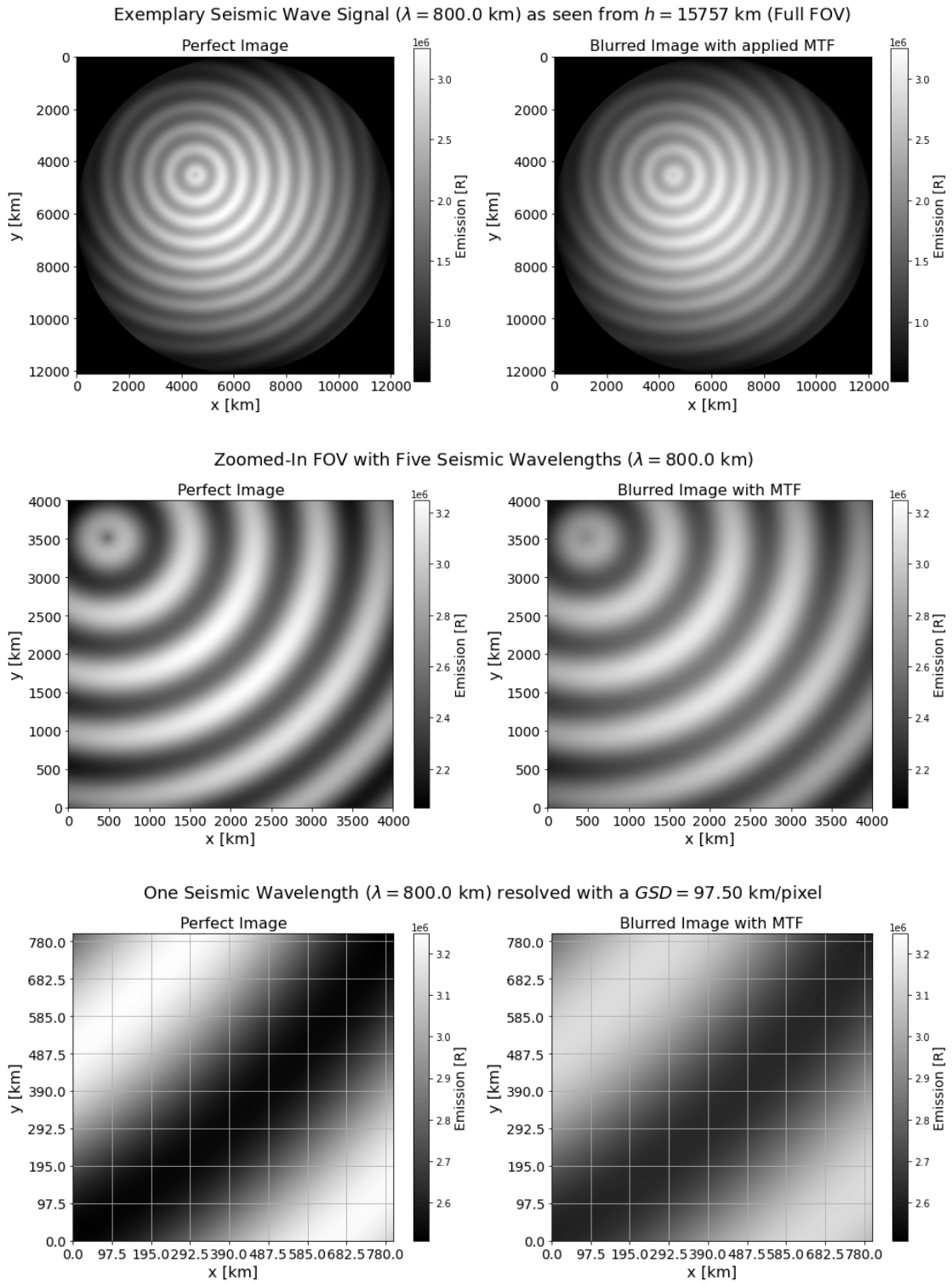

Figure C.4: Contrast comparison for perfect (MTF = 1) and blurred image (applied MTF) with the expected emission in Rayleigh with Venus' full disk in the FOV (top), for a 5 × 800 × 800 km FOV cut-out (center) and for a 800 × 800 km FOV cut-out (bottom) for a background signal with $L_{\lambda_{peak}} = 0.02$ Wm^{-2}µm^{-1}sr^{-1} at 1.27 µm and a surface magnitude of $M_S = 7.5$ (best case) resulting in SNR = 22 using the Teledyne H4RG MWIR

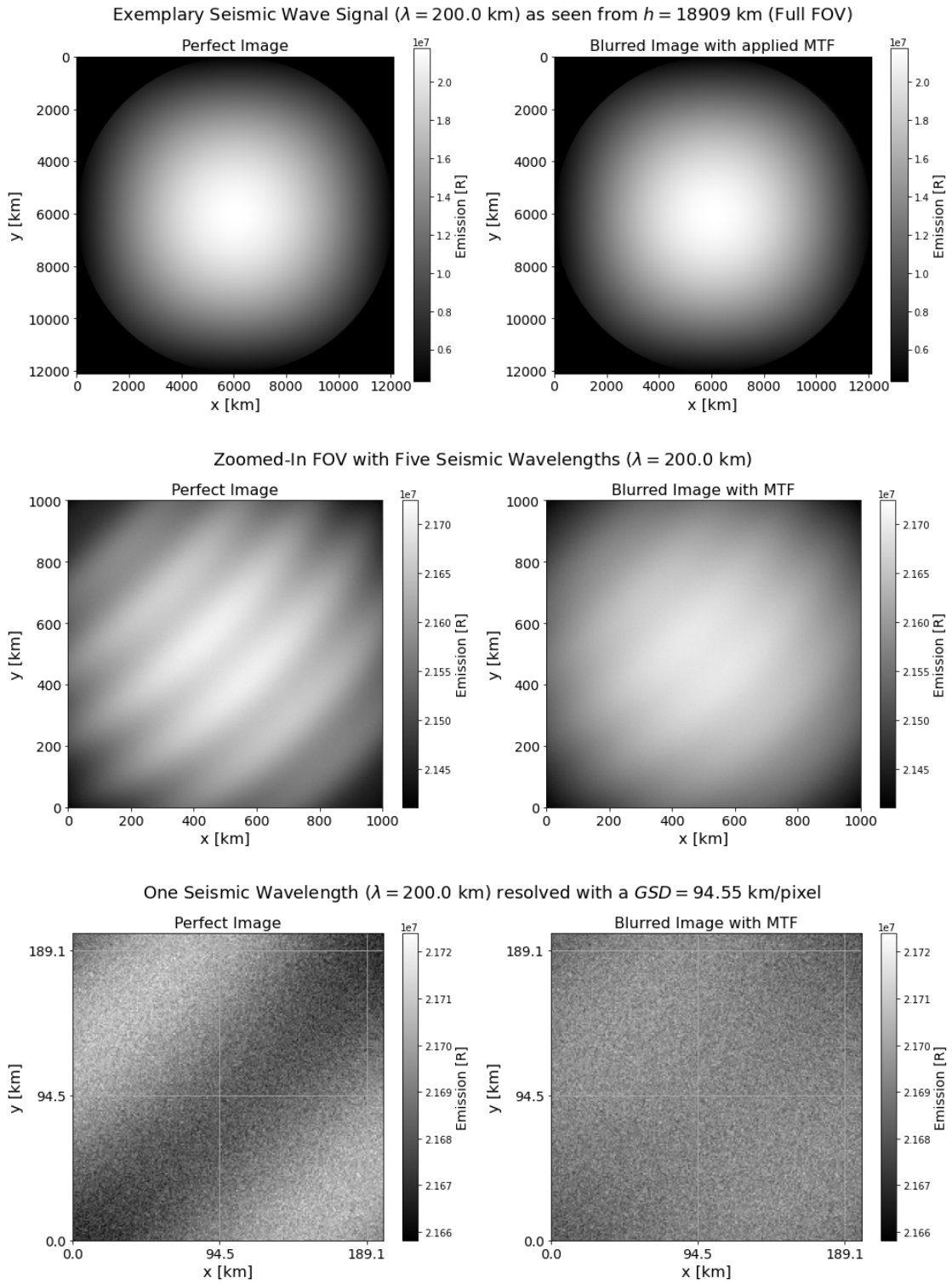

Figure C.5: Contrast comparison for perfect (MTF = 1) and blurred image (applied MTF) with the expected emission in Rayleigh with Venus' full disk in the FOV (top), for a 5 × 200 × 200 km FOV cut-out (center) and for a 200 × 200 km FOV cut-out (bottom) for a background signal with $L_{\lambda_{peak}} = 0.07$ Wm^{-2}µm^{-1}sr^{-1} at 1.27 µm and a surface magnitude of $M_S = 6.5$ (nominal case) resulting in SNR = 1.58 using the Raytheon Phoenix

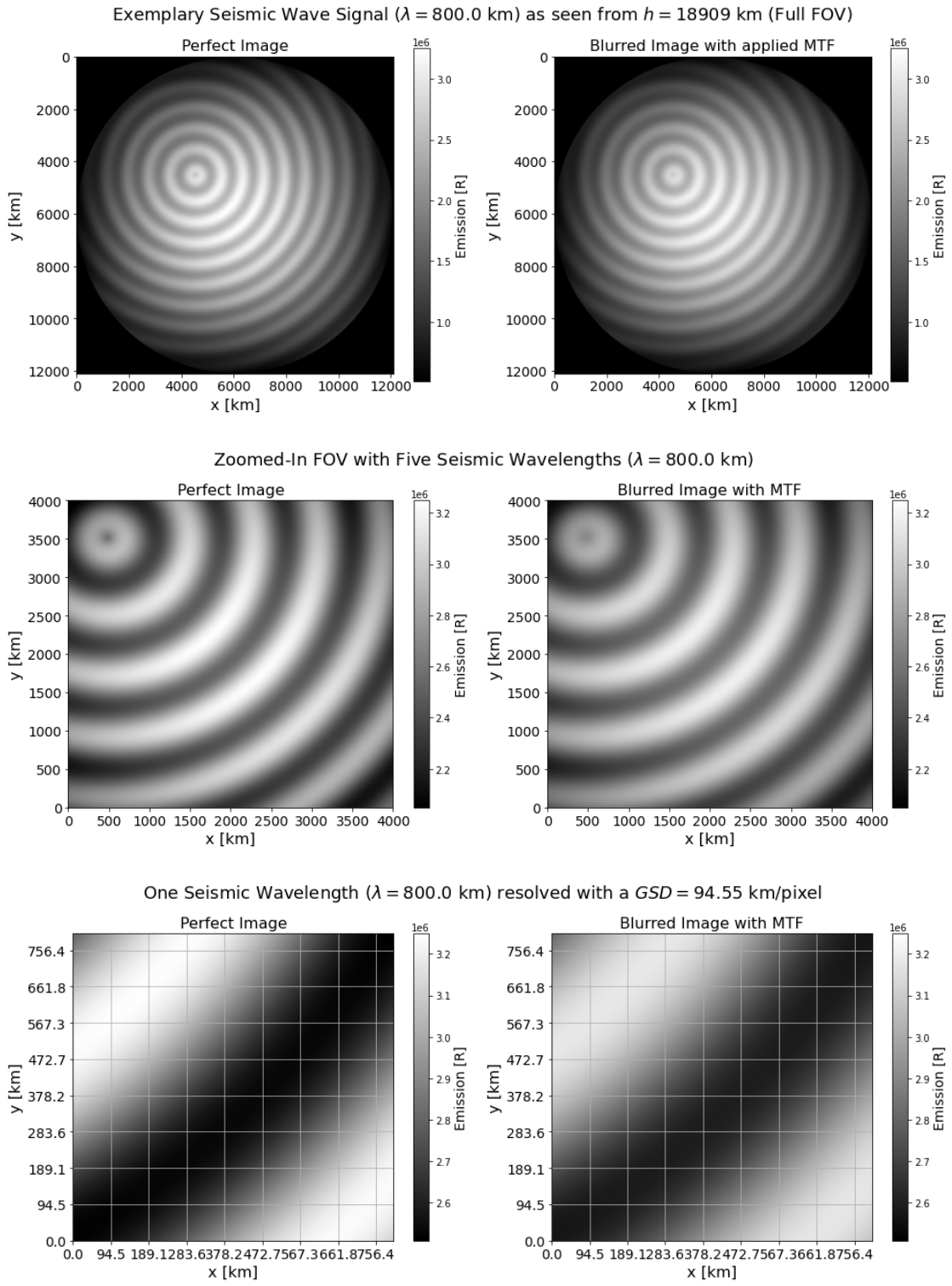

Figure C.6: Contrast comparison for perfect (MTF = 1) and blurred image (applied MTF) with the expected emission in Rayleigh with Venus' full disk in the FOV (top), for a 5 × 800 × 800 km FOV cut-out (center) and for a 800 × 800 km FOV cut-out (bottom) for a background signal with $L_{\lambda_{peak}} = 0.02$ Wm^{-2}µm^{-1}sr^{-1} at 1.27 µm and a surface magnitude of $M_S = 7.5$ (best case) resulting in SNR = 38 using the Raytheon Phoenix